universität wien

MASTERARBEIT / MASTER'S THESIS

Titel der Masterarbeit / Title of the Master's Thesis

AMS measurements of ^{36}Cl using isobar suppression via laser photodetachment

verfasst von / submitted by

Christoph Marek, BSc.

angestrebter akademischer Grad / in partial fulfilment of the requirements for the degree of

Master of Science (MSc.)

Wien, 2018 / Vienna, 2018

Studienkennzahl lt. Studienblatt / degree programme code as it appears on the student record sheet:	A 066 876
Studienrichtung lt. Studienblatt / degree programme as it appears on the student record sheet:	Masterstudium Physik
Betreut von / Supervisor:	Univ.-Prof. Dipl.-Ing. Dr. Robin Golser
Mitbetreut von / Co-Supervisor:	Dipl.-Phys. Dr. Johannes Lachner

Abstract

Natural phenomena and archaeological findings are commonly dated with the use of long-lived radionuclides (e.g. ^{14}C, ^{36}Cl). The long half-life of these isotopes makes a radiometric approach inefficient and therefore accelerator mass spectrometry (AMS) is used to determine low concentrations. Depending on the isotope of interest, the isotope ratio can be measured down to 10^{-16} in AMS, e.g. for ^{36}Cl/Cl. The limiting factor is the interference of isobars, which cannot be separated by the electrostatic and magnetic filters of the mass spectrometer. While a stripping process can be used to dissociate isobaric molecules, the suppression of an atomic isobar is more challenging. The new Ion Laser InterAction Mass Spectrometer (ILIAMS) is designed for the application of a selective photodetachment suppression for AMS measurements. The ILIAMS setup extends the already established Vienna Environmental Research Accelerator (VERA), the AMS facility at the University of Vienna. In the ILIAMS system a laser is used to neutralize unwanted interferences with lower electron affinity (EA) than the measured atomic or molecular form of the isotope of interest.

The aim of this master's thesis was to use this new suppression technique for ^{36}Cl measurements, where the stable isobar ^{36}S has a lower electron affinity. During the investigation the suppression of sulfur by the interaction with a green laser ($\lambda = 532\,\mathrm{nm}$) could be demonstrated. A suppression factor in the order of 10^{10} was reached, increasing the detector efficiency to nearly 100 %. Measurements with two sets of unknown samples were successfully carried out. By the selection of the 2+ high energy charge state the overall measurement efficiency could be further improved. Molecular background investigations revealed that the application of higher photon energy could possibly suppress all interferences, making measurements at low beam energy (e.g. 30 keV) feasible.

Zusammenfassung

Natürliche Phänomene und archäologische Funde werden häufig mithilfe von langlebigen Radionukliden (z.B. ^{14}C, ^{36}Cl) datiert. Aufgrund der langen Halbwertszeit dieser Isotope ist eine radiometrische Messung ineffizient und deshalb wird häufig Beschleuniger-Massenspektrometrie (AMS) verwendet um niedrige Konzentrationen zu messen. Abhängig vom Isotop können damit Verhältnisse (z.B. ^{36}Cl/Cl) bis zu 10^{-16} gemessen werden. Limitiert wird dies durch Isobare, welche nicht mithilfe der elektrostatischen und magnetischen Filter des Massenspektrometers unterschieden werden können. Während ein Stripping-Prozess verwendet werden kann um isobarische Moleküle zu dissoziieren, ist die Unterdrückung von atomaren Isobaren schwieriger. Das neue "Ion Laser InterAction Mass Spectrometer" (ILIAMS) wurde entwickelt um Isobare mithilfe von selektivem Photodetachment zu unterdrücken und erweitert die etablierte AMS-Anlage "Vienna Environmental Research Accelerator" (VERA) der Universität Wien. Die Photonen eines Lasers werden hierbei verwendet, um Interferenzen mit geringerer Elektronen Affinität als die atomare oder molekulare Form des gewünschten Isotops zu neutralisieren.

Das Ziel dieser Masterarbeit war die Anwendung dieser neuen Technik für ^{36}Cl Messungen, bei denen die stabile Interferenz ^{36}S eine niedrigere Elektronen Affinität aufweist. Durch Wechselwirkung zwischen Schwefelanionen und einem grünen Laser ($\lambda = 532\,\text{nm}$) konnte eine Unterdrückung in der Größenordnung 10^{10} demonstriert werden, was die Detektoreffizient auf beinahe 100 % erhöht. Zwei größere ^{36}Cl Messungen wurden erfolgreich durchgeführt und die Auswahl des Ladungszustandes 2+ konnte die Gesamteffizienz der Messung weiter verbessern. Die Untersuchung des bisher bekannten molekularen Hintergrundes zeigte, dass ein Laser mit höherer Photonenenergie alle Interferenzen unterdrücken könnte, was Messungen auf der Niederenergieseite ermöglichen würde.

Contents

1. Motivation

The determination of ^{36}Cl concentration in environmental samples is, similar to the more commonly known radiocarbon method, used for dating certain events in nature. The isotope ^{36}Cl is mainly produced in rocks and is used in surface exposure dating. Today very low ratios in the region of 10^{-12} to 10^{-16}, between rare and stable isotope, are usually measured with Accelerator Mass Specrometry (AMS) [Hellborg and Skog, 2008].

In AMS typically a solid-state target material, like graphite in the case of carbon and AgCl for chlorine measurements, is sputtered to produce negative ions. Impurities in the target material may interfere and have to be separated in the AMS system for precise concentration measurements. In the radiocarbon method the stable isobar ^{14}N does not form negative ions due to its negative electron affinity and therefore does not interfere with ^{14}C measurements. In contrast to nitrogen, the stable isotope ^{36}S can form negative ions, making ^{36}Cl measurements more challenging.

First successful dating of wood samples of known age using ^{14}C was done by Arnold and Libby [1949] using a radiometric approach. During a radiometric measurement the isotope decays were counted and due to the long half-life (^{14}C of (5700 ± 30) years [NNDC, 2018]) they required a sample size of 8 gram to measure the concentration within a reasonable time. According to Hammer et al. [2017] current sample sizes for low-level counting require around $20\,\mathrm{m}^3$ of atmospheric air, which corresponds to around 4 gram of Carbon. The half life time of ^{36}Cl is (301 ± 2) kyrs [NNDC, 2018], which would require an even larger sample size or a longer measurement time, hence making the radiometric approach very inefficient.

The already mentioned new approach is counting the radionuclide atom by atom using mass spectrometry. Since this method does not involve the decay of the interested isotope, the efficiency is independent of the half-life and can even be used for stable isotopes. The additional utilization of an accelerator increases the discrimination of isobaric interference and is called Accelerator Mass Specrometry (AMS).

A typical AMS system consists of a negative ion source, a tandem accelerator and a combination of electrostatic and magnetic filters. The suppression of molecules, having the same mass as the isotope of interest, can be done by using a stripping process. During this process electrons are stripped from an initially produced anion [Purser, 1977]. In the case of small molecules consisting of light elements a charge state of 3+ is sufficient to dissociate the molecule [Synal, 2013] into fragments. The application of filters after the stripping process can remove this unwanted interference in most cases.

The separation of atomic isobars is in general more challenging, because they can not be dissociated. In some cases the use of a negative ion source already eliminates the interference, because a negative electron affinity does not allow the formation of a stable negative ion (e.g. ^{14}N). If this is not the case other methods commonly use energy loss inside a detector [Fifield et al., 1987], or in a gas filled magnet [Zoppi et al., 1994], both requiring an high energy ion beam. Other suppression methods for specific isotope measurement, e.g. the use of a degrader foil for the ^{10}Be/^{10}B separation[Raisbeck et al., 1984; Nottoli et al., 2013], have been proven to be effective.

New AMS systems tend to lower acceleration voltage. Due to the lower ion energy the suppression of the isobaric background in the common way usually gets worse. In the case of ^{10}Be a degrader foil makes small systems competitive with larger facilities [Müller et al., 2010], but the small relative difference in nuclear charge number between chlorine and sulfur still limits the capability of measuring ^{36}Cl.

Currently two new methods for isobaric suppression are investigated, which would allow separation even in the low energy region.

One of them was initially investigated at the IsoTrace laboratory in Toronto. It makes use of chemical reactions between ions in the eV range and a gas inside a reaction cell [Litherland et al., 2007]. Further investigations on the reaction cell technique are continued at the André E. Lalonde AMS laboratory in Ottawa [Kieser et al., 2015] [Eliades et al., 2015].

The other suppression method uses electromagnetic radiation for selective neutralization of the unwanted interference. It makes use of the photodetachment process to neutralize interfering isobars with lower electron affinity than the isotope of interest. Since a laser sends out a photon beam of high intensity and small bandwidth, it is the best suited source of electromagnetic radiation. This method is therefore commonly known as laser photodetachment. Currently the Isotope Research and Nuclear Physics group at the University of Vienna is investigating the potential of this new technique for AMS in combination with the already existing AMS system VERA (Vienna Environmental Research Accelerator).

The investigation of laser photodetachment suppression of ^{36}S and its application for ^{36}Cl AMS measurements is part of the investigation at VERA and is the objective of this master's thesis.

2. Introduction

2.1. The isotope ^{36}Cl

The element chlorine has the atomic number 17. The mole fraction abundance of its stable isotopes ^{35}Cl and ^{37}Cl are (75.76±0.1) % and (24.24±0.1) %, respectively [NNDC, 2018]. Between the two stable isotopes lies the radionuclide ^{36}Cl with a half-life of (301±2) kyrs [NNDC, 2018]. The long life time already indicates the advantageous use of mass spectrometry for concentration measurements.

The rest of the Chlorine isotopes listed in the nuclear chart are also unstable and have half-lives ranging from less than 20 nanoseconds to about 56 minutes [NNDC, 2018]. Therefore, their concentrations, if needed, could be measured using the radiometric approach, but these isotopes are not relevant for dating.

Reservoir	**Chlorine content**	**Form**
Earth mantle	$22{\cdot}10^{21}$ kg	Mineral
Earth crust	$60{\cdot}10^{18}$ kg	Mineral
Oceans	$26{\cdot}10^{18}$ kg	Ionic

Table 2.1.: Natural chlorine content in Earth's three largest chlorine reservoirs. Other reservoirs like freshwater, troposphere and stratosphere have an abundance below ppm. The values in this table are taken from Graedel and Keene [1996].

According to the approximations by Graedel and Keene [1996] the natural Chlorine content on Earth is about $22.1{\cdot}10^{24}$ gram. This chlorine resides in different Earth reservoirs and the content of the three largest reservoirs is listed in Table 2.1. Most of Earth's natural chlorine is incorporated in minerals. Almost everything else is dissolved in water and therefore in ionic form inside the oceans.

Natural chlorine in gaseous form can be found in the troposphere and stratosphere, but the relative abundance is approximately $2{\cdot}10^{-13}$ (calculated using data from [Graedel and Keene, 1996]). In the work of Graedel and Keene [1996] the flux of Chlorine between the reservoirs is also discussed, which will not be reviewed here.

Chlorine is an important substance in the chemical industry, where according to Kleijn and Van der Voet [1998] about 34 % is used for the production of polyvinyl chloride. The study by Kleijn and Van der Voet [1998] also shows that in Western Europe about 7 % of the chlorine inflow of the chemical industry (around $7 \cdot 10^{11}$ gram in the year 1992) was emitted into the environment. It is stated, that about 99 % is emitted into the air, which increases the abundance of chlorine in the corresponding reservoirs. When talking about the relative abundance of the element chlorine in Earth's reservoirs the antropogenic influence is still very small and can be neglected. The annual reports of Euro Chlor (e.g. [EuroChlor, 2009]) even show a decrease of chlorinated organic compound emission, making the antropogenic influence even less important in the last years.

2.1.1. Production of ^{36}Cl

The energy independent production rate P_N of a specific nuclide N per time unit and per volume can be given by

$$P_N = \sum_{x,y} \Phi_x \cdot \sigma_{x,y,N} \cdot \rho_y \tag{2.1}$$

where Φ_x is the flux of particle x through a volume with particle density ρ_y of the particle species y. The cross section $\sigma_{x,y,N}$ for a reaction between particles x and y resulting in the formation of N depends on the center-of-mass energy of the system. Since the particle flux is in general not monoenergetic the calculation for the actual production requires an additional integration of the particle spectrum and the cross section over the energy.

The reactions typically producing ^{36}Cl can be split into the three different categories: spallation reactions, muon reactions and neutron absorption.

Since they can either have natural or anthropogenic origin the two types will be discussed separately.

Natural production

In nature, reactions from all three categories take place. An important factor in the natural production is the cosmic radiation. A small overview of the possible reactions happening in the atmosphere due to cosmic radiation is given in Figure 2.1.

The flux and the energy spectrum of the cosmic radiation depends on multiple factors, e.g. the geographic latitude of the production site. These dependencies will not be discussed here, but for a better understanding of cosmogenic nuclides the work of Gosse and Phillips [2001] gives a detailed model.

When a high energy particle from the cosmic radiation collides with a nucleus a spallation reaction can happen. During the spallation a number of nucleons can be knocked out of the original nucleus, forming a different and lighter nucleus. In the case of ^{36}Cl production the most important spallation targets are K, Ca and Ar [Phillips, 2000]. Since argon is the third most abundant element in the atmosphere its contribution to the ^{36}Cl production is estimated to be in the range of 12 to 20 ^{36}Cl atoms per m^2 and per second [Huggle et al., 1996; Lal and Peters, 1967]. Spallation experiments by Stan-Sion et al. [1996] for ^{40}Ar(p,αn)^{36}Cl and ^{40}Ar(p,2p3n)^{36}Cl reactions revealed cross sections in the range of 22-64 mbarn. In the experiments an argon gas target was irradiated with 17-1000 MeV protons.

As a by-product of spallation mesons (e.g. π^-) can be formed, which typically decay into muons (Figure 2.1). The negative muon can either show weak decay

$$\mu^- \rightarrow e^- + \bar{\nu}_e + \nu_\mu \tag{2.2}$$

or can be captured by a proton of a nucleus. During the capture process the muon interacts via the weak force with the proton, resulting in a bound neutron and an emitted muon neutrino.

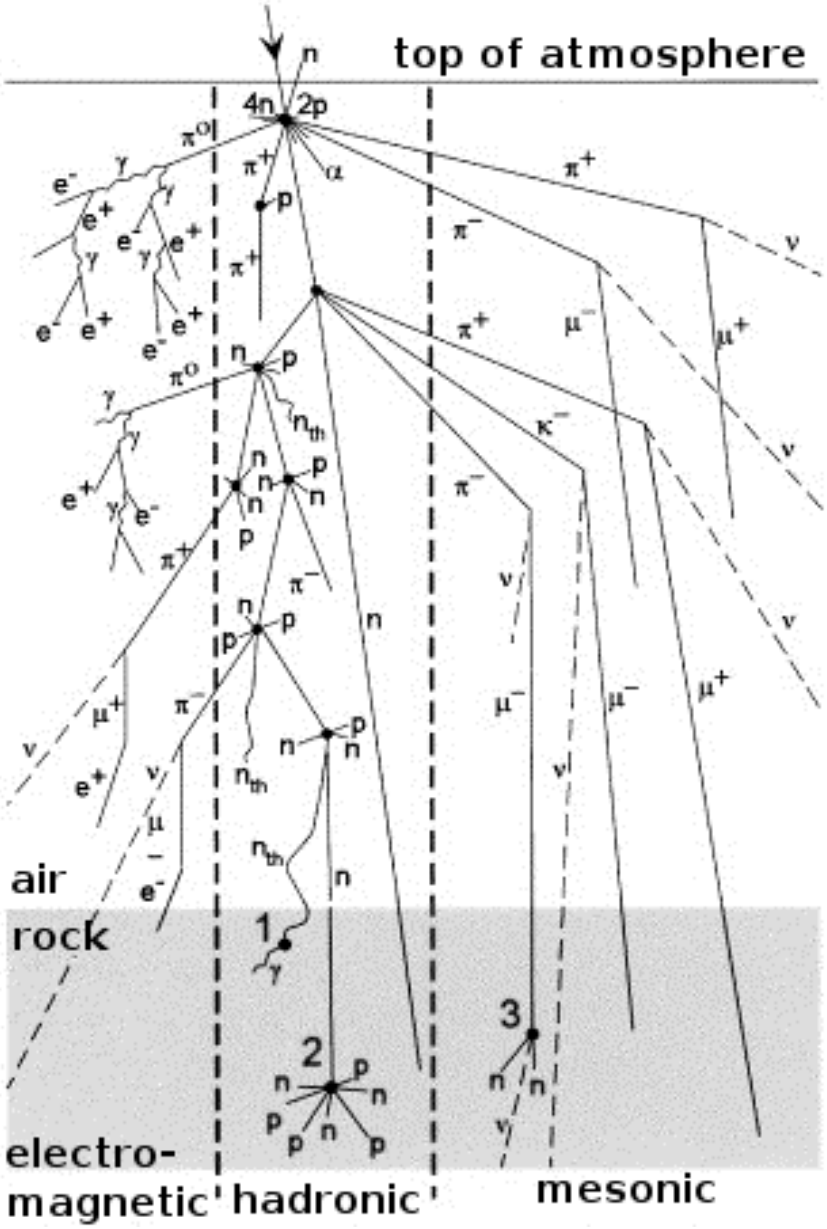

Figure 2.1.: Illustration of possible reactions taking place in the atmosphere and in rocks. The reactions are split in electromagnetic, hadronic and mesonic categories, according to the incident particle. This graphic is taken from the work of Gosse and Phillips [2001].

The resulting excited state of the new nucleus is typically de-excited by the emission of neutrons [Charalambus, 1971].

$$\mu^- + (Z, A) \rightarrow (Z-1, A)^* + \nu_\mu \rightarrow (Z-1, A-X) + X \cdot n + \nu_\mu \tag{2.3}$$

Due to the emission of neutrons, the production of ^{36}Cl by muon reactions can happen either directly by a reaction like ^{40}Ca(μ^-,α)^{36}Cl, or indirectly by the absorption of an emitted neutron.

The thermal neutron absorption on the nuclide ^{35}Cl produces the rare isotope in the reaction ^{35}Cl(n,γ)^{36}Cl. The cross section for thermalized (n,γ)-reactions on ^{35}Cl is 43.63 barn [NNDC, 2018]. Due to this high cross section a substantial amount of the radionuclide is formed in this manner. Compared to the cosmic radiation, a small fraction of the neutron flux originates from the spontaneous fission of Uranium and other reactions involving the natural decay chains. This maintains a measurable subsurface background of ^{36}Cl [Gosse and Phillips, 2001; Fabryka-Martin, 1988].

A detailed calibration of ^{36}Cl production rates by cosmic radiation can be found in the work of Marrero et al. [2016], which is part of the CRONUS-Earth project [Phillips et al., 2016].

Anthropogenic contribution

As already mentioned the production of ^{36}Cl can be achieved by thermal neutron absorption on ^{35}Cl. Due to the large cross section (43.63 barn, [NNDC, 2018]) any process emitting neutrons can create the radionuclide if a certain amount of chlorine is exposed to the flux.

The best example for the production of a high neutron flux by mankind would be the nuclear weapon tests, which started in 1945 with the Trinity experiment in New Mexico, USA. The weapon tests conducted at the Bikini and Eniwetok Atolls from 1952 to 1958 are responsible for most of the global anthropogenic ^{36}Cl, because they were close to the abundant chloride in sea water [Phillips, 2000].

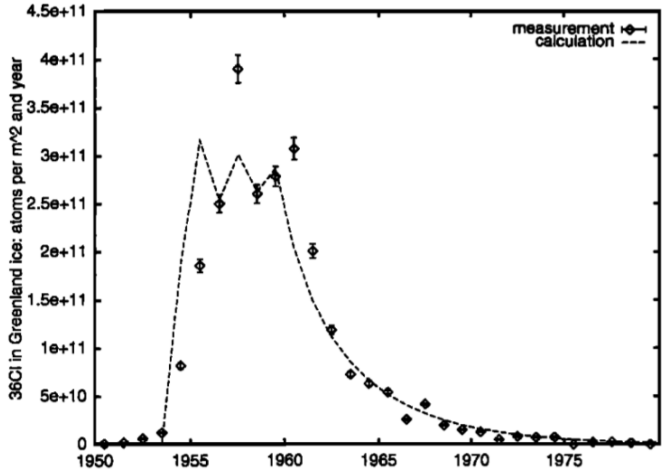

Figure 2.2.: This graphic is taken from Zerle et al. [1997] and shows his calculations for the bomb peak and the measured concentrations in greenland ice from Synal et al. [1990].

Calculations by Zerle et al. [1997] showed that during a nuclear weapon test on barges approximately 17 % of the released neutrons produced ^{36}Cl, which was also brought up to the stratosphere where it could contribute to the global distribution. Data from [Synal et al., 1990] and Zerle et al. [1997] shows that major fallout started in 1954 (Figure 2.2), when the first thermonuclear explosions on barges were tested [Phillips, 2000].

Besides the production during the nuclear weapon tests, ^{36}Cl is also released into the environment during nuclear fuel reprocessing. In the articles by Beasley et al. [1992, 1993] the emission of ^{36}Cl at the two reprocessing facilities Idaho National Engineering Laboratory (INEL) and Savannah River Site (SRS) was investigated. According to these papers both sites showed evidence of ^{36}Cl releases into the environment. This emission is expected to happen during the dissolution process, where the previously produced radionuclides get incorporated in chlorine gas and nitrosyl chloride following the formula [Beasley et al., 1992, 1993]:

$$HNO_3 + 3\,H^{36}Cl \rightleftharpoons {}^{36}Cl_2 + N^{36}Cl + 2\,H_2O \tag{2.4}$$

The actual production of the radionuclide is assumed to take place in nuclear reactors, due to thermal neutron capture on ^{35}Cl impurities in and on the nuclear fuel elements.

2.1.2. Applications of ^{36}Cl

The radiogenic nature of the isotope ^{36}Cl in addition to the natural and anthropogenic production rate P (here assumed to be constant) give the following time evolution for the number of radionuclides N(t) :

$$N(t) = N_0 e^{-\lambda t} + \frac{P}{\lambda}(1 - e^{-\lambda t}) \tag{2.5}$$

Here N_0 is the initial amount of ^{36}Cl at the time t=0 and λ is the decay constant, which is indirect proportional to the half-life. After 5 times the half-life of the nuclide, the activity reaches about 97 % of the production rate and in the limit t$\rightarrow \infty$ the activity of the radionuclide equals the production rate. The isotope ^{36}Cl has a half-life of (301$\pm$2) kyrs [NNDC, 2018], but the production rates of the individual channels are difficult to decifer and therefore it is used for dating events up to 1 Myrs ago [Gosse and Phillips, 2001; Phillips, 2000].

By looking at the relative abundance of chlorine in the environment one can already guess that the main applications of ^{36}Cl involves the dating of geological events regarding the Earth's crust and water reservoirs.

The dating of an event at the Earth's crust is referred to as surface exposure dating. This term describes the dating of a surface or the determination of the duration a specific geological site is exposed to cosmic radiation. In order to date geological events as accurate as possible, the production of the investigated nuclide at the site has to be known to an appropriate level. A good overview of surface exposure dating, using terrestrial in situ cosmogenic nuclides, can be found in the work of Gosse and Phillips [2001]. Typical target minerals for cosmogenic ^{36}Cl productions caused by spallation are K-Spar, Plag and Calcite [Gosse and Phillips, 2001]. An example for surface exposure dating using exclusively ^{36}Cl is the determination of slip events at the magnola fault, located in central Italy by Palumbo et al. [2004]

and Schlagenhauf et al. [2010]. Their works show evidence of strong earthquakes during the holocene and reveal information that can be used for seismic hazard estimations.

In hydrology the isotope ratio of Chlorine can be used to determine very old groundwater and younger groundwater by making use of the ^{36}Cl isotopes originating form the nuclear weapons tests. Chloride, where chlorine is in the form of an negative ion, introduced into water is advected the same way as its surrounding and is resistant to geochemical processes [Phillips, 2000]. This led to its use as a hydrological tracer, which was first recognized by Davis and Schaeffer [1955]. An example for dating old groundwater would be the investigations of Bentley et al. [1986]. The greatest problem according to Davis et al. [1998] is the determination of the initial concentration of ^{36}Cl in most hydrogeological settings. In the work of Argento et al. [2010] sea water was investigated and an average ^{36}Cl/Cl ratio of $(0.5\pm0.3)\cdot10^{-15}$ was determined.

2.2. Vienna Environmental Research Accelerator (VERA)

The Vienna Environmental Research Accelerator (VERA) is an AMS facility at the University of Vienna, which was financed by the Austrian Federal Ministry of Science and Research in the year 1993 [Kutschera et al., 1997]. In 1996, half a year after the installation, first performance tests showed precision of radiocarbon measurements close to expectations [Priller et al., 1997]. The system was improved even further to measure heavy isotopes (e.g. ^{236}U, ^{244}Pu) and light isotopes (e.g. ^{10}Be, ^{26}Al) [Steier et al., 2004]. Even the measurement of ^{36}Cl became feasible, by separation of the isobaric sulfur isotope using their characteristic energy loss [Martschini et al., 2013].

A scheme of the current state of the AMS system is shown in Figure 2.3 and already includes the Ion Laser InterAction Mass Specrtometry (ILIAMS) setup, which was finished during the time span of this master's thesis.

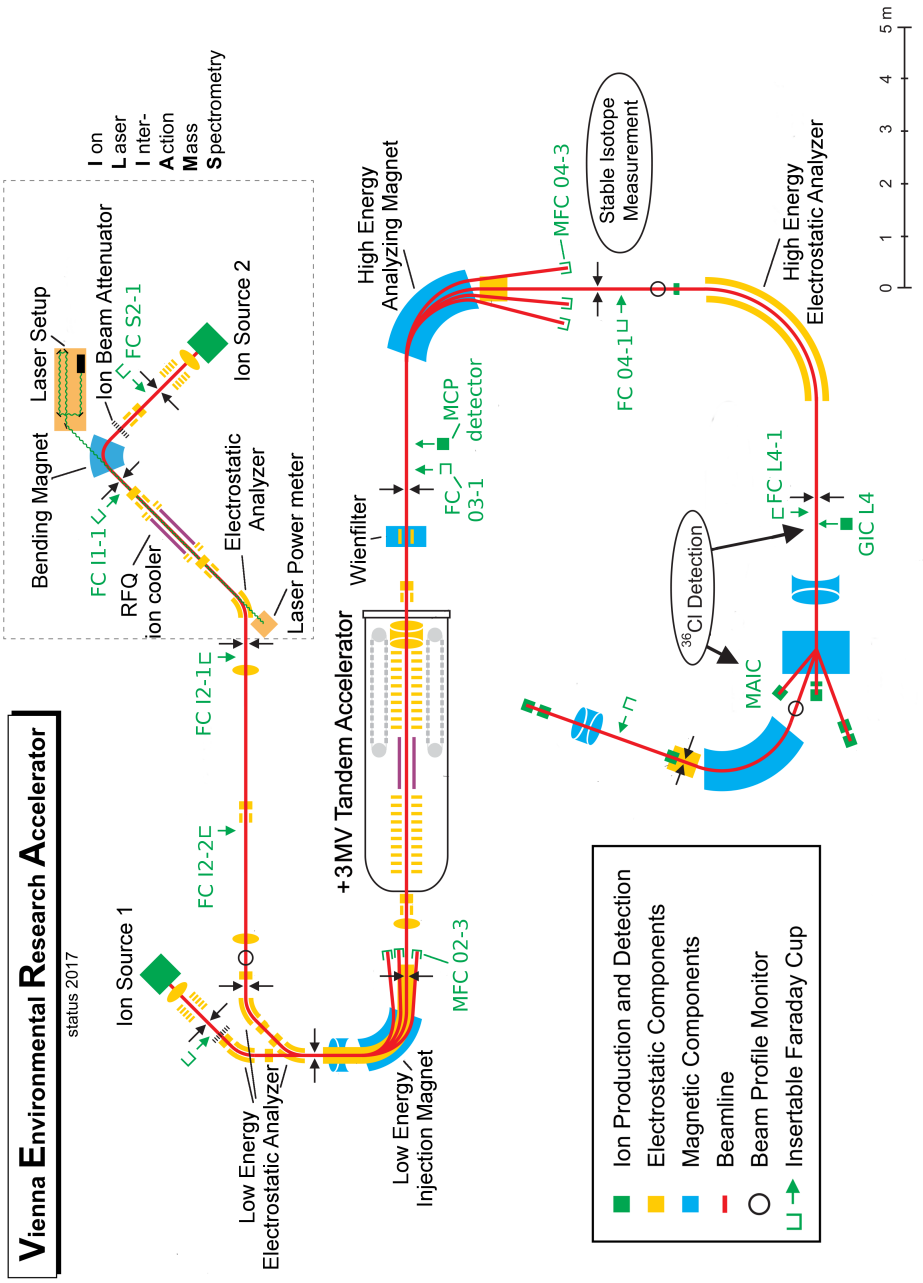

Figure 2.3.: A scheme of the VERA setup in late 2017. The important measurement points and components used in this master's thesis are labeled. A more detailed scheme can be found in Appendix A.

Besides the ILIAMS part, the facility resembles a typical AMS facility. The ions are produced in a Source of Negative Ions by Cesium Sputtering (SNICS) made by the National Electrostatics Corporation (NEC). It is followed by an electrostatic spherical analyzer (ESA) and an injection magnet, which filter the mass of the isotope of interest on the low energy side of the the accelerator. A 3 MV Pelletron tandem accelerator constructed by NEC is the key element of the system and allows stripping of the injected anions with either a gas or a foil. The extracted and accelerated ions can be again filtered by a Wienfilter, an analyzing magnet and an ESA, before detection in one of VERA's various detector beam lines is done. Stable isotope currents can be measured in offset Faraday cups located behind each bending magnet. A Multi Beam Switcher (MBS) at the injection magnet allows fast sequentially injection of different masses into the accelerator. The ion optical elements (e.g. steerers and lenses) and beam diagnostic components (e.g. Faraday cups and beam profile monitors) allow efficient tuning of the various isotopes measured at the facility.

2.2.1. Previous ^{36}Cl measurement routine at VERA

The work of Martschini et al. [2013] proved that ^{36}Cl measurements are possible with the 3 MV tandem accelerator of VERA. The separation of ^{36}S from the isotope of interest ^{36}Cl was done using a $\Delta E/E$ detection setup. By using a ionization chamber with a split anode, the difference in energy loss could be detected (Figure 2.4). Since the ^{36}Cl nucleus contains one proton more than the isobar ^{36}S, its stopping power is higher at the first anode section (E_1), while ^{36}S shows slightly higher energy loss in the second detection volume (E_2). According to Martschini [2012] the capability to distinguish between the isobars can be seen at first order as their separation s:

$$s = \frac{\Delta E_{12}}{\sqrt{\delta E_1^2 + \delta E_2^2}} \tag{2.6}$$

In this context, $\delta E_{1/2}$ are the widths of individual peaks, which are correlated to energy straggling and energy resolution, and ΔE_{12} is the total energy loss difference inside the sensitive detector volume.

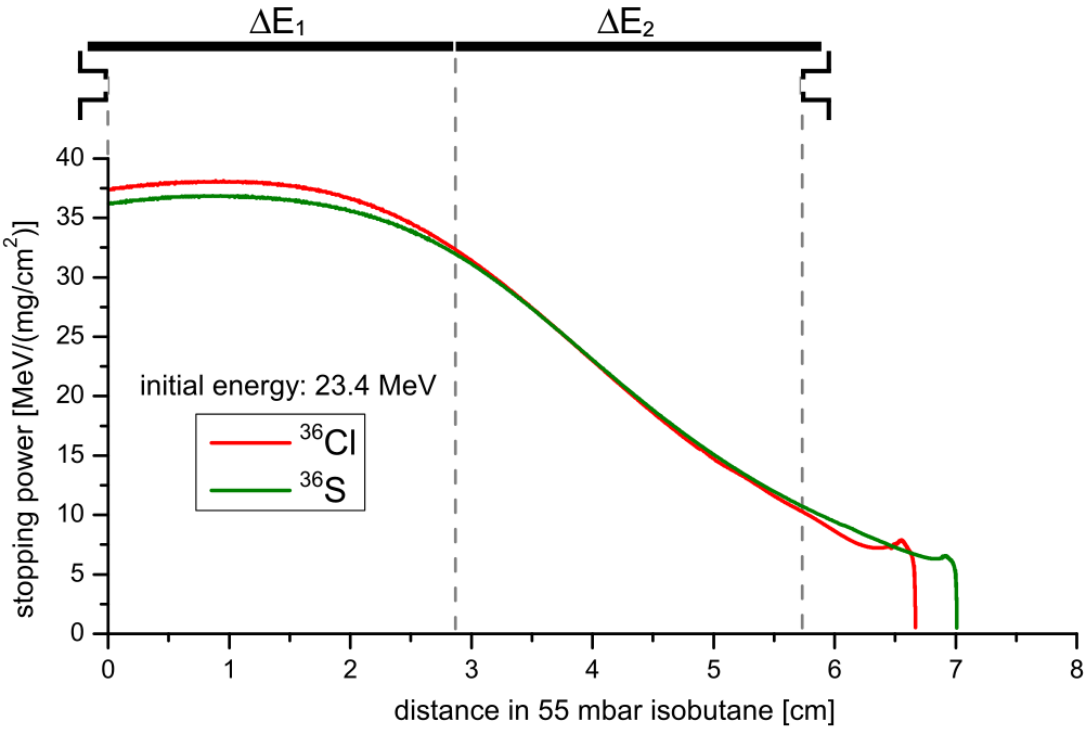

Figure 2.4.: The total stopping power of ^{36}Cl and ^{36}S with inital energy of 23.4 MeV is plotted against the travel distance inside a detector volume filled with 55mbar isobutane gas. The values ΔE_1 and ΔE_2 correspond to the measured energy loss inside the sensitive detector volume of Anode 1 and Anode 2, respectively. This figure is taken from the work of Martschini [2012] and uses the data from *SRIM* [Ziegler and Biersack, 2008].

In order to achieve sufficient separation high energies are required. To reach this particle energies with a 3 MV accelerator a high charge state had to be selected at the high energy side. At VERA ^{36}Cl measurements using this energy loss method were carried out in the charge state 7+ and a stripping foil made out of carbon was used to increase its yield. In addition to the separation in the detection stage, the overall sulfur output of the source was reduced by the use of a special cathode having selected low-sulfur backing material. The best results at VERA were achieved with an in-house produced silver bromide backing material. The required amount of sample material per cathode depended on its expected isotope ratio and ranged from 0.5 to 2 mg [Martschini et al., 2013].

2.3. Laser photodetachment

The photodetachment process describes the detachment of an electron from an negatively charged ion (A^-), resulting in a free electron (e^-) and the neutral state (A).

$$A^- + \gamma \rightarrow A + e^- \tag{2.7}$$

Before going into the details of the process, the binding properties of a negative charged ion, also called anion, will be discussed. Since for this thesis the focus lies on the application for chlorine measurements in AMS, only atomic anions will be discussed. More information about molecular anions can be found in the work of Rienstra-Kiracofe et al. [2002].

2.3.1. Atomic negative ions

The additional electron introduced to a neutral atom does not feel any long ranged attracting Coulomb force. However, if the charged electron is near a neutral atom the electron will polarize the atom and the induced electric dipole moment attracts the electron. The binding energy gained by the formation of a negative ion is also called the electron affinity (EA). A definition of the electron affinity was given by Hotop and Lineberger [1975]:

*"The electron affinity EA of an atom A is the difference between the total energies (E_{tot}) of the ground states of A and its negative ion A^-."*Hotop and Lineberger [1975, page 541]

$$EA = E_{tot}(A) - E_{tot}(A^-) \tag{2.8}$$

The dipole potential responsible for binding the electron to the atom is proportional to r^{-4}. In contrast to the ionization potential, which has to be overcome in order to form a positive ion, the electron affinity is typically one order of magnitude smaller [Drake, 2006]. Some values for ionization potentials and electron affinities are listed in Table 2.2. The energy levels of hydrogen and the corresponding anion is shown in Figure 2.5.

Name	Formula	electron affinity in eV	ionization potential in eV
Hydrogene	H	0.754 195(19)	13.598 443
Oxygen	O	1.461 113 5(9)	13.618 05
Fluorine	F	3.401 189 7(24)	17.4228
Sulfur	^{32}S	2.077 104 03(51)	10.360 01
	^{34}S	2.077 104 3(11)	10.360 01
Chlorine	Cl	3.612 725(27)	12.967 63

Table 2.2.: List of some atomic ionization potentials and electron affinities in eV. The ionization potential and electron affinity values are taken from [Rumble, 2018].

For the element Sulfur an isotopic shift was measured between the stable isotopes ^{32}S and ^{34}S. The difference is in the order of 0.1 µeV and since the gap in electron affinity of unwanted and interesting isotope is often in the order of eV (EA(Cl)-EA(S)$>$ 1.5 eV), it is not relevant for isobaric suppression,

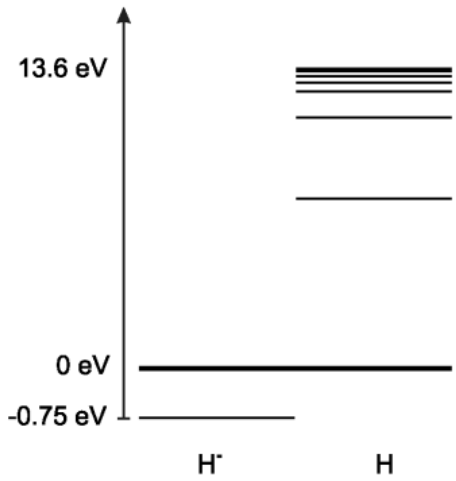

Figure 2.5.: A schematic drawing of the energy levels of H and the anion H^-. This figure is taken from the work of Andersson et al. [2009].

2.3.2. Photodetachment cross-section

The cross section of the photodetachment proccess near threshold can be described by the Wigner law [Wigner, 1948]:

$$\sigma \propto k^{2l+1} \tag{2.9}$$

In this context, k represents the linear momentum and l the angular quantum number of the outgoing electron. In the case of photodetachment one usually rewrites equation 2.9 in terms of photon energy (E_γ) and the threshold energy, which corresponds to the electron affinity (EA):

$$\sigma(E_\gamma) \begin{cases} \propto (E_\gamma - EA)^{\Delta l+1/2} & \text{, for } E_\gamma \geq EA \\ = 0 & \text{, for } E_\gamma \leq EA \end{cases} \tag{2.10}$$

The angular quantum number of the photon is $l = 1$. Therefore, the selection rule implies a change of $\Delta l = \pm 1$ is applied to the final system of neutral atom and electron. If an electron occupying an s-state ($l = 0$) in the initial ion is detached, it will be emitted with a quantum number of $l = 1$, which is referred to as p-wave. For higher initial angular quantum number of the detached electron, the change $\Delta l = -1$ will dominate, since higher angular momentum is suppressed by the centrifugal barrier [Andersson, 2009]. Because of this the detachment of an p-state electron in the anion results mostly in an emitted s-wave ($l = 0$) electron.

As already stated before, the Wigner law only holds near threshold and according to Farley [1989]:

"The law is said to 'hold' if the deviation between the law and reality is less than some arbitrary fraction. In other words, there is no theoretical guideline for either the range or the accuracy of the Wigner law." Farley [1989, page 6286]

In his work Farley also stated that the Wigner law is only the first term in the expansion of a yet unknown exact solution. Therefore, the cross section at higher energy diverges from the Wigner law due to higher order terms in k. Corrections

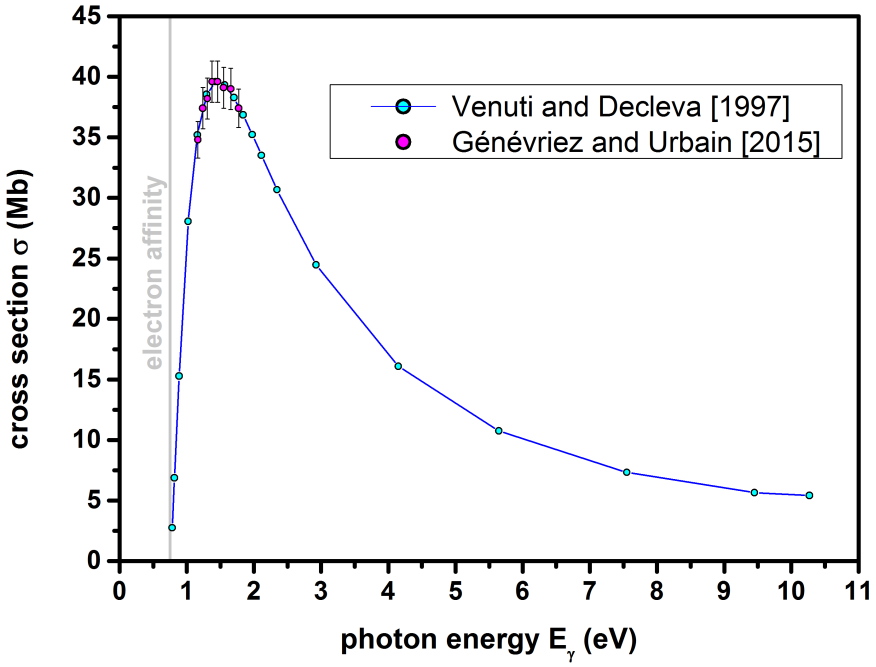

Figure 2.6.: The experimental values of Génévriez and Urbain [2015] and the theoretical values of Venuti and Decleva [1997] for the photodetachment cross section of Hydrogene are plotted and show decreasing cross section at higher energies.

for this have been calculated by O'Malley [1965] and Farley [1989]. The correction term determined by O'Malley [1965] involved long-range multipole forces between the detached electron and the neutral atom. The paper of Farley [1989] reports a model calculation using a zero-core-contribution (ZCC) approximation. A newer approach for the calculation of photodetachment cross sections was done by Liu and Ning [2015] using density functional theory (DFT). The anion H^- is the simplest of its kind, hence the theoretical calculations are the most accurate. The model of Venuti and Decleva [1997] has proven very robust and matches new experimental cross section data measured by Génévriez and Urbain [2015] (Figure 2.6). Both, the experiment and the theory of the hydrogen cross section, show decreasing behavior after a maximum at around 1.45 eV. This behavior is assumed to be general for photodetachment and Andersson [2009] stated in his work that this comes from the decreasing overlap integral of initial and emitted electron wave functions at high photon energies.

2.3.3. Suppression by photodetachment

In addition to the cross section σ the detachment probability p depends on the photon flux ϕ and the interaction time t in the following way:

$$p = 1 - e^{-\sigma\phi t} \tag{2.11}$$

The Figure 2.7 the detachment probability as a function of interaction time for different laser powers. For the calculations a laser wavelength of 532 nm (2.33 eV) and 2.25 mm spot size was used. Based on the hydrogen data a cross section of 10 Mbarn was chosen.

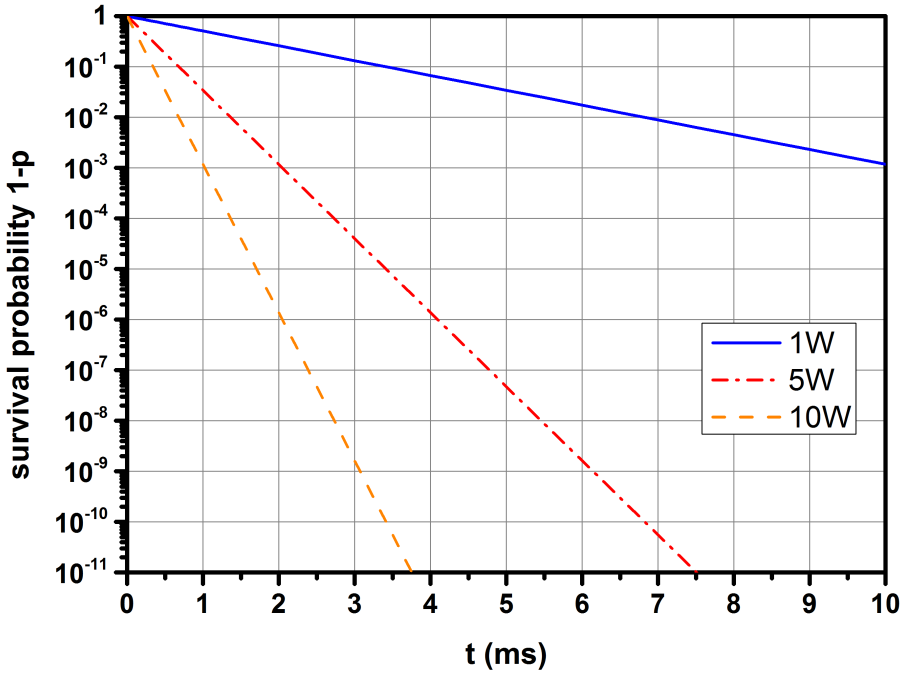

Figure 2.7.: Time dependence of the ion survival probability for photodetachment at different laser powers. Calculations assume a laser with 532 nm wavelength, a laser spot size of 2.25 mm diameter and a cross section of 10 Mbarn.

In AMS applications the typical energy extracted from an ion source is in the order of 50 keV. For an interaction of an ^{36}S ion beam of 10 keV energy with a laser for

a duration of 1 ms an overlap has to be guaranteed for a distance of around 230 m. A beamline of this length is not efficient. Therefore, the better solution is to slow down the ions to thermal energies.

2.3.4. Ion Laser InterAction Setup (ILIAS)

As stated in the previous chapters the photodetachment process can be used for suppression of an isobaric interference with lower electron affinity than the isotope of interest. The Ion Laser InterAction Setup (ILIAS) was constructed with the goal to explore the selective laser photodetachment filtering method and its application for AMS. The ILIAS project was located in a basement lab in the neighboring building and was operated independently of the already existing AMS facility VERA. Due to its very promising results, the main parts of the setup have already been integrated into the VERA facility, which is better described in Chapter 3.

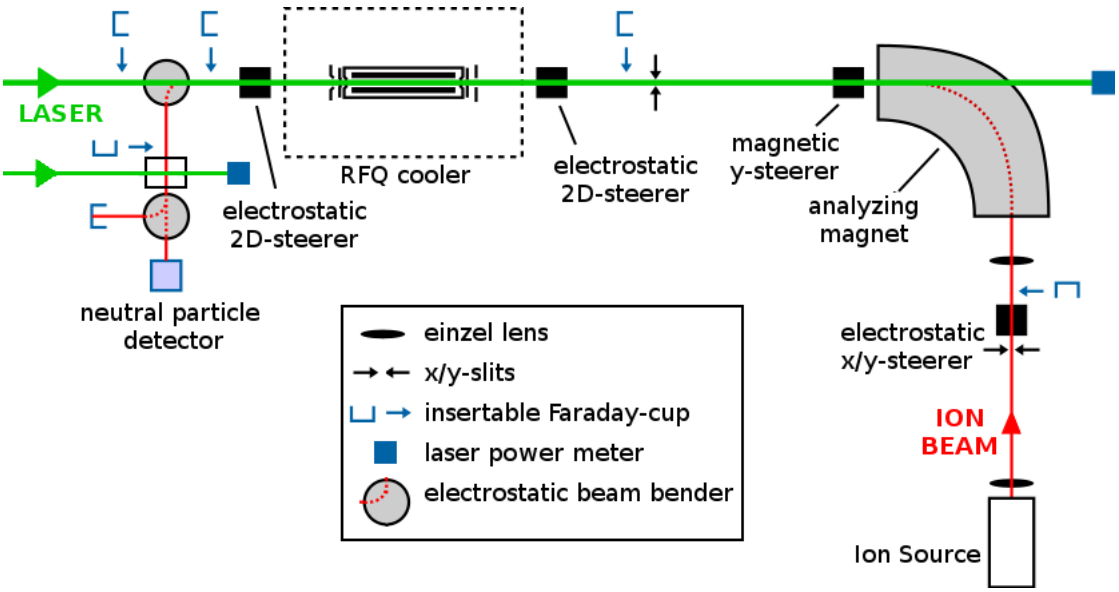

Figure 2.8.: Schematic drawing of the ILIAS setup.

The outline of ILIAS resembles a simple mass spectrometry system (Figure 2.8). A single cathode cesium sputtering ion source (SNICS II by National Electrostatics Corporation in Wisconsin, USA) was used to create negative ions, which are accelerated to energies up to 30 keV. An analyzing magnet was used for momentum over charge filtering before the ion beam was injected into a RFQ cooler.

During the residence time in the cooler a laser interacted with the ion beam for photodetachment measurements. After the cooler followed an electrostatic bender, multiple Faraday cups and detectors, which were used for different investigations on the system.

The principle behind the RFQ cooler is a linear Paul trap. The ions are trapped to the centered z-axis of the cooler by a force proportional to their radial distance. By assuming that the four quadrupole electrodes extend infinite in z-direction the potential can be approximated as

$$\Phi(\vec{r}, t) = \frac{\Phi_0(t)}{r_0^2}(x^2 - y^2) \tag{2.12}$$

with the potential $\pm\Phi_0(t)$ applied to the parallel electrode pairs, the inscribed circle radius r_0 of the RF-electrodes and the transversal Cartesian coordinates x and y.

The ion's equations of motion can be derived by this potential and results in a differential equation, which is referred to as *Mathieu equation*. This equation has a set of solutions, which are defined by the Mathieu parameters

$$q := \frac{4QU_{RF}}{mr_0^2\omega_{RF}^2} \qquad and \qquad a := \frac{8QU_{DC}}{mr_0^2\omega_{RF}^2} \tag{2.13}$$

Here Q and m are the electric charge and mass of the ion, r_0 is the inscribed circle radius of the RF-electrodes and the electrode potential $\Phi(t)$ is characterized by a DC voltage U_{DC} and an AC contribution with amplitude U_{RF} and circular frequency ω_{RF}.

In general, a linear Paul trap can be used as a mass filter, where the electrode potential can be used to select different masses. The RFQ cooler used in photodetachment investigations does not require the selection of a mass and therefore the additional DC contribution is not used ($U_{DC} = 0$).

The absence of the DC potential leaves only the parameter q defined by the AC contribution. At a=0 stable trajectories inside the cooler require a value of $|q| < 0.908$ [Pitters, 2015]. Therefore, the ion guide works as an high pass filter and allows stable trajectories for ions with mass

$$m > \left| \frac{4QU_{RF}}{0.908 \cdot r_0^2 \omega_{RF}^2} \right| \tag{2.14}$$

The additional electron in an anion is weakly bond and therefore collisional detachment during the injection of the ion beam into the gas filled cooler has to be prevented. The work of Pitters [2015] involved the construction of a electrostatic deceleration stage, before the injected ions collide with the buffer gas. The transmission through the cooler was investigated and improved by Moreau [2016]. The improvements involve the construction of 2D-steerers at the entrance and exit of the cooler. The transmission measurements of a $^{63}Cu^-$ ion beam through the cooler showed that higher injection currents result in lower transmission values (Figure 2.9).

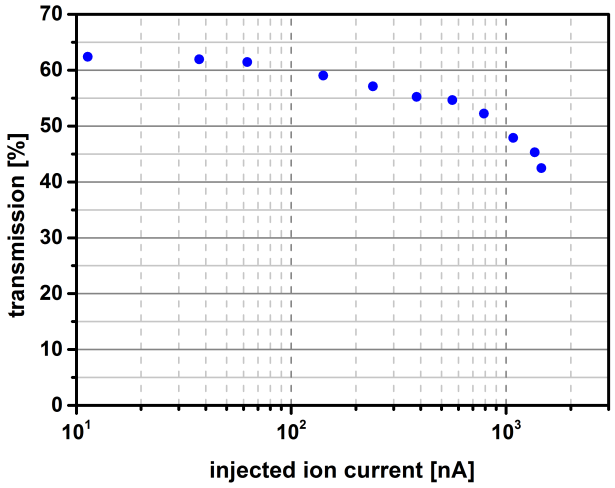

Figure 2.9.: Cooler transmission of a $^{63}Cu^-$ ion beam as a function of the injected current. While injecting a current lower than 100 nA, transmission values greater than 60 % were observed. This graphic is taken from [Moreau, 2016].

The RFQ potential confines the ions to a narrow beam at the center of the electrodes. The collisions between the decelerated ions and the buffer gas, typically helium, are foremost elastic and damp the oscillation in the quadrupole. According to simulations done by Pitters [2015] the ions are trapped within a radial distance of 0.5 mm. These simulation also result in a mean kinetic energy of 0.08(2) eV for the trapped ions. By reaching the simulated equilibrium values the residence time was calculated to be in the order of ms, increasing with higher buffer gas pressure.

Experimental measurements on the residence time of ions in the RFQ cooler were done by [Moreau, 2016]. The setup involved a fast switching steerer for interruption of the injected ion beam. After an interruption the extracted ion current was measured over time. This data was afterwards used to determine the residence distribution during unloading of the cooler. Different cooler settings and injected current values were investigated. The most relevant results are presented in Figure 2.10. A decreasing residence time was observed for increasing injection current, increasing guiding field strength and decreasing gas pressure. The injected current has the most visible effect on the residence time. Between the current values 32 pA and 460 nA the maxima of the respective residence time distributions are more then one order of magnitude apart and range from 0.4 to 7 ms.

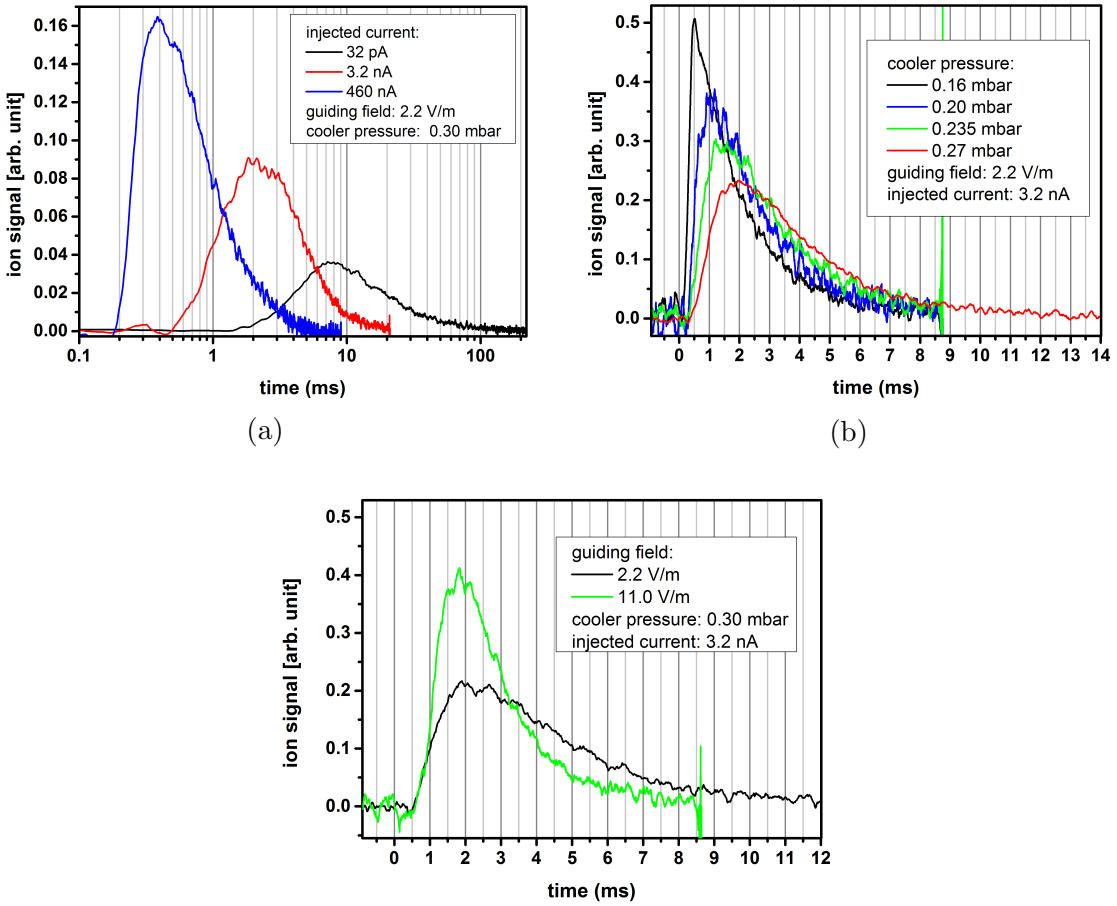

(a) (b)

(c)

Figure 2.10.: Current (a), cooler pressure (b) and guiding field (c) dependency of the unloading residence time distribution. These graphics are taken from the work of Moreau [2016]. During the measurement the injected current was interrupted while the decrease of the extracted current was measured (unloading of the cooler).

3. Integration of ILIAS into VERA

After the promising results of the ILIAS project for the application in AMS, the construction of a new beamline coupled to VERA was undertaken. The new beamline contains the most relevant parts of ILIAS. The combination of ILIAS and VERA enables us to perform Ion Laser InterAction Mass Spectrometry (ILIAMS), which is the new name for the method. It is located in an extension to the accelerator hall. This chapter is designed to present some phase-space measurements on the output of the ILIAMS-ion source, prior to the AMS experiments done on the combined system. The new beamline will be described in a separate section of this chapter to present the possibilities of the system.

3.1. Phase space measurements

A MC-SNICS from NEC (previously described by Priller et al. [2010]) is mounted at the beginning of the newly installed low energy beamline. The new beamline allowed first photodetachment investigations on the new system without affecting the routine measurements at VERA.

The phase space of the ion beam, emitted by the ion source, potentially affects the cooler injection. The injection of the ion cooler consists of an deceleration stage followed by an aperture of 3 mm in diameter. A blow up of the ion beam during deceleration in combination with the aperture is critical for the transmission through the ion cooler. Therefore the phase space was measured before the construction of the ILIAMS beamline was finished.

The phase space describes each particle state possible in the system. In three-dimensional space it is usually spanned by the position vector $\vec{r} = (x, y, z)$ and

the momentum vector $\vec{p} = (p_x, p_y, p_z)$, resulting in a six-dimensional hyper-volume. Each particle is represented by a single point in this volume and changes its coordinates according to its equations of motions. In ion beam optics the default path of the particles is typically used as the z-axis, pointing in the beam's flight direction. It corresponds to the designed beam path, which is usually the center of the beamline. Therefore, deviations from the intended path are only in the plane spanned by the x- and y-axis, which build a left-handed orthogonal system with the z-axis. The measurement of the particle momenta p_x and p_y is more challenging than the determination of the beam divergences $\frac{dx}{dz}$ and $\frac{dy}{dz}$ from the center. Therefore the reduced phase space (x,y,$\frac{dx}{dz}$,$\frac{dy}{dz}$) will be used in the following. This simplification assumes a constant momentum p_z in direction of the default path and a beam divergence equal to the respective ratio of momenta (e.g. $\frac{dx}{dz} = \frac{p_x}{p_z}$). An ion beam consists of many particles and it is more convenient to present a phase space distribution I, which depends on the ions' coordinates, their positions $(x(z), y(z))$ and the corresponding z derivatives ($\frac{dx}{dz}$,$\frac{dy}{dz}$). To present this phase space distribution, the contributions $I(x, \frac{dx}{dz})$ and $I(y, \frac{dy}{dz})$ will be plotted separately.

3.1.1. Measurement setup

For the phase space investigations used carbon samples without visible cratering were chosen as targets. They still yielded a sufficient source output in the order of µA. The measurements were done using a combination of a two dimensional beam slit, to select narrow parts of the beam in x- and y-direction, and a beam profile monitor (BPM, NEC type BPM80), for measuring the resulting current distribution after a known distance.

The measurement principle is illustrated in Figure 3.1 and shows the measurement of the phase space in y-direction. The rotation axis of the BPM helix wire is tilted by 45°. In the illustrated example, the exposed wire segment therefore moves parallel to the x-axis while measuring the current distribution in the perpendicular y-direction. Phase space measurements were conducted at two positions, before and after the bending magnet (see Figure 3.2). To distinguish between them they are named SETUP1 (after the source) and SETUP2 (after the magnet).

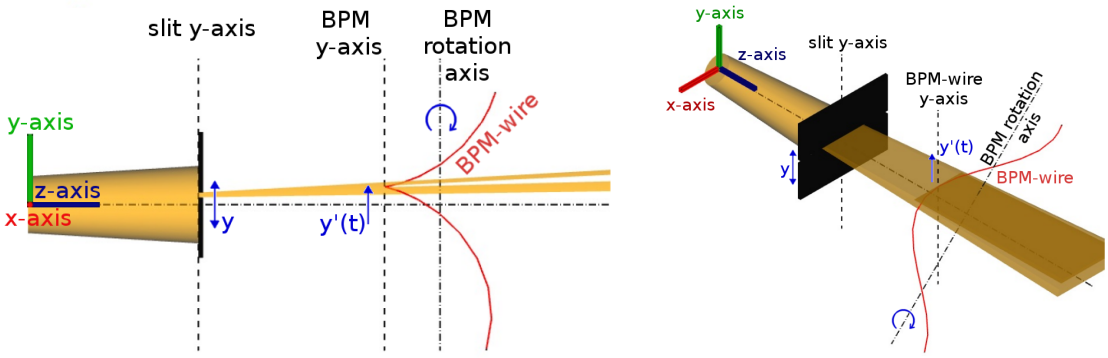

(a) (b)

Figure 3.1.: A 2D (a) and 3D (b) schematic drawing of the principle behind a phase space measurement in y-direction. The center of the slit position y can be set manually, while the motor driven rotation of the BPM helix scans the beam intensity at position y'(t). In (a) it is visible that a beam segment cut out by the slits may diverge again and therefore a $\frac{dy}{dz}$ distribution can be calculated at each slit position y.

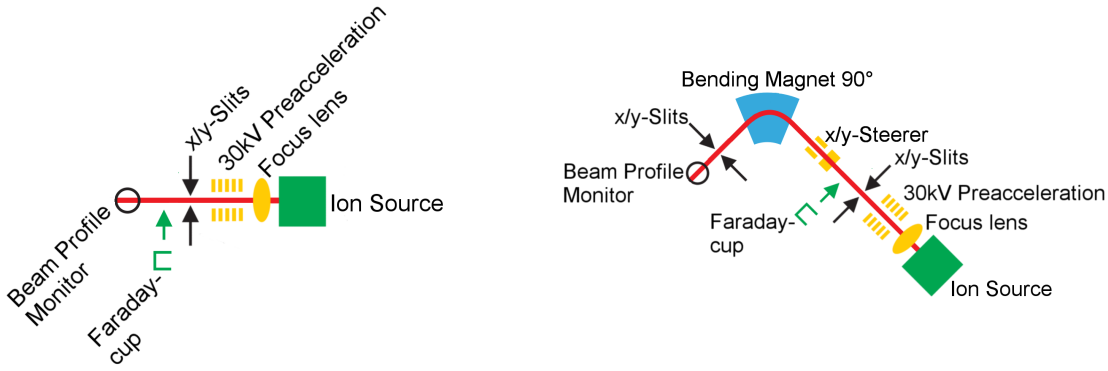

(a) (b)

Figure 3.2.: Schemes of SETUP1 (a) and SETUP2 (b). Both show different stages of the ILIAMS beamline construction.

In the following only the measurement of a phase space in the y-direction will be described, but the measurement in x-direction is analogous.

The phase space measurement in y-direction involved recording the BPM current distribution $I(y, y')$ for 9 equidistant slit positions y, ranging from -4 mm to 4 mm distance to the default path. The position y refers to the center of the slit and the gap between slit elements was set to 1 mm. During the acquisition of BPM data the x slit was "open", meaning a centered slit with a 10 mm gap. By knowing the slit position y, the BPM wire position y'(t) and the distance d between slit and BPM y-axis, the beam divergence at the slit position can be approximated by

$$\frac{dy}{dz} \approx \frac{y' - y}{d} \tag{3.1}$$

and the current distribution can be written as $I(y, \frac{dy}{dz})$, which is an estimation of the phase space distribution of the particles passing through the slit at position y.

The measurement results presented here are not exact, because this would require infinitesimally thin measures of the slit and the diameter of the BPM wire. The measured phase space corresponds to a convolution of the theoretical phase space with two rectangular functions, one for the slit gap and one for the wire diameter. The slit distance was set to (1.00±0.14) mm during each measurement and according to the manufacturer the scanning wire has a diameter of 0.5 mm. In theory the parallel component of the ion beam ($\frac{dy}{dz} = 0$) is measured at y'=y. Because of the finite dimensions of the slit and wire, ions with a derivative in the range of $\pm 1.33\,\frac{mm}{m}$ additionally contribute to the BPM signal during SETUP1 measurements. In SETUP2 the derivatives in the range of $\pm 2.77\,\frac{mm}{m}$ contribute tto the parallel measurement, due to the smaller distance between slits and wire.

The x-axis distance d between slit and BPM was 647 mm and 324 mm for SETUP1 and SETUP2, respectively. The y-axis distance d between slit and BPM was measured to be 563 mm for SETUP1 and 270 mm for SETUP2. The x/y-slit of SETUP1 was mounted to a small venting flange, which was then connected to the source's exit (flange of the pre-acceleration stage). The distance from the source's

pre-acceleration exit flange to the x- and y- axis of the slit was about 210 mm and 240 mm, respectively. During the SETUP2 measurements the x/y-slit, used for phase space measurements was separated from the bending magnet flange by a bellows. The distance between the tangent crossing point of the bending magnet and the x- and y-axis of the slit was measured as 750 mm and 760 mm respectively. A simple ruler was used to measure the distances, hence the uncertainty is estimated to be ± 1 mm.

The BPM signals were read out by a digital oscilloscope (Tektronix® TDS2024C). During each phase space measurement the fiducial signal (see Figure 3.3), used for position conversion, was measured once. Then the current distribution of each slit position was recorded. During measurements on SETUP1 the Faraday cup in front of the beam profile monitor allowed to measure and correct source output drifts. In SETUP2 a Faraday cup could not be integrated, because the already mounted RFQ cooler limited the available space behind the magnet. In order to apply a correction for the source output drift, the ion current during SETUP2 measurements was calculated by using the BPM wire signal. A conversion factor k was used to transfer the integrated BPM signal into an ion current. It was calculated using the data from SETUP1 measurements. Five SETUP1 measurements were used to determine a mean conversion factor of

$$k = \frac{\int_{BPM}}{I_{FC}} = (1.307 \pm 0.022) \cdot 10^{-3} \, \frac{Vs}{A} \tag{3.2}$$

The currents obtained by the conversion of the integral differ from the Faraday cup measurements by less than 5 %.

3.1.2. Data evaluation

The BPM data was saved on a flash drive in the form of a simple ASCII file (example of the signals measured in Figure 3.3). The drawing in Figure 3.4 shows the main idea behind the data evaluation.

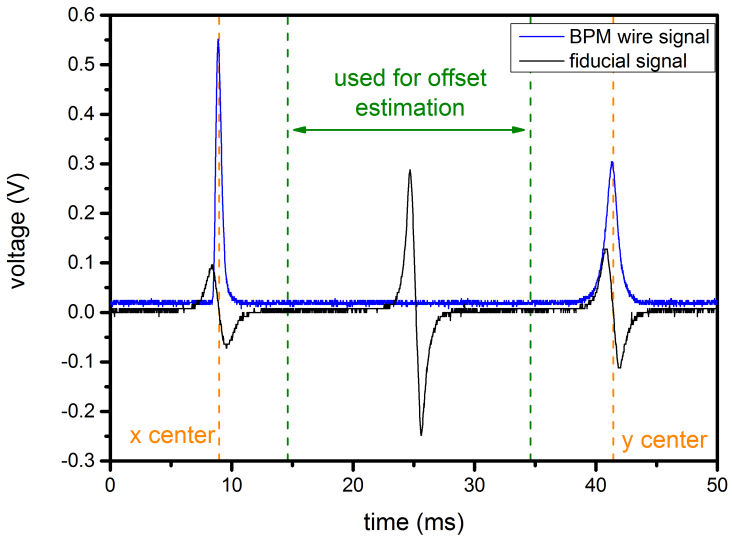

Figure 3.3.: Example of the BPM data recorded via an oscilloscope and used for phase space evaluation. The fiducial signal indicates the centers of the axes, marked by orange dashed lines. In the region between x- and y-beam profile, indicated by the green dashed lines, no beam current expected and was used for offset estimation.

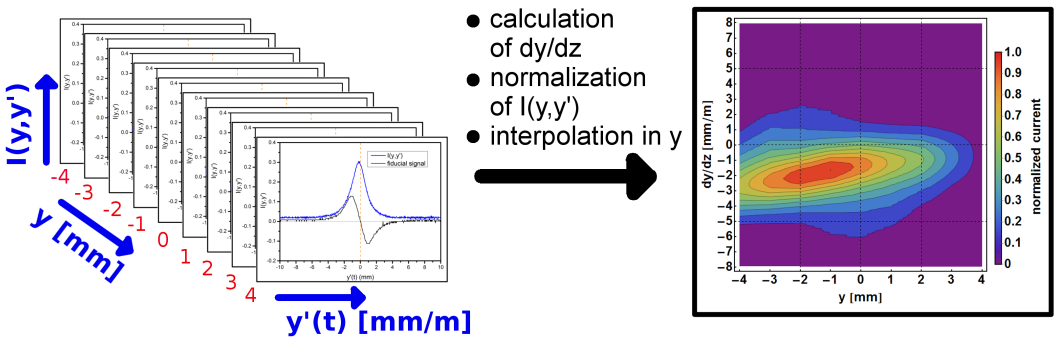

Figure 3.4.: Illustration of the phase space evaluation in y direction. The slit position y and BPM wire position y' were used to calculate the slope $\frac{dy}{dz}$ according to equation 3.1. The current distribution $I(y, y')$ is normalized and interpolated between the slit measurement points, before the contour plot of the approximated phase space distribution is created.

After importing the raw data files into a *Mathematica*® environment the following steps were done:

Offset correction

During the offset correction a selected part of the BPM signal (Figure 3.3) was averaged over time and afterwards subtracted from each voltage value of the wire signal. Since different measurements yielded different offset values, its correction allows better comparison of the evaluated phase space distributions.

Source drift correction

The positioning of the manually controlled slit and the recording of the BPM signal usually took 1-2 minutes. During the measurement of the phase space distribution the slit position was set 9 times per axis. This allows for a drift of the source output between these individual recordings. To compensate this behavior, the total ion beam current was used. It was obtained either via Faraday cup or conversion of an "open" (10 mm gap in x- and y-direction) BPM wire signal. The individual measurements of the ion beam current were linearly interpolated and evaluated at the start time of each BPM recording. The BPM signal of each slit position was then divided by the interpolated current.

Conversion of BPM wire signal axes

In order to transform the time signal into the position of the beam wire (i.e. $y'(t)$), values provided by the BPM's data sheet were used and resulted in the conversion factor

$$c = \frac{\Delta s_{fiducial}}{\Delta t_{fiducial}} = 1.85 \, \frac{mm}{ms} \tag{3.3}$$

The BPM wire signal combines the x and y data (see Figure 3.3). They had to be separated using the zero-crossings of the fiducial signal as a reference for the beamline center. The voltage signal provided by the beam profile monitor is proportional to the current measured by the BPM and was converted using the selected sensitivity (usually 10^{-6} A/V was set during measurements).

Calculation of the slope

In order to present the current distribution in the form $I(y, \frac{dy}{dz})$, the y' axis of the BPM wire signal was shifted by the respective slit position value y. Afterwards the resulting signal values were divided by the distance between slit and wire to obtain a distribution $I(\frac{dy}{dz})$ for each slit position y.

Creating a phase space plot

The whole data array derived from the BPM signal is plotted using the built in function "ListContourPlot" of Mathematica®. Since the distribution $I(\frac{dy}{dz})$ was only measured at a few discrete slit positions, the values were interpolated in y to get a better approximation of the actual phase space. For a better comparison of the results, the distributions were normalized by using the maximum value.

3.1.3. Measurement results

The most relevant phase space plots of SETUP1 are given in Figure 3.5. To achieve an ion energy of 30 keV for singly charged anions, the source voltages were set to 3 kV for the cathode, 8.5 kV for the extraction and 18.5 kV for pre-acceleration stage. The focal lens voltage was either set to 1 kV (Figure 3.5 a & b) or to 0 kV (Figure 3.5 c & d) relative to extraction potential.

Without the focal lens (0 kV) the beam maximum lies between -1 mm and +2 mm in the x-direction and between -2.5 mm and -0.5 mm on the y-axis (Figure 3.5a,b).

Assuming no forces acting on the particles of the ion beam, their individual momenta stay constant and their slope can be used to evolve the particle's path in z direction. For example, the y position of a single beam particle i can be calculated as

$$y_i(z) = y_i(z_{y-axis}) + (z - z_{y-axis}) \cdot (\frac{dy}{dz})_i \tag{3.4}$$

with z_{y-axis} being the z-positions of the measurement plane. The x-positions can be calculated analogously.

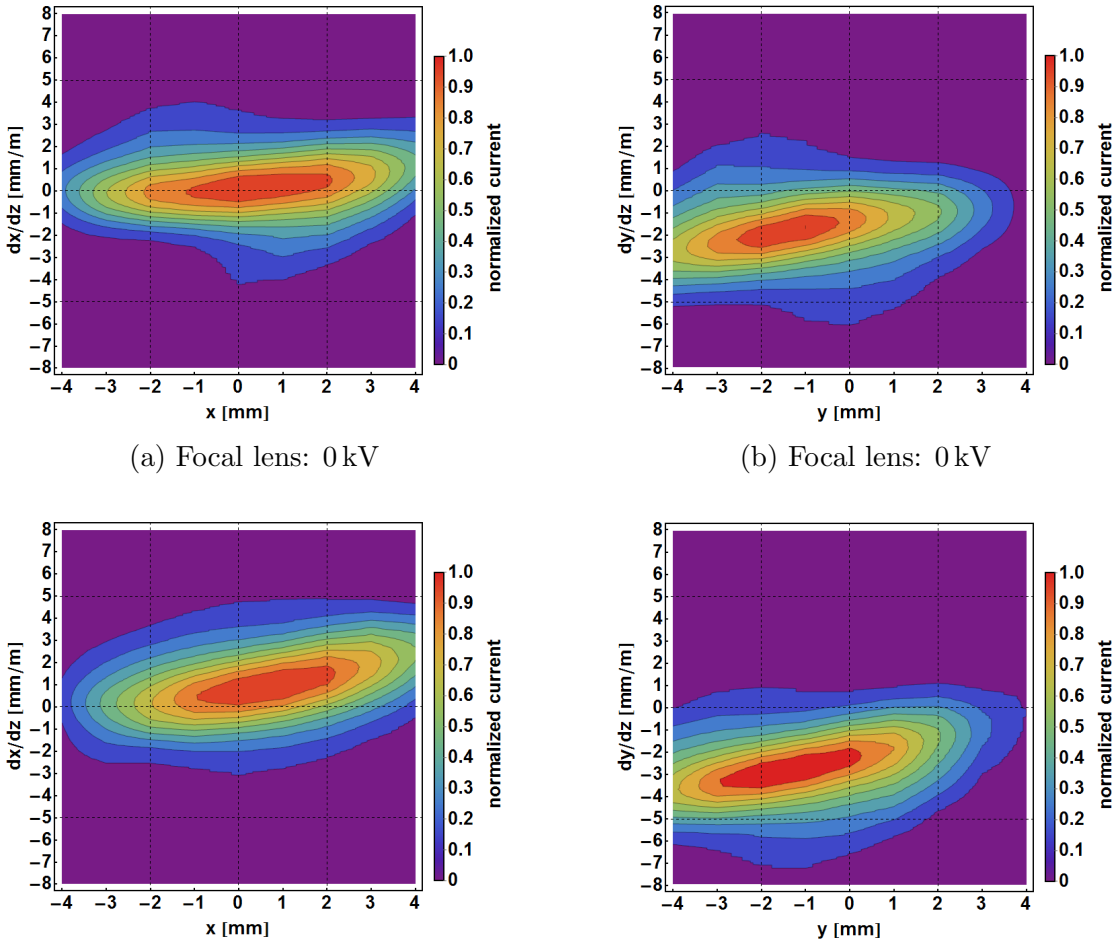

(a) Focal lens: 0 kV

(b) Focal lens: 0 kV

(c) Focal lens: 1 kV

(d) Focal lens: 1 kV

Figure 3.5.: The most relevant phase space results after the ion source (SETUP1). The distance between the measurement plane and the source exit (flange of the pre-acceleration stage) amounts to 210 mm and 240 mm for x and y measurements, respectively. All measurements were done using the source settings: cathode voltage=3 kV, extraction voltage=8.5 kV, pre-acceleration=18.5 kV. The graphics (a) & (b) show the phase space without the use of the source's focal lens and the diagrams (c) & (d) show the result of a measurements with a focal lens voltage of 1 kV relative to the extraction potential.

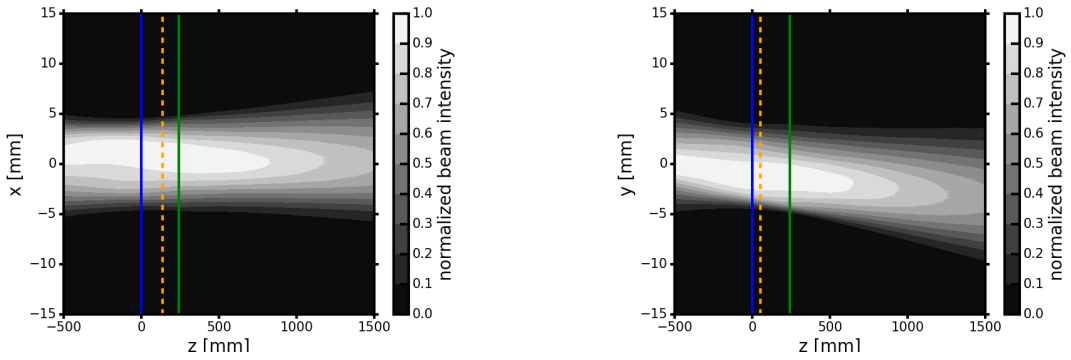

(a) x direction (b) y direction

Figure 3.6.: Evolution of the beam profile in x- and y-direction are presented in (a) and (b), respectively. The exit of the source (blue) is defined as $z = 0$ and the measurement planes of the phase space distribution (green) were located at z_{x-axis} =210 mm and z_{y-axis} =240 mm. The beam profile was calculated at equidistant z positions (Δz =1 mm). Both beam waists (orange dashed) lie between the slit and the exit of the source.

In the contour plot of the phase space distribution the evolution can be seen as a sheering, where each pixel is shifted in x- and y-direction proportional to their respective slope. This way the measured phase space distribution can be calculated at each z-position resulting in the intensity distributions $I(z, x, \frac{dx}{dz})$ and $I(z, y, \frac{dy}{dz})$. By integrating these distributions over the slope the evolution of the beam profile in z-direction ($I(z, y)$ and $I(z, x)$) is gained (Figure 3.6).

The evolution of the beam profile was used to determine the 1σ beam waists. The beam waist for the x-axis was found at z =138 mm distance from the source exit with a diameter of d_x =5.0 mm. The beam waist for the y-axis was found at z =52 mm distance from the source exit and has a diameter of d_y =4.6 mm.

The use of the focal lens at 1 kV shows no significant change in beam position, but the slope distribution in both directions deviate further away from a beam parallel to the intended path. Therefore, the focal lens of the source was usually set to 0 kV during later measurements.

Since the ILIAMS system was under construction while the phase space measurements were done on SETUP2, a beam injected into the cooler could not be analyzed. Instead of measuring the phase space of an injected beam the effect of a 2D-steerer [Moreau, 2016] on the beam's phase space distribution was investigated and will be discussed here.

The currents through the coils of the bending magnet (BM I1-1) were set to center the ion beam at the BPM position. It should be noted here that the focal plane of the double focusing bending magnet is designed to coincide with the entrance aperture of the RFQ cooler. Therefore, all SETUP2 measurements were done closer to the magnet than its focal plane. The source setup resembles the settings during SETUP1 without the use of the focal lens.

The plots in Figure 3.7 show the phase space distributions in x-direction for different settings of the 2D-steerer. As expected, sheering of the phase space distribution indicates a beam waist further away from the magnet (Figure 3.7a). By applying -250 V to the steerer's x-component, the negative ions feel a force in negative x-direction during the passage. Therefore, the beam is bent into the negative x-direction towards an inner path through the magnet and the resulting phase space is shifted in both the position and the propagation angle (Figure 3.7b). The shift towards more positive slopes, in contrast to the initial bending in the negative direction, is an effect of the double focusing magnet between steerer and measurement plane. Adding a deflection in y-direction, by setting the y-component to -500 V, the maximum of the x-phase space changes neither in position nor in slope, but looks stretched (Figure 3.7c). This indicates a lens effect of the steerer, caused by the potential raise of the x-electrodes due to the internal voltage divider of the steerer. By turning off only the x-component of the steerer, one would expect to see a slightly deformed version of the unaffected phase space (i.e.Figure 3.7a). Instead, the maximum is still shifted, requiring a bending of the beam (Figure 3.7d). Since no potential difference between positive and negative x-electrode should be present, the only explanation would be a lens effect caused by the y-component in combination with an off-centered steerer position.

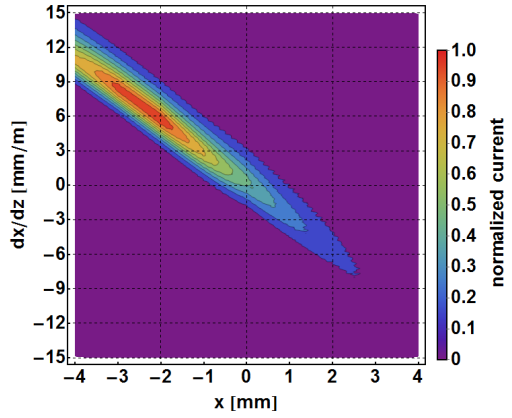

(a) X-Steerer: 0 V , Y-Steerer: 0 V

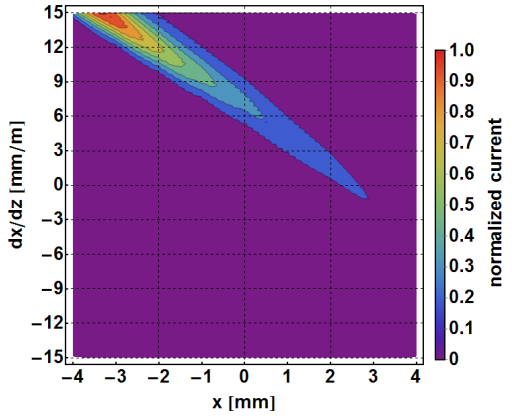

(b) X-Steerer: -250 V , Y-Steerer: 0 V

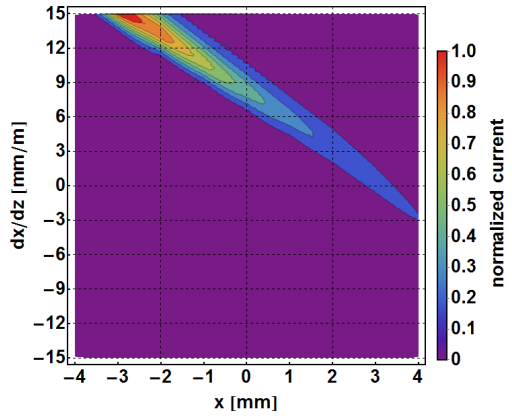

(c) X-Steerer: -250 V , Y-Steerer: -500 V

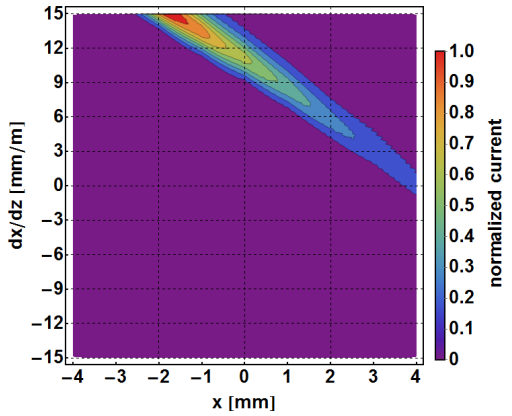

(d) X-Steerer: 0 V , Y-Steerer: -500 V

Figure 3.7.: The x-phase space results after the injection magnet to the ion cooler (SETUP2) for different 2D steerer settings. The x- and y-measurement planes lie 750 mm and 760 mm away from the tangent crossing point of the magnet. They are closer to the magnet than its designed focal plane. All measurements were done using the source settings: cathode voltage= 3 kV , extraction voltage=8.5 kV, pre-acceleration=18.5 kV. The steering effect of the y-component in (d) indicates an off centered positioning.

These measurements make it clear that changing one parameter of the steerer also affects the phase space in perpendicular direction. Due to this behavior it is advised to include both parameters during a tuning process of the 2D steerer. Measurements on the y-phase space distribution are presented in Appendix B, but the results indicate a potential systematic error during the measurement.

New measurements and simulations regarding the ILIAMS phase space have been done by Wasserburger [2018] in order to improve the cooler injection. However, the measured phase spaces of the source output are not comparable, because the carbon measurement by Wasserburger [2018] were performed at usual carbon settings of Source 1 (anion energy of 70 keV and focal lens at 1.51 kV).

3.2. Ion Laser InterAction Mass Spectrometry (ILIAMS)

A closeup of the schematic drawing of the Ion Laser InterAction Mass Spectrometry (ILIAMS) setup is given in Figure 3.8. The ILIAMS system is located in an extension to the VERA building and is connected to the low energy beamline of the AMS system (cf. Figure 2.3). The connecting beamline contains steerers and electrostatic einzel-lenses to optimize the beam transmission. Two Faraday cups and a beam profile monitor are also installed to perform beam diagnosis.

The ion source of ILIAMS is a MC-SNICS by NEC, which uses a cathode wheel containing up to 40 individual cathodes. Typically caesium is used for sputtering, but during some of the chlorine measurements the element rubidium was used due to investigations on the isotope ^{135}Cs using the same ion source. In general, the kinetic energy of the ions emitted from the source is 30 keV. To achieve this energy the source parameters are usually set to 3 kV for the cathode voltage, 8.5 kV for the extraction voltage and 18.5 kV set as pre-acceleration voltage. At this energy the double focusing 90° bending Magnet (Danfysik, r=350 mm , B_{max}=1.23 T) is capable of bending singly charged negative ions with a mass of up to 280 amu.

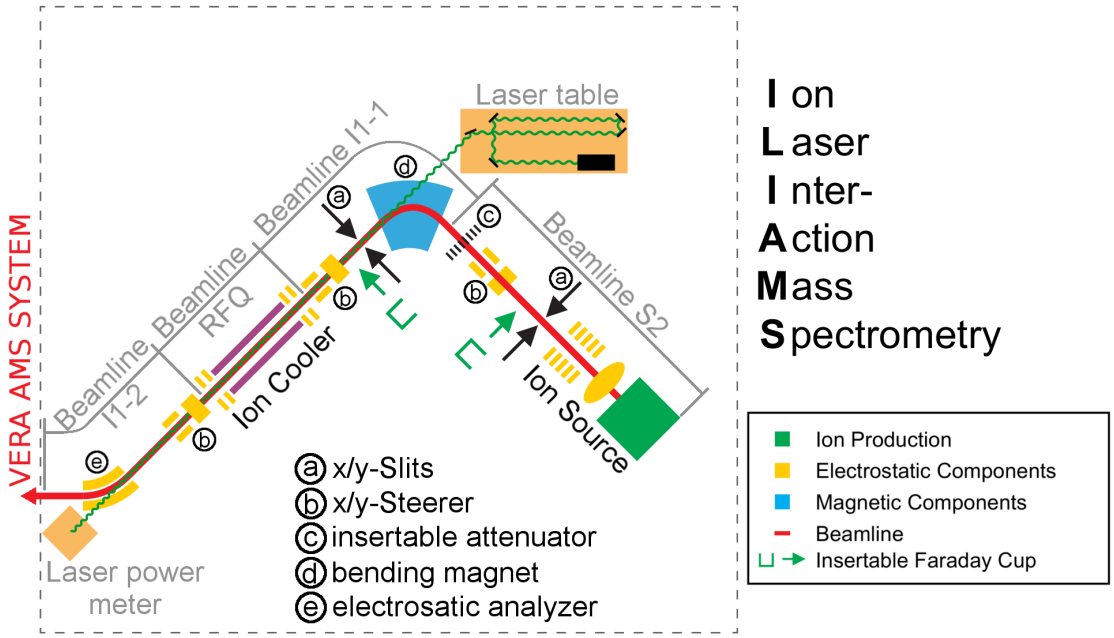

Figure 3.8.: Schematic drawing of the ILIAMS system.

The ion cooler was built during the ILIAS project and a detailed description of it can be found in the works of Forstner et al. [2015], Pitters [2015], Moreau [2016] and Martschini et al. [2017]. The last filter element in the ILIAMS setup is a 45° electrostatic analyzer capable of bending singly charged anion beams with energies up to 60 keV. Two insertable Faraday cups and x/y-slit pairs are mounted in the beamline segments I1-1 and S2 to perform beam position diagnosis before the cooler injection. A total of three 2D-steerers are mounted in the ILIAMS system to assure optimal injection and extraction of the ions loaded into the cooler. A detailed description of the steerer design can be found in Moreau [2016]. Between ion source and bending magnet an attenuator can be inserted into the system. Its purpose is to decrease the usually intense ion beam during stable isotope measurement. This way the transmission through the cooler is similar for both the abundant and the rare isotope. The material used for the attenuating device is a Conidur® hole sheet, which has an initial measured attenuation factor of 70.

A drawing of the laser table setup is shown in Figure 3.9. A more detailed graphic, containing the positions of the various optical elements on the table, is given in

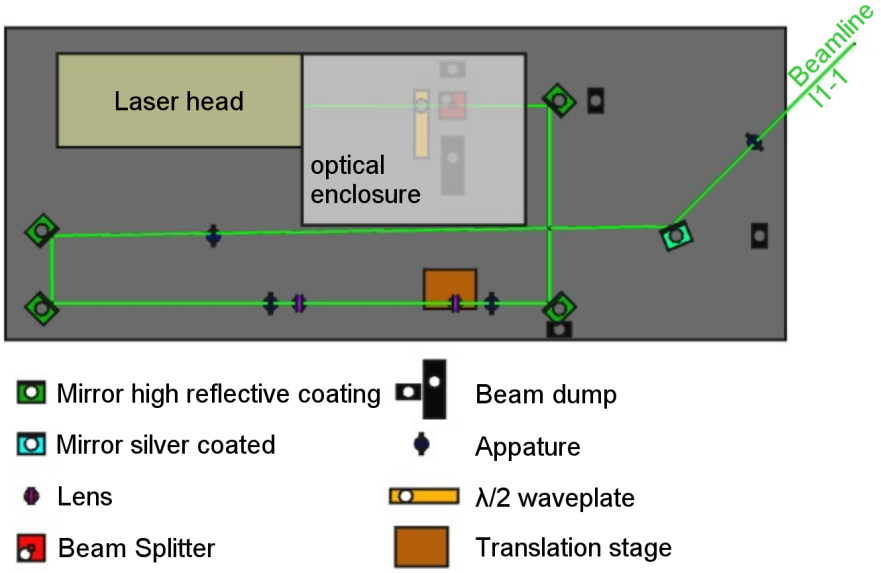

Figure 3.9.: Schematic drawing of the laser setup made with [FreeCAD, 2018]

Appendix C. The laser table is constructed out of a 150x60 cm^2 breadboard from THORLABS® and a carrier construction, which is made out of aluminum profiles. The laser source, Verdi V18 from Coherent®, is a diode-pumped solid-state type. It is capable of emitting a continuous wave (CW) with a maximum power of 18 W at a wavelength of 532 nm. The laser head is located on the laser table, connected to its power supply, which is standing beneath the table. An additional water cooling system is used to prevent overheating.

The emitted laser power is usually set to 18 W and the actual laser power injected into the ILIAMS system is adjusted by using a combination of a $\lambda/2$-waveplate (reflectance <0.25 % per side [CVI™, 2018b]) and a high energy polarizing beam splitter (parallel transmission >95 % [CVI™, 2018a]). Both are mounted inside an optical enclosure and the reflected light is absorbed by a large beam dump. A motorized rotation mount allows precise tuning of the $\lambda/2$-waveplate angle via the APT™ software by THORLABS®.

The laser fraction transmitted by the beam splitter leaves the enclosure and is adjusted to beamline height via two high-reflective mirrors (T >99.8 % [Laseroptik, 2018]). The adjusted beam passes two plano-convex UVFS lenses with 100 mm and 200 mm focal length in this order (UCFS transmission 94 % for 10 mm thickness [Thorlabs®, 2018b]). The lens system works as a Kepler-telescope. The lens with 100 mm is located on a translation stage facilitating adjustment of the distance between them. The other mirrors reflecting the laser beam are used for optimization of the overlap between ion and laser beam inside the RFQ cooler. It should be noted that only the last reflection is done using a silver coated mirror (reflectance $\geq$ 94.9 % for an angle of incidence of 45° [Thorlabs®, 2018a]), because it has a higher transmission at an incidence angle of 67.5° compared to the other mirrors used in the setup. In addition to the enclosure of the output regulation system (beam splitter and waveplate), the whole table is covered by an black hard cover enclosure from THORLABS®. The connection between the beamline entrance and the table cover is done using a pipe and black masking tape.

The laser beam enters the beamline through a MgF_2 window, which is mounted to the beam pipe inside the yoke of the bending magnet. The laser beam passes the ILIAMS beamline and exits through another MgF_2 window mounted to the straight-on port of the ESA housing. Both windows are from VACOM® with a reported transmission of about 93 % at a wavelength of 532 nm [VACOM®, 2018]. The transmitted laser power is measured by using a the thermal power sensor S314C from THORLABS® and the appropriate power meter console.

By combining all transmission values of the individual elements the total transmission, from laser head output to the sensor of the power meter, is about 67.5 %. Measurements and tuning showed, that during the selection of 18 W on the power supply only 16.6 W could be measured at the exit of the laser head. The optical elements mounted at the laser table transmit about 83.7 % of the intensity. During the passage of the cooler beamline and the MgF_2 windows, the laser intensity decreases by about 23,7 %. These high loss results in an experimental total transmission of about 63.8 %.

4. Sulfur suppression using laser photodetatchment

Previous investigations by Pitters [2015] and Moreau [2016] on the ILIAS setup verified the photodetachment process for Cu^- and MgO^-. A $^{63}Cu^-$ ion beam could be suppressed by over five orders of magnitude during laser beam overlap. A MgO^- beam showed photodetachment suppression by four orders of magnitude. Further measurements by Kalb [2017] using the ILIAMS system resulted in suppression of ^{26}Mg during ^{26}Al measurements by a total factor of 10^{13}, where a factor of 10^5 to 10^6 comes from collisions with the buffer gas. The photodetachment suppression of sulfur was not investigated in the ILIAS project, but the detachment had already been observed by Berkovits et al. [1989]. This chapter presents the first laser photodetachment suppression measurements of the element sulfur using the ILIAMS system.

4.1. Material used for suppression measurements

In order to measure the suppression of sulfur by laser photodetachment a sulfur spiked AgCl material was used. The chemical preparation was done following a procedure which was previously used at VERA in 2010. Table 4.1 lists materials and required concentrations used for the production of the spike. The chemical component Na_2S was mixed by combining 500mg of (Na_2S +$9H_2O$) with additional 10 ml of H_2O. The rest of the substances were available in the chemical lab.

In total 4 different sulfur spiked materials were created. The first attempt (batch #1) resulted in a solution with a pH value of 4 and showed no clear separation between solid AgCl+Ag_2S and liquid components. Due to this it was doubted

Material	required concentration
NaCl	$125\,g/l$
Na_2S	$35\,g/l$
HNO_3	$0.14\,Mol$
$AgNO_3$	$350\,g/l$

Table 4.1.: Chemical materials for sulfur spiked AgCl targets

that the estimated Cl:S ratio was reached. Therefore, it was not used for sulfur suppression experiments, but the high sulfur content still makes it a very good tuning material. In a second attempt a total of three materials (#2*a*, #2*b* and #2*c*) were mixed. All of these new batches used 400 μl NaCl, 165 μl Na_2S and 500 μl $AgNO_3$. The used volume of HNO_3 was 400 μl for batch #2*a* and 300 μl for the batches #2*b* and #2*c*. The preparation was done by mixing NaCl with Na_2S and then adding 5 ml of Milli-Q™ water. By combining the result with the specified amount of HNO_3, a solution with pH value of 6.5 was achieved. In the last step $AgNO_3$ was added and this time clear separation between solid and liquid component was accomplished. Afterwards the batches were put into a centrifuge and the supernatant liquid part was discarded before the precipitants were dried for 14 h in the oven. The heat in the oven reduced the rest humidity and the resulting powder could be pressed into the cathodes in the usual manner.

By following this procedure the expected particle ratio S:Cl is about 1:11.6 in the form of an AgCl+Ag_2S material.

4.2. Sulfur suppression using ^{36}S

The measurement of the suppression factor consisted out of multiple single runs at different laser powers. During a single run the events in the detector are logged over a specified time interval. A typical ^{36}Cl measurement setup was used, which is given in Appendix E. The events were detected using the Multi Anode Ionization Chamber (MAIC) of the VERA system [Buchriegler, 2013]. The charge state 2+ was selected at the high energy side, because it shows high accelerator transmission. The material sputtered during this experiment was the self-made

AgCl+Ag_2S spike (batch #2*a*). During the measurement, the $^{36}Cl^{2+}$ current on the high energy side was measured multiple times and stayed around 100 nA during the whole investigation.

The suppression of ^{36}S was calculated in two different ways: a "total suppression" and a "photodetachment suppression". In contrast to the pure suppression by the interaction with the laser ("photodetachment suppression"), the "total suppression" also includes suppression due to transmission and yield differences between chlorine and sulfur.

The "total suppression factor" value was obtained using the measured $^{36}S/^{37}Cl^{2+}$ rate at a given transmitted laser power and the nominal $^{36}S/^{37}Cl$ ratio of the mixed AgCl+Ag_2S material.

$$total\ suppression\ factor = \frac{(^{36}S/^{37}Cl)_{mixed}}{(^{36}S^{2+}/^{37}Cl^{2+})_{measured}} \tag{4.1}$$

The nominal $^{36}S/^{37}Cl$ ratio of the mixed material was calculated by applying the mole fraction abundance of ^{37}Cl, the theoretical ratio of the material (S:Cl≈1:11.6) and the mole fraction abundance of ^{36}S (0.01(1) % [De Laeter et al., 2003]). This approach does not include the difference in ionization and stripping yield. Therefore, it can only be used to estimate the overall suppression of ^{36}S.

In this context it should be mentioned that the source's sulfur output decreases over time relative to chlorine output (Figure 4.1). This additional drift was not corrected during data evaluation.

The "photodetachment suppression factor" was calculated entirely by measured values of $^{36}S^{2+}/^{37}Cl^{2+}$ for different laser powers. The count rate of a non-suppressed $^{36}S^{2+}$ beam was taken as a reference.

$$photodetachment\ suppression\ factor = \frac{(^{36}S^{2+}/^{37}Cl^{2+})_{without\ laser}}{(^{36}S^{2+}/^{37}Cl^{2+})_{with\ laser}} \tag{4.2}$$

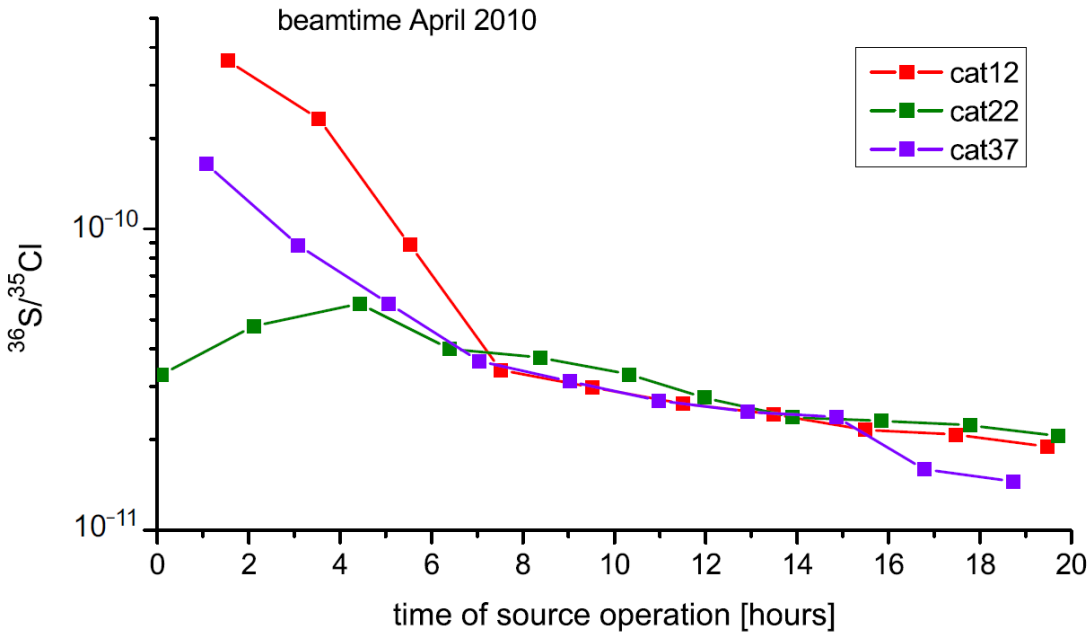

Figure 4.1.: Ratio between ^{35}Cl and ^{36}S output as a function of the source's operation time. This graphic is taken from Martschini [2012].

The measured data of suppression factors are presented in Figure 4.2. During the measurement of a photodetachment suppression factor the determination of the non-suppressed count rate of ^{36}S turned out to be problematic. The intensity was too low to measure a current in a Faraday cup and too high for the ionization chamber. The detector raw data showed high amounts of pile up for low laser power measurements. This may indicate that not all events are recognized by the detector, due to its dead time. These unrecognized events would underestimate the $(^{36}S^{2+}/^{37}Cl^{2+})_{without\,laser}$ ratio. Hence, the presented photodetachment suppression factors should be seen as lower bounds.

The calculation of the total suppression factor does not correct the lower cooler transmission of the high intensity ^{37}Cl beam. This results also in an underestimation of the non-suppressed $^{36}S^{2+}$ events. Therefore this suppression factor can also be seen as a lower bound, but the error without the correction of the cooler transmission is less then one order of magnitude.

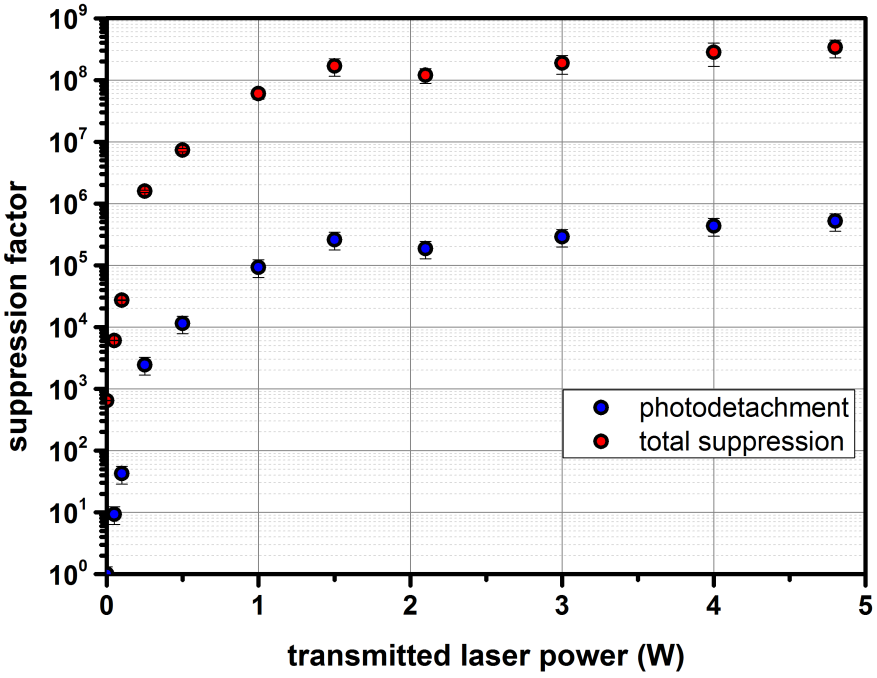

Figure 4.2.: The ^{36}S suppression factor as a function of the transmitted power of a 532 nm laser. The "total suppression" data points were calculated using the nominal ratio. The "photodetachment" data points were calculated by using only measured ^{36}S count rates acquired with the MAIC detector.

4.3. Sulfur suppression using ^{34}S

The low count rate of the remaining non-suppressed ^{36}S (laser on) was very low and required long measurement times. In addition, the non-suppressed beam (laser off) could not be effectively measured using neither the detector nor the Faraday cup. An alternative approach to determine the suppression factor of sulfur was to measure a more abundant stable isotope of the element.

The two most abundant stable sulfur isotopes are ^{34}S, with a mole fraction abundance of (4.25±0.24) % [NNDC, 2018] and ^{32}S, with a mole fraction abundance of (94.99±0.26) % [NNDC, 2018]. When choosing the isotope it is always advised to

look at the expected interference that could pass the AMS system during the measurement. In the case of ^{32}S the highest interference is expected from ^{16}O. It can pass the low energy side as an $^{16}O_2^-$ molecule and, if dissociated in the stripping process, the individual atoms can pass the high energy filters in +1 charge state. A non-dissociated $^{16}O_2$ molecule can also pass the filters in charge state +2. The major interference of ^{34}S is also expected to be oxygen. The low energy side can be passed by a molecule with m=34 amu, which can be achieved by combinations of ^{16}O, ^{17}O and ^{1}H (e.g. $^{16}O^{17}O^{1}H$). The high energy side can be passed either by the non-dissociated molecule in charge state +2, or more probable by fragments with mass 17 amu and charge state +1.

The mole fraction abundances of the two oxygen isotopes are (99.757±0.016) % for ^{16}O and (0.038±0.001) % for ^{17}O [NNDC, 2018]. According to the mole fraction abundances the interference ratio $^{17}O/^{34}S$ is expected to be lower than the interference ratio $^{16}O/^{32}S$. Although the low energy side during ^{34}S measurements can be passed by more than one type of molecule, the formation of $^{17}O_2$ or $^{17}O^{16}OH^-$ is far less probable than the formation of $^{16}O_2$ because it requires one or even two of the less abundant ^{17}O isotope. Therefore, the isotope ^{34}S was chosen for the suppression experiments.

For the measurement the accelerator system was scaled to mass 34 amu from an initial mass 36 amu setup used for ^{36}Cl measurements. The materials used during this experiment were from the batches #2*a*, #2*b* and #2*c*. The Faraday cup FC L4-1, located between the high energy ESA and the MAIC detector, was used to measure the ^{34}S current at laser power 0 W. The MAIC detector was chosen to determine the ^{34}S counts for different laser powers in the same way as for the ^{36}S investigations.

In order to calculate the correct suppression factor for ^{34}S, the contribution of the interference was investigated. The 2D spectrum of the MAIC detector revealed good discrimination between ^{34}S and the expected interferences (Figure 4.3).

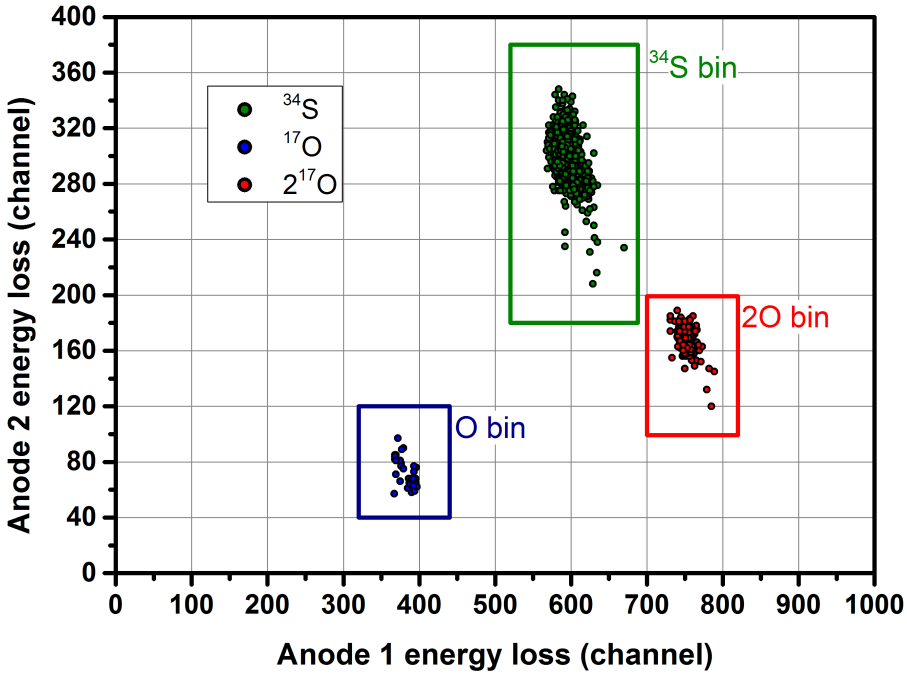

Figure 4.3.: Example of a 2D spectrum measured with the MAIC detector during the ^{34}S investigations. The bins were used to distinguish and count the events of the individual particle types.

During the ion current measurement the different types of particles are indistinguishable, because each incident ion contributes to the total current measured by the Faraday cup. The interfering molecules O_2 (EA=(0.450± 0.002) eV, [Rumble, 2018]) and HO_2 (EA=(1.078± 0.006) eV, [Rumble, 2018]) can both be suppressed by the interaction with the green laser ($E_\gamma \approx 2.33eV$) at the low energy side. This indicates a higher amount of interfering ions during the ion current measurements, where the laser was turned off. To measure the effect of the laser power on possible individual ion intensity, multiple detector spectra were recorded to estimate a trend of the individual count rates (Figure 4.4). The presented data was not acquired during the actual suppression measurement, because the good alignment during the investigation resulted in very few oxygen events in the detector. These few counts could not indicate a tendency of the ratio between sulfur and the oxygen

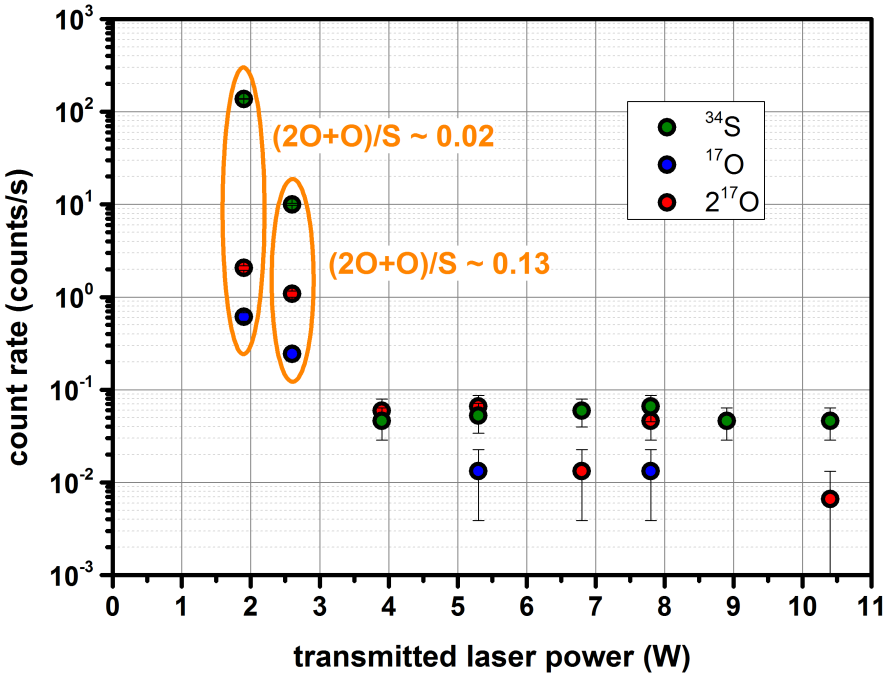

Figure 4.4.: Individual count rates from a Ag_2S+AgCl (1:11.6) target as a function of the transmitted laser power for an injected beam with mass of 34 amu. While higher laser power resulted in almost identical count rates, the sulfur count rate increases faster at lower laser powers than the interference.

interference. Therefore, the presented count rates were measured during machine settings, where the laser transmission was lower (maximal transmitted laser power 10 W instead of 11 W).

The contribution of the ^{17}O interference to the overall count rate at 2.6 W transmitted laser power is about 13 % and decreases to 2 % at a laser power of 1.9 W. The data indicates even less relative contribution at lower laser powers. The ion current measurements show scatter of about 2 % in the sub 1 nA region. Because of this, they were taken as pure ^{34}S with an uncertainty of 2 %.

For the actual determination of the photodetachment suppression factor the laser beam was aligned in the best way possible. In total four cathodes with spiked material from 3 different batches were used. The non-suppressed ^{34}S current was measured at least at the beginning and at the end of each cathode investigation. Linear interpolation of the ion current data was done, to calculate its value during the event counting in the detector. After each cathode change the injection and extraction of the cooler was scanned to ensure similar cooler behavior. The scans involved the high energy lens voltage at the cooler's entrance (RFQ InjHV), the high energy lens voltage at the exit of the cooler (RFQ ExtHV) and the three 2D-steerers in the beam line sections S2, I1-1 and I1-2. The suppression factor, determined with the interpolated current and the ^{34}S detector counts, is plotted versus the transmitted laser power in Figure 4.5. The uncertainties were obtained by Gaussian error propagation of the detector event counting statistics and the estimated current uncertainty of 2 %.

The measured data reveals higher suppression values than the prior ^{36}S investigation (cf. Figure 4.2). The problematic determination of the of the non-suppressed ^{36}S count rate might be the reason for the underestimation of the ^{36}S suppression measurement. The new measurement showed that above 4 W the individual values fluctuate between 10^{10} and 10^{11}, not indicating any further tendency. Below the 4 W mark, the measured suppression factors show decreasing tendency. At around 1.2 W the suppression reached values of about 10^{7}. The data points of the long sputtered cathode show the similar behavior but the values show higher scatter.

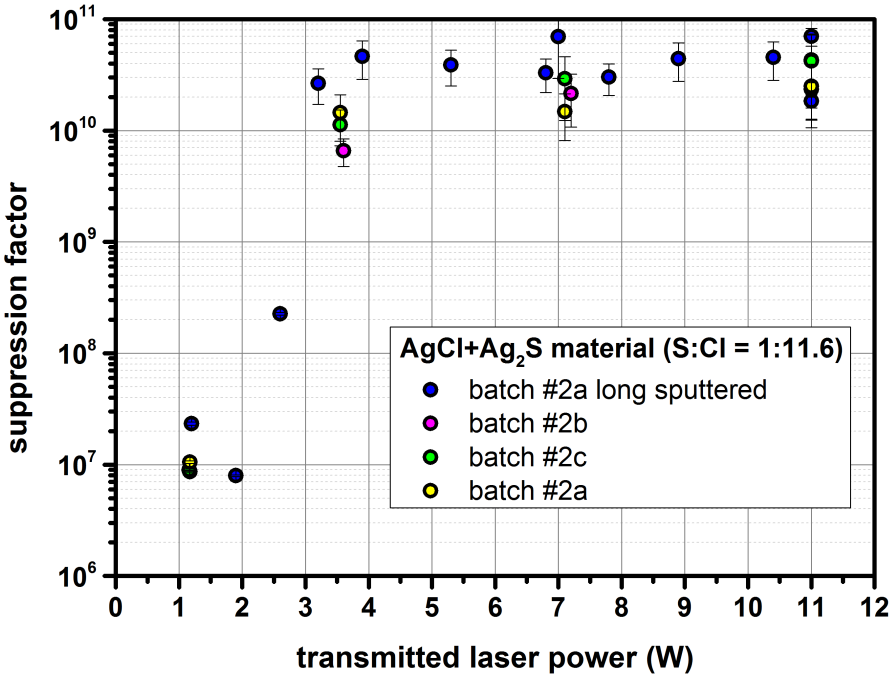

Figure 4.5.: The suppression factor of ^{34}S as a function of the transmitted power of a 532 nm laser. The cathode with the tag "long sputtered" was already used during the ^{36}S investigation.

5. Molecular isobaric background

The laser photodetachment approach has proven effective for sulfur suppression (Chapter 4), which is one of the main goals of this new technique. The next investigation regarding ^{36}Cl measurements was the analysis of potential molecular interferences. Assuming that all ions extracted from the source have charge state -1, the interfering molecule must have mass 36 amu in order to pass the low energy filters of the instrument.

5.1. Chlorine hydrides

Usually hydrides of the stable isotopes are potential intense molecular interferences. Therefore, the molecule H^{35}Cl is expected to contribute to the mass 36 amu beam. Experiments done by Christophorou et al. [1968] could not show the formation of the ion HCl^-, but rather the dissociation of the molecule. This dissociative attachment usually results in a negative chlorine ion and a neutral H atom.

$$e^- + HCl \rightarrow H + Cl^- \tag{5.1}$$

Also mass scans during various ^{36}Cl tunings on the ILIAMS system did not reveal any HCl anions.

5.2. Carbon

Another potential interference is the molecule $^{12}C_3^-$. The formation of carbon trimeric anions in the ion source is known, due to the fact that it is a typical AMS isotope and is also measured at the VERA facility. For investigations regarding the carbon interference, an already sputtered carbon cathode was used as a target.

A machine setup used for ^{36}Cl measurements was taken as a starting point. During tuning of the carbon beam through the RFQ ion cooler the cooler potential and the guide electrode potential were scanned (Figure 5.1a). The behavior suggests the contribution of more than one ion species. The EA of C_3 is 1.981±0.020 eV [Rumble, 2018], which allows the use of the photodetachment method with the presented ILIAMS setup. The same scan was done for an laser power of 12 W (Figure 5.1b). The scan showed that a part of the ion beam is neutralized, while a minor contribution is unaffected by the overlapped laser beam. The absence of the ion current at 30 kV RFQ potential and a current maximum at 29.925 kV indicate that the unaffected ion species is only measured at injection energies in the order of 10-100 eV. The molecule C_2 (EA(C_2)=3.296±0.006 eV [Rumble, 2018]) can not be detached by the 532 nm laser (E_γ =2.33 eV). This fact suggests, that the unaffected species is $^{12}C_2^-$. The formation is expected to result out of collisions between an injected $^{12}C_3^-$ molecule and the He buffer gas inside the RFQ cooler.

$$^{12}C_3^- + He \rightarrow ^{12}C_2^- + ^{12}C + He \tag{5.2}$$

A new tuning on the setup used for the scans in Figure 5.1a & b was done and resulted in a setup with a different current behavior (Figure 5.1c). The distribution still suggests two contributions and prefers even higher injection energies. The main differences between the measurement setups were the voltages applied to the injection and extraction electrodes of the cooler.

To further analyze the composition of the ion beam, the low energy bending magnet BM 01-1 was used to separate the different masses (Figure 5.2). The mass scans were done for different ion cooler settings of interest, chosen on the basis of the data provided in Figure 5.1. At a guide electrode voltage of 20 V and RFQ cooler potential of 29.95 kV, ion beams with the masses 24 amu and 36 amu were detected to emerge from the cooler (see green colored line in Figure 5.2), identifying the molecules $^{12}C_2^-$ and $^{12}C_3^-$. The absence of a peak at 12 amu indicates that the applied cooler settings do not provide stable transmission conditions for this ion of significantly lower mass.

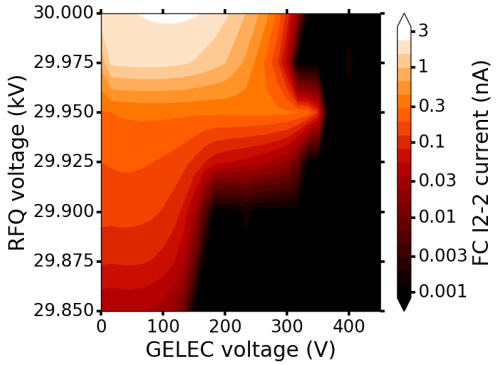

(a) Laser power: 0 W

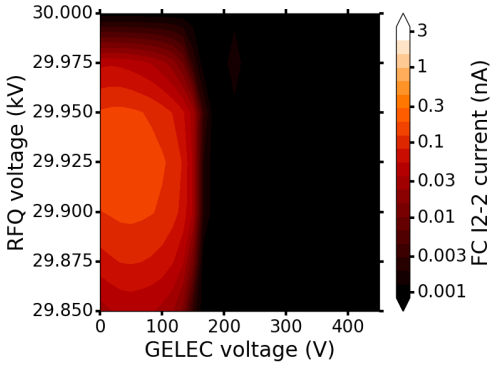

(b) Laser power: 12 W

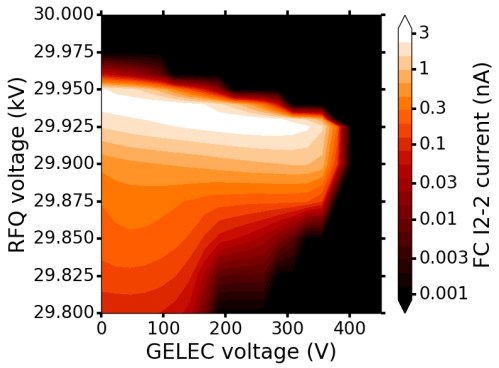

(c) Laser power: 0 W (different tuning)

Figure 5.1.: Two-dimensional scans of the ion current extracted from the ion cooler. The effect of the RFQ potential and the applied guide electrode (GELEC) voltage was investigated. The plots a & b show scans with and without laser overlap. The graphic c shows the current behavior for a different setup, where the assumed to be $^{12}C_3^-$ peak is shifted. Measured currents are plotted on a logarithmic scale to better represent the minor second peak.

By overlapping the ion beam with a green laser (12 W) the $^{12}C_3^-$ peak vanishes from the spectrum while the height of the $^{12}C_2^-$ peak is reduced only by a small fraction (see red colored line in Figure 5.2). The decrease of the $^{12}C_2^-$ intensity may be caused by photodetachment of $^{12}C_3^-$ prior to the collision with the helium buffer gas. As a result these collision produce neutral $^{12}C_2$ fragments, reducing

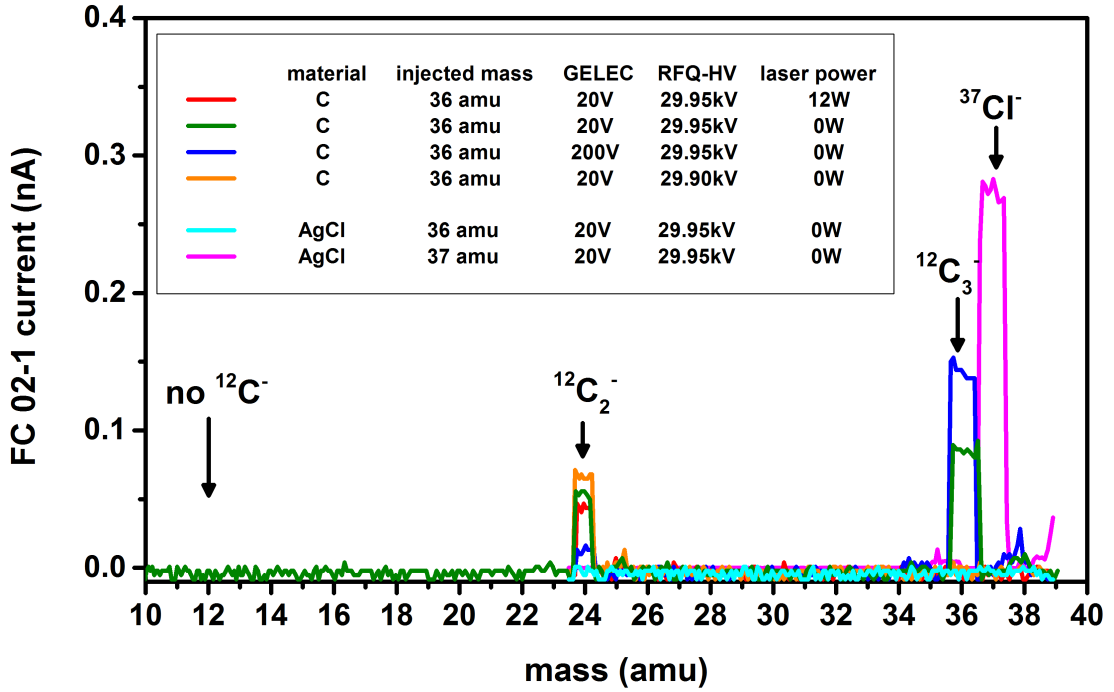

Figure 5.2.: Low energy mass scans of the cooler output to study potential molecular background contributions. The sputtering of a graphite target reveals peaks at the masses 24 amu and 36 amu, which show opposing trends for different cooler and laser settings (red, green, blue and orange colored lines). During AgCl sputtering neither the 24 amu peak, nor the mass 36 amu interference is measured (cyan and magenta colored lines)

the number of $^{12}C_2^-$. Cooler settings with higher guide electrode voltage (see blue colored line in Figure 5.2) and lower RFQ potential (see orange colored line in Figure 5.2) were also investigated. Higher guide electrode potential results in an increase of surviving $^{12}C_3^-$ and a decrease of $^{12}C_2^-$ intensity. This indicates a contribution to the deceleration of the injected ions or faster transport through the cooler, both of which decrease the chance of dissociative collisions with the buffer gas. The scan with lower cooler potential shows no $^{12}C_3^-$ and an increased $^{12}C_2^-$ current. In this case, the $^{12}C_3^-$ ions are assumed to collide with the buffer gas exclusively in an dissociative sense, increasing the amount of $^{12}C_2^-$ fragments.

An AgCl target was sputtered to estimate the molecular background on the low energy side during an actual chlorine measurement. During the injection of mass 36 no peak is visible when scanning the cooler output (see cyan colored line in Figure 5.2). This concludes low contamination of carbon. During mass 37 injection, the $^{37}Cl^-$ peak is significantly present, but the rest of the scan does not yield any additional information (see magenta colored line in Figure 5.2).

5.3. Further investigations

The absence of a signal at mass 36 amu during AgCl sputtering and the additional fact that the $^{12}C_3^-$ interference can be neutralized by overlapping the laser beam suggested further investigations of the background. The limited space between the low energy analyzing magnet and the accelerator does not allow the installation of a particle detector. Therefore, the investigations were conducted on the high energy side. A microchannel plate (MCP) detector, capable of counting ion events, was mounted behind the Faraday cup FC 03-1 (see Figure 5.3). The detector consists out of two microchannel plates in Chevron arrangement [Wiza et al., 1979] in front of an anode plate.

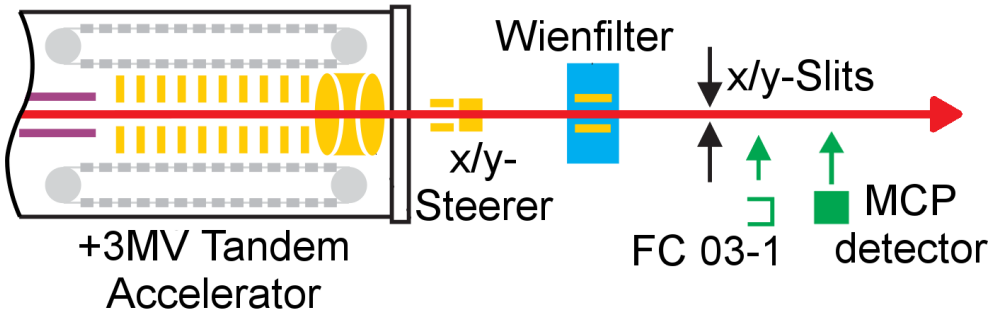

Figure 5.3.: Schematic drawing of the MCP detector position.

The advantage of the detection behind the accelerator is that the injected molecules undergo a stripping process, which may dissociate them into their fragments. The detector alone can not distinguish between the different fragments, but the Wien-filter allows the selection of a ratio between energy and mass $E/m \propto |\vec{E}|^2/|\vec{B}|^2$.

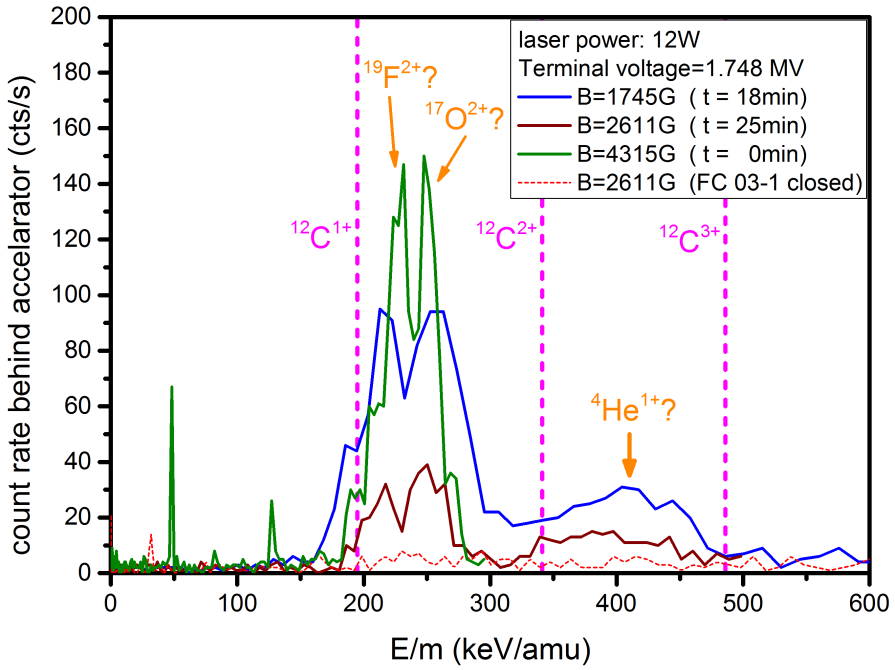

Figure 5.4.: Wienfilter scans of the accelerator output during AgCl sputtering and mass 36 amu injection with the laser in operation. The magnetic filed was set to a specified value, while the electrostatic potentials of the Wienfilter electrodes were scanned. The count rate was measured using the MCP detector. All peak positions differ from the expected carbon E/m values (indicated by pink dashed lines). The peak intensities decreased over time. A scan for closed Faraday cup FC 03-1 shows minor dark count rate of the detector.

The electric field $\vec{E}$ can be set faster than the magnetic field $\vec{B}$ of the dipole magnet. Therefore, the E/m value was scanned by stepwise increasing the electric field strength, while the magnetic field was set to a fixed value.

During the first investigations three different magnetic field strengths were selected. The potential difference between the electrostatic electrodes was scanned from 0 to about 52.8 kV in 0.4 kV steps (see Figure 5.4). The laser was operated at 12 W to detect non-suppressed molecules or their fragments. Both of the two

lower magnetic field scans (blue and red line in Figure 5.4) show two narrow peaks between 200 and 300 keV/amu. A broad peak of lower intensity between 300 and 500 keV/amu is also visible.

The expected E/m values of the ions $^{12}C^{1+}$, $^{12}C^{2+}$ and $^{12}C^{3+}$ do not match the position of the measured peaks. This verifies that the $^{12}C_3^-$ suppression is sufficient during the sputtering of AgCl targets. If carbon were the only molecular interference, this would allow measurements of $^{36}Cl^-$ on the low energy side. This is not the case, because the two narrow peaks reveal another molecular interference consisting out of two components. The other broader peak is assumed to correspond to single ionization of the stripper gas ($^4He^{1+}$) during collisions and would not be present at the low energy side. The large width of the peak is expected to result from a wide velocity distribution of the $^4He^{1+}$ ions, caused by kinetic transfer variations of the individual collisions and ionization at positions closer to the accelerator exit.

The intensity of the diatomic molecule decreases over sputtering time, which would correspond to a higher contamination at the material surface than in deeper layers. The peak positions suggest a molecule consisting out of ^{19}F and ^{17}O. Both fragments are detected in charge state 2+, with expected E/m=233.4 keV/amu 255.0 keV/amu, respectively. The molecule FO has an electron affinity of (2.272±0.006) eV [Rumble, 2018], which is about 60 meV lower then the photon energy of the 532 nm laser. The fact that the electron affinity is lower implies the detachment possibility, but the small energy difference suggests a small cross section. To further investigate the suppression of the molecule, the peaks were scanned at different laser powers (see Figure 5.5). The results verify the suppression of the molecular interference and reinforce the hypothesis of FO^- molecules. The additional use of the high energy filters and the detection by a silicon surface barrier detector proved that the fragment peaks can be found at high energy settings for m/q=19/2 and m/q=17/2 respectively. This matches the fragments of a $^{19}F^{17}O^-$ molecule.

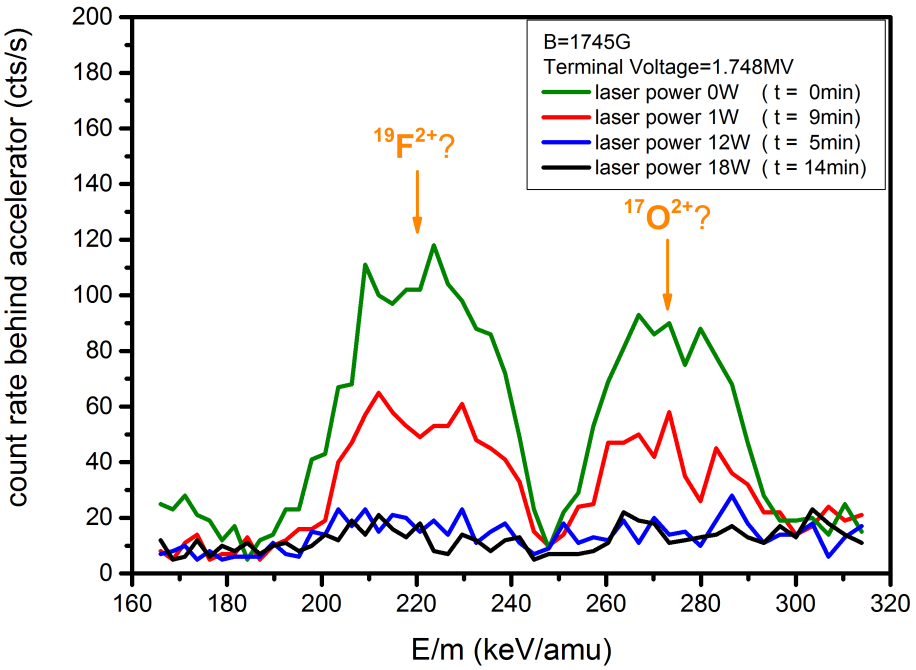

Figure 5.5.: Scans of the FO^- fragment peaks for different laser powers. The intensities show a higher suppression of the molecule fragments for increasing photon flux, which proves the occurence of a photodetachment process. The count rates during the two highest laser power settings (blue and black line) show no significant difference and are close to the dark count rate of the MCP detector.

The only known molecular interference prohibiting $^{36}Cl^-$ measurements on the low energy side of the system is therefore FO^-. The use of a laser with higher photon energy, but still lower than the electron affinity of Cl, may result in higher suppression of FO^-. This might allow ^{36}Cl measurements on the low energy side, without the use of the tandem accelerator.

6. Measurements of ^{36}Cl samples

This chapter gives an overview of ^{36}Cl measurements carried out with the ILIAMS setup. At first the new ^{36}Cl tuning and measurement procedure will be described. Afterwards the behaviors and limits, encountered during two sample measurements (January 2017 and August 2017) and a blank level investigation in October 2017, will be discussed. The evaluation of the measurement's raw data will not be described in this chapter, but can be found in the Appendix D.

6.1. Tuning procedure

First tuning of a chlorine beam through the ILIAMS system was done shortly after its completed installation at VERA. An usual Cl measurement involves the tuning of the rare ^{36}Cl isotope beam to a detector and the tuning of one or both stable isotopes to a Faraday cup of the high energy side. Since fast switching between isotopes is not possible when using the ILIAMS system (more information in Section 6.2), only the stable isotope ^{37}Cl was chosen as a reference. Assuming the natural ^{37}Cl/Cl abundance in the measured samples, the ^{36}Cl/Cl ratio can be calculated using the mole fraction abundances of the stable isotopes . The advantage of ^{37}Cl, in contrast to ^{35}Cl, is its lower mole fraction abundance (^{37}Cl:^{35}Cl $\approx$ 1:3). This already reduces the ion beam intensity, resulting in a higher cooler transmission (see Section 6.3.1). The stable ^{37}Cl isotope setup is also used as a pilot beam for the ^{36}Cl tuning.

During the creation of the first ^{37}Cl setup, the beam was step wise tuned from one Faraday cup to the next. In each step the parameters of the ion optical components between them where optimized. The absence of a Faraday cup close to the cooler exit makes the tuning through the cooler the most challenging and time

consuming part. Typically, the current of an attenuated $^{37}Cl^-$ beam is in the order of 10 nA. Its cooler transmission can be optimized to a value of around 80 %. This can be usually achieved by starting an *automax* script [Steier, 2000] containing the parameters of the cooler injection, cooler extraction, 2D-steerers and bending magnet. The cooler transmission can be optimized by using the Faraday cup FC I2-2. After further optimizations of the steerer and ESA parameters of the ILIAMS system, a tuned $^{37}Cl^-$ beam should be present at the connected and established part of the VERA system. The rest of the machine tuning is similar to the previous tuning procedure described by Martschini [2012].

The two major differences are that the ^{35}Cl isotope is not used and that the absence of the fast switching method requires a total of three setups (more information in Section 6.2). These setups differ from each other only by the settings for the cooler injected mass and Faraday cup sensitivity. Further tuning for chlorine measurements was done by using established setups as a starting point. A tuning script was already created and used, but still requires some attention of the operator. During the automatic tuning of the system, the use of a sulfur spiked material (see Chapter 4.1) is recommended, because the high amount of ^{36}S can be used to tune a mass 36 amu beam into the detector. The whole tuning procedure can be done in approximately one working day.

6.2. Measurement structure

The two ion sources at the VERA facility can each hold up to 40 different target cathodes in a cathode wheel. One cathode wheel usually contains multiple samples, standards and blanks. During the experimental work of this thesis standards from the DiluSe series [Martschini, 2012] were used. Various computer scripts were implemented, allowing automatic data acquisition during a measurement.

An ordinary measurement at VERA involves the acquisition of rare and stable isotope data for each cathode. Each data acquisition is referred to as "run" and is consecutively numbered during the measurement. During a measurement without the ILIAMS system, an electrostatic fast bouncing setup is used for switching

between stable and rare isotope injection into the accelerator. During the AMS measurement of a material, the same cathode is measured multiple times to achieve higher precision. To distinguish between these multiple measurements of the same cathode they are categorized in "turns". Therefore, a measurement consists of multiple turns, which usually contain a single run for each cathode in the wheel.

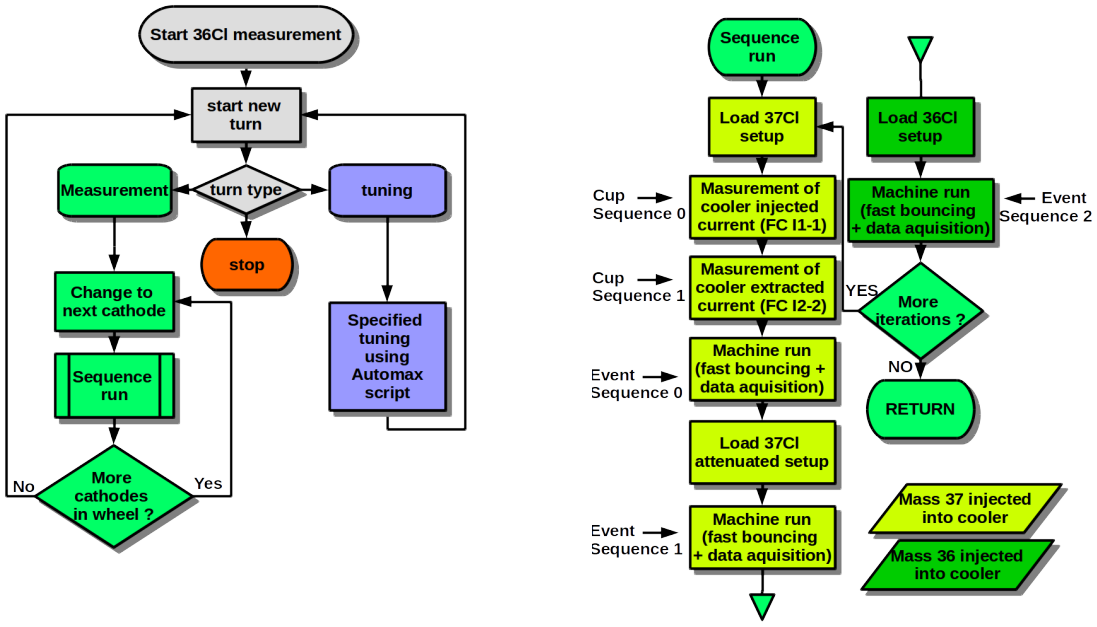

(a) Flowchart of a ^{36}Cl measurement procedure.

(b) Flowchart of a sequence run used in ^{36}Cl measurements.

Figure 6.1.: Measurement procedure illustrated in the form of a flowchart. A measurement procedure represented in (a) consists of multiple turns, which can be either used for cathode measurements, a tuning procedure, or to stop a measurement. The cathodes are measured during a sequence run described by the flowchart (b).

In contrast to other routine measurements at VERA, the bending magnet in the ILIAMS system injects only a selected p/q value into the cooler. The charge state extracted from the ion source for the Cl measurements is -1. Therefore the bending magnet and the ESA of the ILIAMS system already specify the masses of the ions in the low energy beamline. The absence of an electrostatic fast bouncing setup at the cooler injection prohibits the ILIAMS setup from fast switching between stable and rare isotope. The ILIAMS system also differs form other routine measurement structures due to the use of an attenuator in front of the injection magnet of ILIAMS. The attenuator can be inserted automatically and is used to reduce the stable isotope beam before it is injected into the cooler. To minimize the programming afford in implementing these new features, the ordinary runs were substituted by so called "sequence runs".

6.2.1. Sequence run

A sequence run was originally designed for automatic measurements of multiple actinide concentrations in one cathode. Due to this, it was already capable of changing the machine setup during the measurement of a single cathode. The individual isotope measurements are done during an so called sequence. There a two main types of sequences:

Cup-sequences

Cup-sequences can be used to determine Faraday cup currents at various beamline positions. In the case of chlorine measurements two different cup-sequences are implemented. The first is used to determine the ^{37}Cl current injected into the RFQ cooler (Faraday cup FC I1-1). A second cup-sequence measures the extracted ^{37}Cl current (Faraday cup FC I2-2). The combination allows to monitor the cooler transmission during the measurement.

Event-sequences

Event-sequences determine the data required to calculate the isotope ratio. Each event-sequence resembles a simple run procedure and uses the fast bouncing system of the accelerator injection. The sequence measures the rare isotope events in the detector and the low and high energy current of

the stable isotope. In a chlorine measurement there are three different event-sequences implemented, due to the mass selection of the cooler injection. Two of them load a setup for ^{37}Cl injection, which differ only in the use of the attenuator. The last event-sequence loads a setup for ^{36}Cl, to measure the rare isotope events.

These sequences can be arranged in a corresponding script. Also a number of iterations before the next cathode is measured, can be set. During the experimental work of this thesis the number of iterations was set to 3. Since switching between the isotopes ^{36}Cl and ^{37}Cl involves the loading of different setups, which takes several seconds, it is internally referred to as "slow bouncing method".

6.3. Measurement efficiency

The efficiency of an AMS measurement is an important quantity, because it is correlated to the required amount of material and measurement time. Previous ^{36}Cl measurements at VERA were performed with an overall detection efficiency of 8 % [Martschini, 2012], not including the negative ionization yield. A limiting factor was the selection of the high energy charge state 7+, which was necessary for the isobar separation in the recorded detector spectrum. In addition, the MAIC detection system used an aperture inside its sensitive volume between the second and third anode. This was build in to reduce straggling misinterpretation, but caused transmissional losses. The relatively narrow ^{36}Cl region of interest further reduced the detection efficiency.

In this chapter the beam transport and detection efficiency of the new measurement routine will be presented.

6.3.1. Cooler transmission

A new cause of efficiency loss is the RFQ cooler in the ILIAMS setup. The injected current dependency of its transmission was already revealed during experiments on the ILIAS test setup (see Chapter 2.3.4).

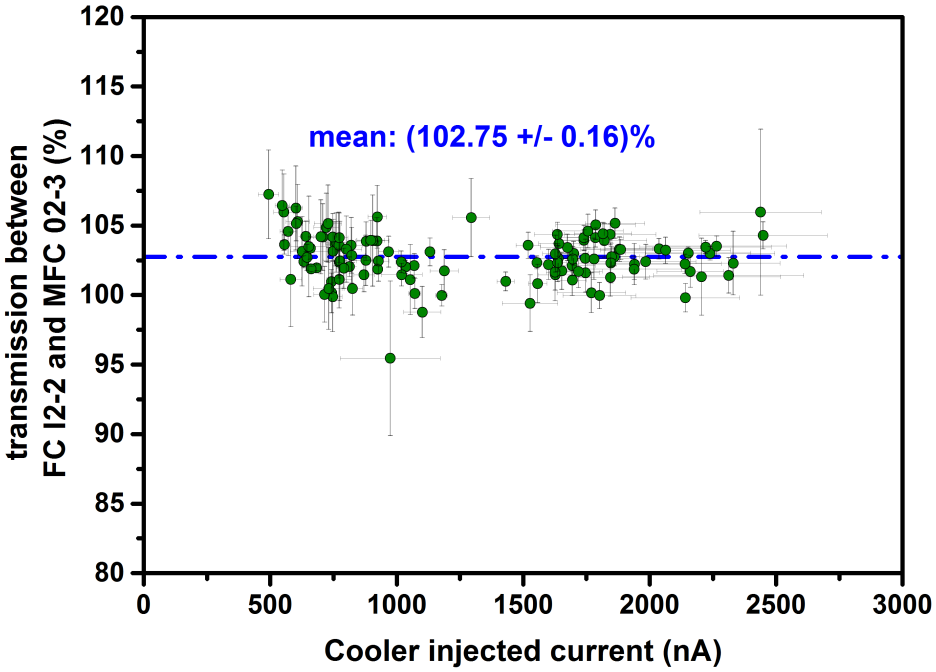

Figure 6.2.: Transmission between Faraday cup FC I2-2 and MFC 02-3 as a function of the injected cooler current. On average, the data reveals almost 3 % higher current values in MFC 02-3, independent of the injected current. This is expected to originate from wrong positioning of the Faraday cup FC I2-2 inside the beam line.

During ILIAMS measurements the cooler transmission was calculated by comparing the current values of the Faraday cups FC I1-1 and MFC 02-3. The Faraday cup FC I1-1 is the closest possible measurement opportunity to the cooler injection and is therefore the obvious choice. The Faraday cups closest to the cooler exit are FC I2-1 and FC I2-2. Data analysis after the first measurement revealed that these Faraday cups could not be trusted. Therefore, the third closest Faraday cup MFC 02-3, which revealed even higher ion current values than FC I2-2 (Figure 6.2), was chosen as a measurement point for future measurements.

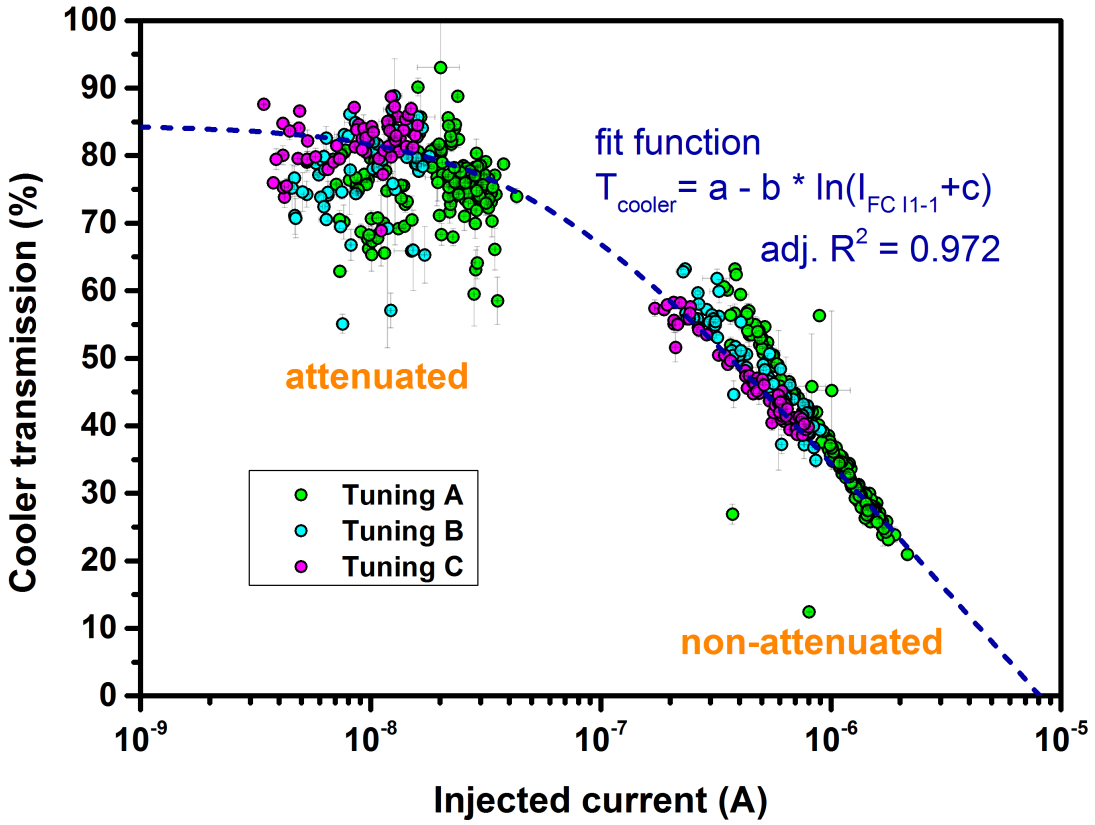

Figure 6.3.: Cooler transmission as a function of the injected current. Data was acquired during the sample measurement in August 2017 (Cl1708). Each data point corresponds to the average transmission over the iterations of a sequence run. The transmission values of Tuning C were fitted by an empirical logarithmic function, which shows good agreement with the experimental data.

The injected and extracted ions of the cooler are in charge state -1 and the cooler transmission T_{cooler} can simply be calculated as

$$T_{cooler} = \frac{I_{MFC\,02-3}}{I_{FC\,I1-1}} \tag{6.1}$$

During the automatic ^{36}Cl measurements, the recording of the cooler transmission is implemented. The monitoring is done for both, the attenuated and the non-attenuated injection into the cooler and therefore reveals the transmission of two injection current ranges (Figure 6.3).

The decrease in transmission at higher injection currents, was observed in previous experiments and is attributed to space charge effects [Moreau, 2016]. The non-attenuated transmission indicates a logarithmic behavior and an accurate fit of the Tuning C data could be done with the empiric function

$$T_{cooler} = a - b \cdot ln(I_{FC\,I1-1} + c) \tag{6.2}$$

where the three constants a, b and c are assumed to be correlated to the machine tuning. Below an injection current of 50 nA the transmission of the attenuated beam shows higher fluctuations between individual runs. The injected current during the detection of ^{36}Cl events can not be compared to these higher currents, its transmission can therefore only be assumed to be greater than 80 %.

6.3.2. Accelerator transmission

In contrast to the cooler, the ions injected into the accelerator undergo a stripping process at the accelerator's terminal. At VERA either a stripping foil, or a stripping gas can be used. Measurements prior to this master's thesis and also the first ILIAMS measurement in January 2017 were carried out in the high energy charge state +7 to reach high ion energies. A carbon stripping foil was used during these measurements, because gas stripping suffers from a very poor +7 yield (Figure 6.4). Later ILIAMS measurements of ^{36}Cl were carried out in charge state +2, where the theoretical stripping yield promises higher efficiency (Figure 6.4).

During the ^{36}Cl measurements in January and August 2017, the accelerator transmission was monitored. For the calculation the current values of the Faraday cups MFC 02-3 and MFC 04-3 were used. The current measured in MFC 04-3 is already in the selected high energy charge state Q. Therefore the measured transmission $T_{acclerator}$ combines stripping and transmission efficiency and is calculated as

$$T_{accelerator} = \frac{I_{MFC\,04-3}}{Q \cdot I_{MFC\,02-3}} \tag{6.3}$$

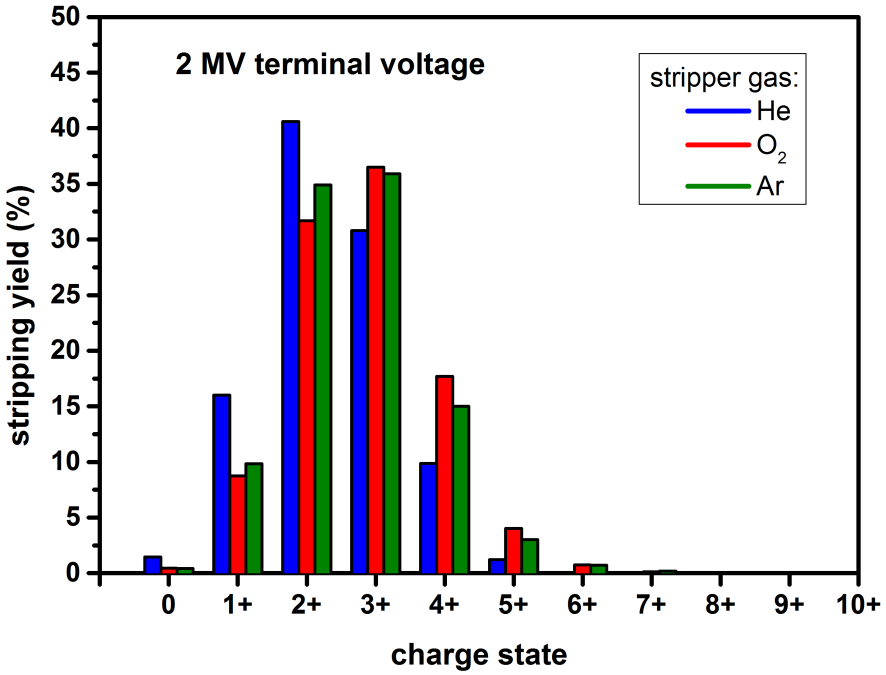

Figure 6.4.: Stripping yield of 2 MeV chlorine ions for different stripping gasses. The data is taken from Wittkower and Ryding [1971].

Similar to the cooler transmission, the accelerator transmission was analyzed in its injection behavior (Figure 6.5).

During carbon foil stripping about 11 % of the injected ions could be measured in charge state +7. The value of 16 % stated in the work of Martschini [2012] could not be reached. This might correspond to the use of a worn out carbon foil. In contrast to the almost invariant accelerator transmission during foil stripping, the gas stripping measurements show a dependency similar to the cooler transmission. The transmission of the non-attenuated beam rises up to 28 % at about 100 nA. Typical values of the accelerator transmission for attenuated beams are in range 30-37 %. The higher transmission fluctuation of the +2 charge state may results from stripping gas pressure variations.

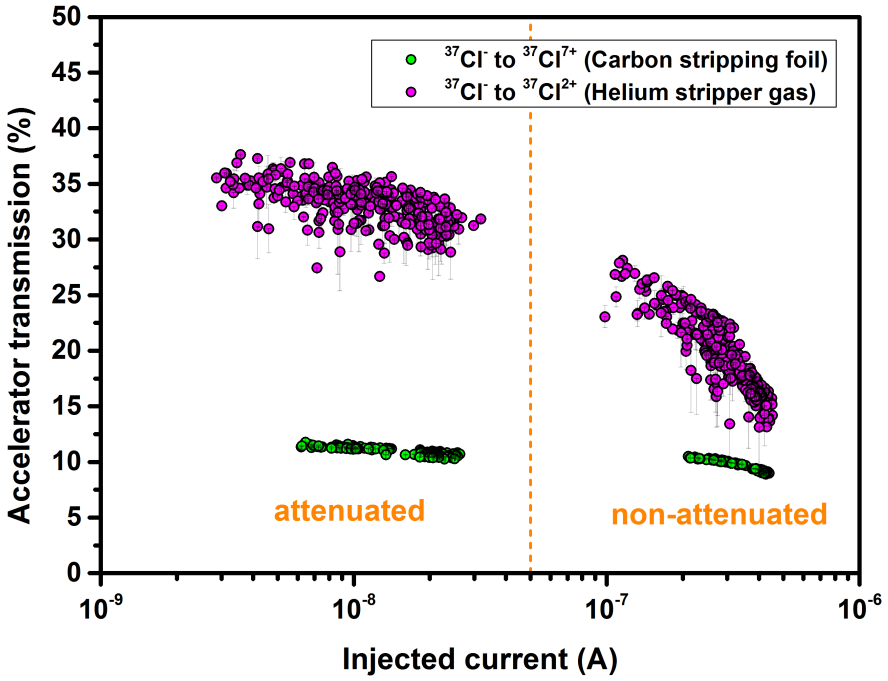

Figure 6.5.: Accelerator transmission as a function of the injected current. Carbon stripping into a Q= +7 cation achieved transmission values of about 10 %. Using helium gas for stripping into the charge state Q= +2, transmission values greater than 30% could be reached for low injection currents (<40 nA of $^{37}Cl^-$).

6.3.3. Detector isobar separation

During the measurement of unknown samples the MAIC detector was used for rare isotope detection. The MAIC detector has three anodes and can therefore measure the energy loss in three successive volumes [Buchriegler, 2013]. As already mentioned in Section 2.2.1, the elements sulfur and chlorine differ in their energy loss. At high energies the anode signals, which are proportional to the energy lost in a detector volume, can be used to distinguish the ^{36}Cl events from its ^{36}S interference (Figure 6.6). The position and the separation of the isobaric events in a two anode plot is correlated to the detector gas pressure and the ion energy.

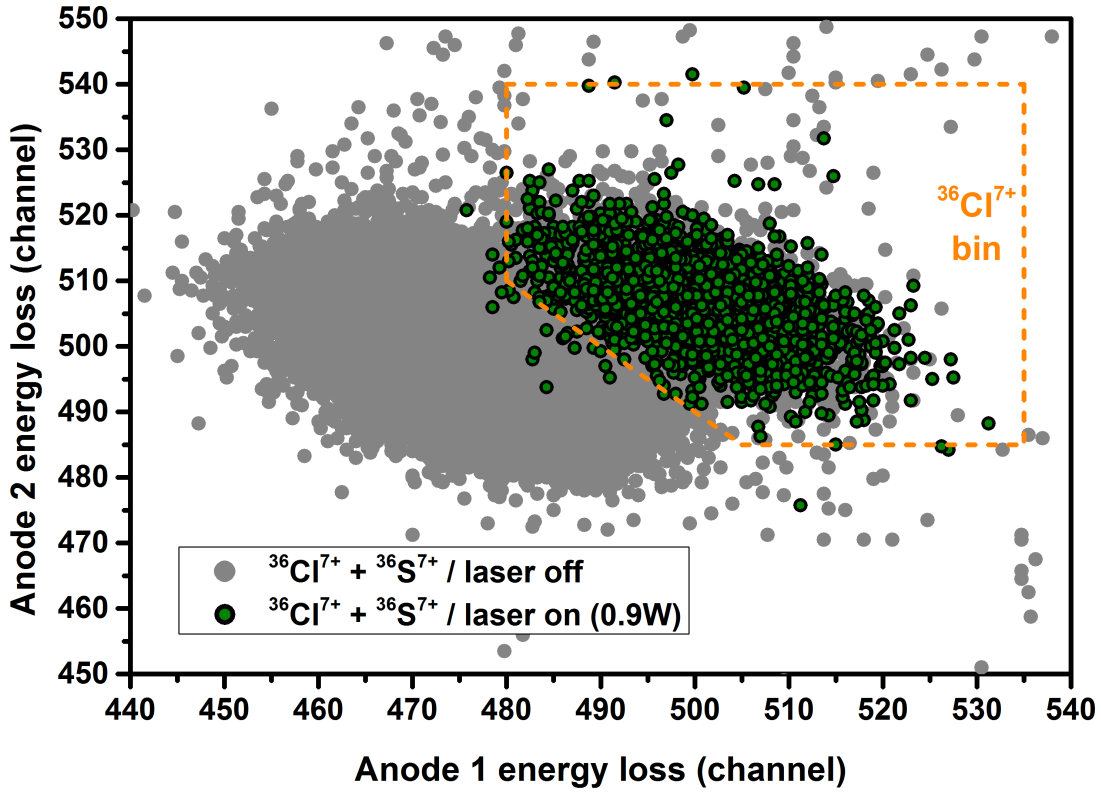

Figure 6.6.: Two recorded MAIC detector spectra during the $^{36}Cl^{7+}$ (E_{ion}=24.4 MeV) measurement in January 2017 (beamtime Cl1701b). The gray dots show a $^{36}Cl^{7+}$ measurement spectrum dominated by the $^{36}S^{7+}$ interference. The green dots represent the measured events with turned on laser. This visualizes the actual $^{36}Cl^{7+}$ region. In both cases the signals from the first two detector anodes were used to represent the events and the detector pressure was set to 30.77 mbar. An example of bins and conditions, used for the identification of $^{36}Cl^{7+}$ events, is drawn in orange.

The identification bins of the isobars have to be set accordingly and a regulation of the pressure is required. In contrast to previous ^{36}Cl measurements at VERA the bins were set relatively large, which is justified by the additional use of the photodetatchment suppression.

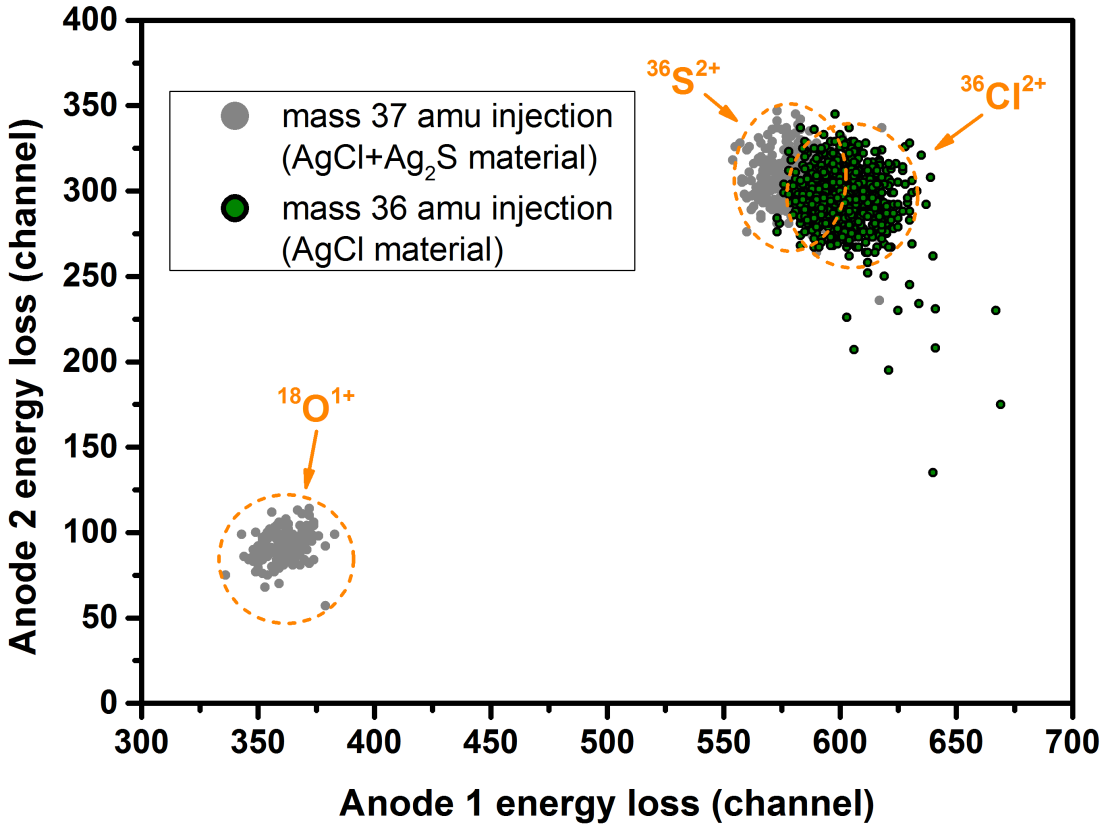

Figure 6.7.: Two recorded MAIC detector spectra during the $^{36}Cl^{2+}$ (E_{ion}=5.27 MeV) measurement in August 2017 (beamtime Cl1708). Both spectra were recorded at 5.5 W transmitted laser power. During the non-attenuated injection of a mass 37 amu beam into the cooler (gray data points), events of $^{36}S^{2+}$ and $^{18}O^{1+}$ were detected. At mass 36 amu injection (green data points) only the $^{36}Cl^{2+}$ peak is visible in the spectrum.

The measurement in August 2017 was carried out for the selected high energy charge state +2. This charge state has a higher gas stripping yield, but the lower ion energy resulted in a worse separation between the isobars $^{36}Cl^{2+}$ and $^{36}S^{2+}$ (Figure 6.7). The lower charge state also allows the transmission of the m/q interference $^{18}O^{1+}$ to the detector.

The low electron affinity of the required molecular forms at the low energy side (EA(HO_2)=(1.078±0.006) eV, EA(O_2)=(0.450±0.002) eV [Rumble, 2018]) suppress them and no additional peak is visible in the spectrum during mass 36 amu injection. During the non-attenuated mass 37 amu sequence the spectrum shows $^{36}S^{2+}$ and $^{18}O^{1+}$ events in the detector. This suggests non suppressed molecular forms at this mass. Potential candidates for ^{36}S would be the hydride form $^{36}S^{1}H$ which has an electron affinity close to the photon energy of the laser (EA(SH)=(2.3147282±0.0000015) eV [Rumble, 2018]). In the case of ^{18}O the already encountered $^{19}F^{18}O$ form (EA(FO)=(2.272±0.006) eV [Rumble, 2018]) is assumed to be responsible for the detected events.

Further investigations in October 2017 were conducted with a different dual anode ionization chamber following the ETH design [Forstner et al., 2008] [Suter et al., 2007]. The new ionization chamber (GIC L4) is located between the high energy ESA and the switching magnet and replaced a silicon surface barrier detector. Measurements in charge state +2 have already been carried out with it and the spectrum resembles the one presented in Figure 6.7.

These presented detector spectra prove once more the high suppression of ^{36}S and allowed bin settings covering the whole ^{36}Cl peak of the spectrum. The pile up effect due to the high ^{36}S count rate is not present and the aperture inside the detector is not required anymore. Therefore, the detector efficiency increases to about 100 %.

6.4. System stability

During the experimental work of this thesis, the RFQ cooler had proven challenging in terms of transmission and measurement stability. This section will present the gathered experience and the possible corrections during data evaluation.

6.4.1. Stability indicators

In order to decide whether a machine setup is trustworthy or not, the recorded and calculated data was analyzed. Indicators for a stable machine condition were found to be the normalization factor and the transmission through cooler and accelerator.

Normalization factor

The normalization factor is the inverse fraction between the measured ^{36}Cl/Cl ratio and the nominal ^{36}Cl/Cl value of the same standard.

$$normalization\ factor = \frac{(^{36}Cl/Cl)_{nominal}}{(^{36}Cl/Cl)_{measured}} \tag{6.4}$$

During both major sample measurements the ^{36}Cl/Cl ratio was calculated using the ^{36}Cl detector events and the ^{37}Cl high energy current. A time independent normalization factor indicates no drift of the machine setup and a good measurement condition of the system. An AMS measurement at VERA usually involves the measurement of more then one standard cathodes, which should be evenly distributed across the cathode wheel. A good agreement between their individual normalization factors indicates no significant dependency of the wheel position and assures similar transmission through the system.

The temporal development of the normalization factor during the measurement in January 2018 indicates three different conditions of the system (Figure 6.8). From the start of the measurement at t≈13 h to t≈67 h the mean normalization factor is 47.6 and the corresponding relative scatter (σ/μ) is about 3.5 %. No significant drift is visible and therefore the machine condition is considered to be in a stable state. After this time period, the normalization factor drifted away requiring a re-tuning of the system. After the tuning the system was still in an unstable condition (B in Figure 6.8). During this time the normalization factor decreases to a minimum of 33.2 and afterwards shows regenerating behavior. Even the error bars indicate high fluctuations of the normalization factor during the individual sequence run iterations.

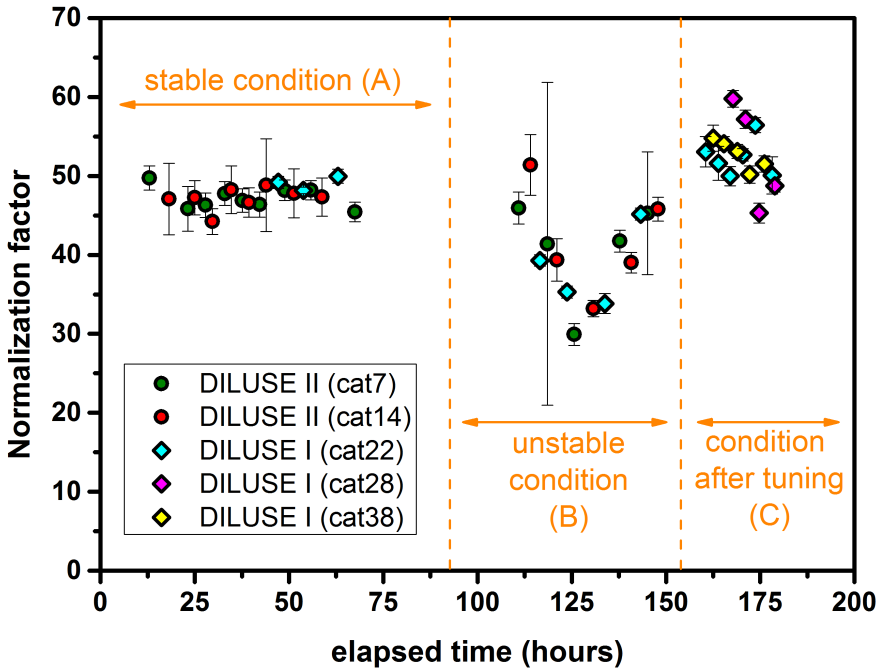

Figure 6.8.: The normalization factor of multiple standard cathodes is plotted against the run number. The initial machine state (A) shows an almost constant normalization factor. The second condition (B) shows the breakdown of the normalization factor followed by an regenerating behavior. The last state (C) was obtained after tuning of the system and resulted in higher values and scatter of the normalization factors.

This unstable condition forced another tuning attempt. This time the non-diluted samples were measured. Their higher ratios, in the order of 10^{-11}, required the use of the highest standard material DiluSe I. Measurements on the new setup resulted in a mean normalization factor of about 52.6, but also an increase of the relative scatter to about 6.9 %.

The decrease in cooler stability measurement in January 2017 was also present at later investigations. In August 2017 the measurement was done using three different machine tunings, each showing higher relative scatter as before (Figure 6.9).

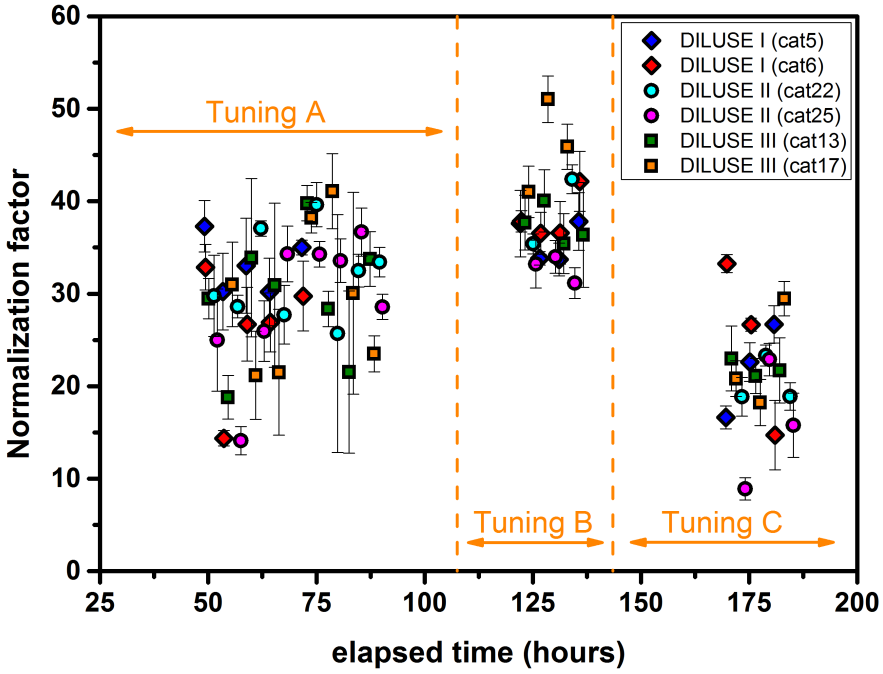

Figure 6.9.: The normalization factor of multiple standards is plotted against the elapsed time to show the behavior of the measurement setup over the measurement period. The stability of the cooler was not optimal during this measurement, requiring two major retunings. The individual tunings will be reffered to as Tuning A,B and C.

During Tuning A the averaged normalization factor was about 29.3 and shows high fluctuations with a relative scatter around 22 %. Differences between individual sequence run iterations also resulted in high normalization factor uncertainties. The second tuning attempt, resulting in Tuning B, revealed that improvement of the system was possible. A mean value of 38.3 with a standard deviation of 4.2 could be achieved for the normalization factor. It should be noted that cathode 17 showed higher normalization factor values than the other standards cathodes during this tuning. During the measurements in Tuning C the procedure was slightly changed and involved an automatic re-tuning step after each cathode change. This re-tuning involved the scan of the source's 2D-steerer and the x-component of the steerer at the exit of the cooler (ESX I1-2). This was done, because previous tuning attempts mainly showed a drift concerning these parameters. Although this procedure was expected to increase the stability of the system, the normal-

ization factor was lower than before (22.1 with a relative scatter of 25 %). Despite the high fluctuations between individual data points it should be mentioned that the re-tuning process resulted in better agreement of the individual sequence run iterations, which is indicated by the smaller error bars.

Transmission

Another indication for a stable cooler condition is the transmission. In contrast to the normalization factor, the transmission values can be calculated for all cathode types. This way it is possible to monitor the measurement stability of blanks and unknown samples. In a plot of the accelerator transmission, as function of the cooler transmission, a difference between the three tunings in August 2017, is visible (Figure 6.10).

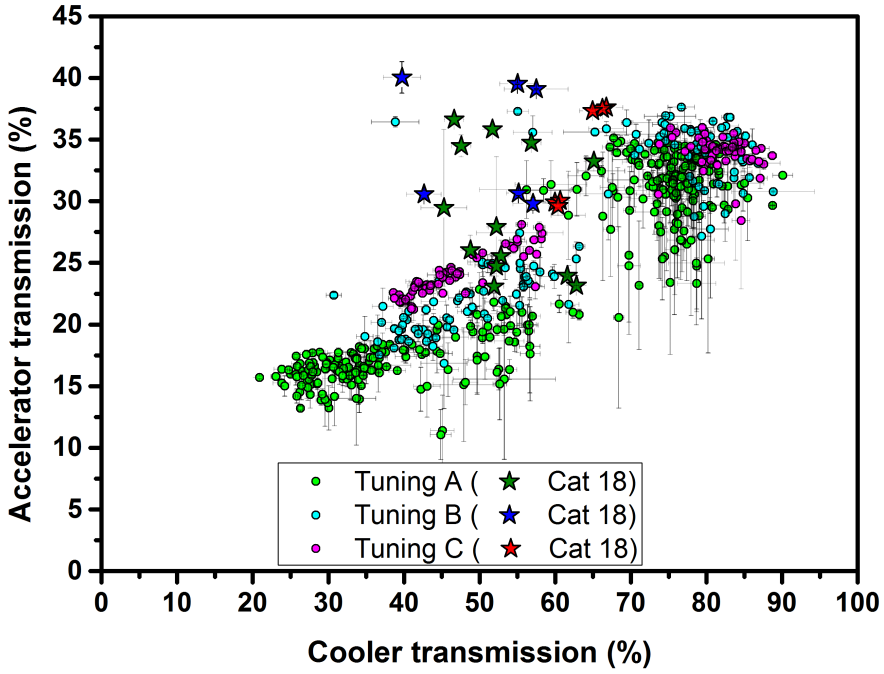

Figure 6.10.: The accelerator transmission as a function of the cooler transmission. The three different tunings (A, B & C) of the measurement performed in August 2017 are shown. Both, the attenuated (cooler transmission $\gtrsim$ 65 %) and non-attenuated values (cooler transmission $\lesssim$ 65 %), are presented, but clear separation is not possible. All values of the cathode 18 are marked separately to display its unusual behavior.

Although tuning C showed a low normalization factor (cf. Figure 6.9), it shows high and stable cooler transmission values. During the measurement in August 2017, the cathode 18 showed especially high values of accelerator transmission, despite its low transmission through the ion cooler. This example shows that the transmission investigation allows the identification of unusual cathode behavior even for non-standard materials.

6.4.2. Influence in data evaluation

The knowledge of the stability behavior was applied in the data evaluation. The time dependence of the normalization factor was used to distinguish between stable and unstable machine conditions. A trend in the normalization factor (e.g. unstable condition B in Figure 6.8) is seen as unstable and the acquired data was not used for evaluation. The absence of a visible trend was considered stable. After the measurement in January 2017 high fluctuations of the normalization factor were always present making the identification of minor drifts impossible. Hence, during later measurements only turns in which the cooler transmission broke down were discarded.

The normalization factor can only be calculated for standards. Therefore, the transmission values were used to reject individual sequence run data. In order to get an acceptance range for the transmission data, a histogram was created for each tuning and transmission type (cooler transmission example in Figure 6.11). A Gaussian distribution was used to fit the histograms. It is visible that this does not perfectly describes the measured distribution, but the lower tail is assumed to originate from short break downs of the cooler system. In the data evaluation all transmission values outside the 5σ range of the fit were rejected. Assuming a pure Gaussian distribution this would correspond to a cut of about 0.6 ppm. Due to the lower tail of the distribution, the actual rejection percentage is dependent on the cooler stability. Although the time evolution of the normalization factor during the tunings A and B look stable (see Figure 6.9), the 5σ condition rejects 12 % and 8 % of the data, respectively. The re-tuning process in the last tuning achieves an rejection percentage of only 1.5 %.

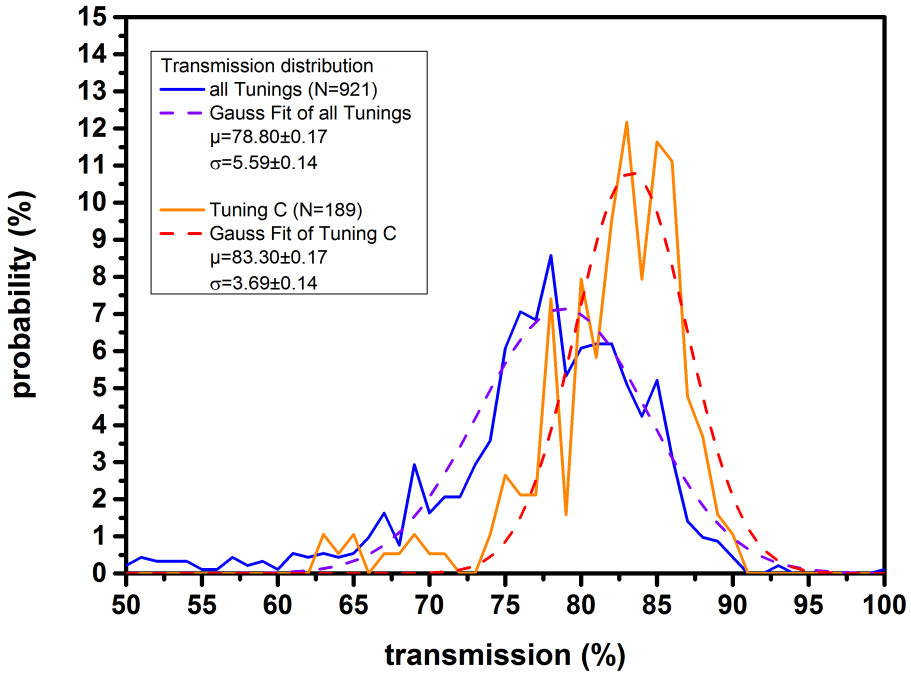

Figure 6.11.: The cooler transmission distribution measured during Tuning C (orange) and the combined distribution of all tunings during the beamtime Cl1708 (blue). Their respective Gauss fits are given by the dashed lines.

The greatest problems encountered during the measurements are short time breakdowns and drifts during the rare isotope detection (Figure 6.12). It should be noted that the presented examples show extraordinary events and do not represent the usually encountered temporal evolution. The "slow bouncing" method of the new measurement procedure does not allow the detection of these breakdowns, because the stable isotope current can not be monitored during the almost 300 second detection time of the rare isotope. This effect introduces an additional error in the data, which may result in an underestimation of the actual isotope ratio. For samples with a high ratio, the individual counts of the sequence run iterations can be used to identify a breakdown or short-term drift event. In the case of low-ratio samples the counting statistics are not sufficient and this instability can not be detected by looking at the recorded data.

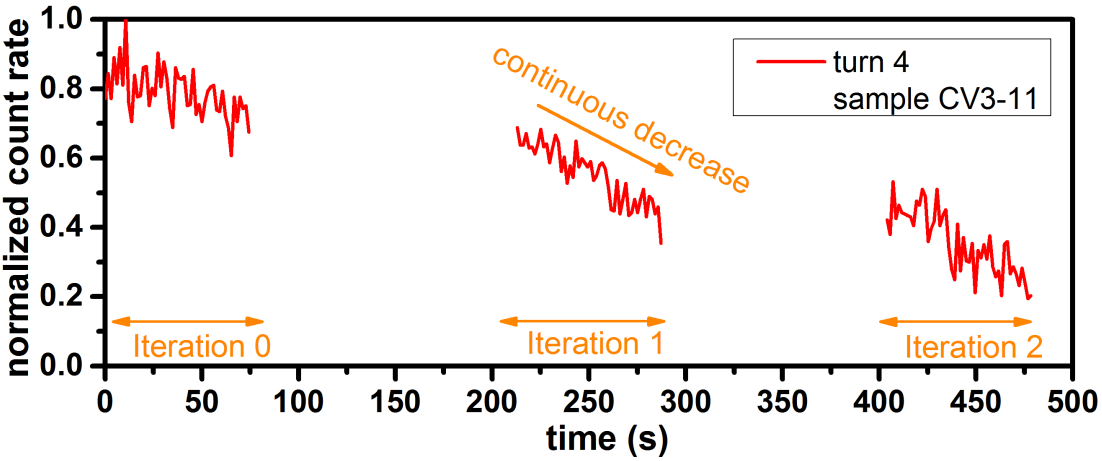

(a) continous decrease

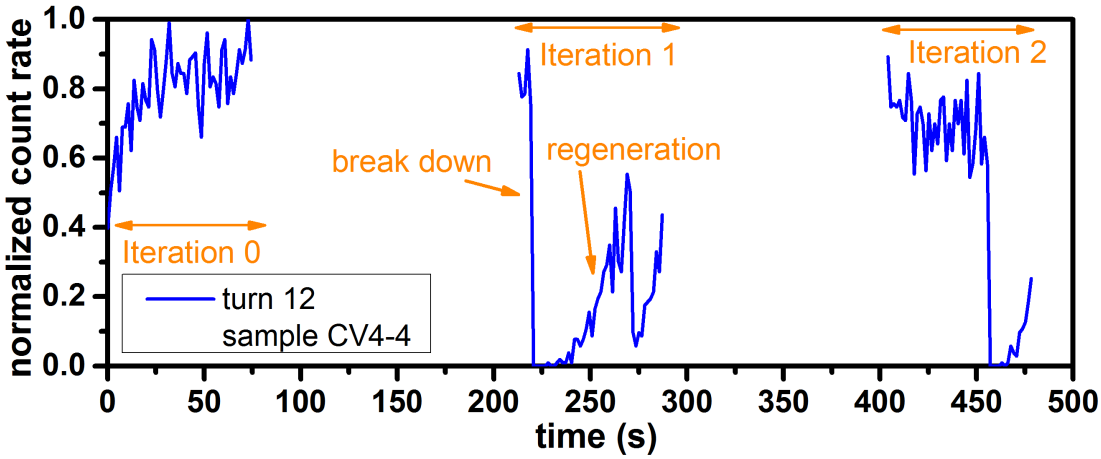

(b) breakdown and regeneration

Figure 6.12.: Time evolution of the event count rate during the iterations of a sequence run. The two extreme examples show two significant instability issues: a continuous drift (a) and a breakdown effect followed by a regeneration (b). The isotope ratio of the presented samples were measured to be in the order of 10^{-11}. Although the continuous drift is also visible in the stable isotope current values, it still introduces an additional uncertainty. The breakdown and regeneration effects are too short to be visible during the stable isotope measurements.

6.5. Measurement precision and reproducibility

In the previous measurement procedure high ratio samples (^{36}Cl/Cl $\geq 10^{-12}$) could be measured with a precision of 0.8 % [Martschini, 2012]. The more limiting factor was found to be the reproducibility of their ratio. The reproducibility of these high ratio samples was determined to be about 2%. This is assumed to come from transmissional losses originating from minor discrepancies in the complex cathode preparation [Martschini, 2012]. The new measurement procedure does not rely on the complex cathode preparation due to its high isobar suppression via photodetachment. The precision and the reproducibility of the individual ratio measurement results was therefore investigated in January and August 2017.

January 2017 (beamtime Cl1701b)			August 2017 (beamtime Cl1708)
SOLA	1AVG	BF	CV 3-2
SOLB	2AVD		CV 3-11
SOLC	3ARG		CV 4-4
SOLD	4ARD		

Table 6.1.: The labels of the unknown sample materials measured in January and August 2017. All of these materials were also available and measured in diluted form.

6.5.1. Precision

During the January beamtime (Cl1701b) a total of 9 unknown sample materials were measured and available in both, a diluted and an non-diluted form (Table 6.1). For high ratio samples (^{36}Cl/Cl $\approx 10^{-10}$ - 10^{-12}) the total rare isotope detection time was about 15 minutes. During this time the cathodes were determined with an average precision of about 4 %. Samples with lower ratios were measured for 55 minutes on average. This resulted in the precision of 3-4 % for ratios in the order of 10^{-13} and 6-23 % precision for 10^{-14} ratios. The lowest sample was determined to have a ratio in the 10^{-15} region and could only be measured with a precision of 58% during this time. In all cases the ratio uncertainty of a sequence run (recall Section 6.2) is dominated by the scatter of the individual values of its

iterations and not by counting statistics. Because of this, all presented error bars of ratio data points result from the scatter of the sequence run iterations, which are also responsible for the measurement precision (Figure 6.14).

The measurement in August 2017 involved the determination of 3 unknown sample materials, which were also measured in diluted and non-diluted form (Table 6.1). The detection time for each sample was about 45 minutes. During this time the non-diluted samples were determined to be in the order of 10^{-11}-10^{-12} with an average precision of about 5 % (e.g. Figure 6.13). The diluted samples showed ratios in the range 10^{-14}-10^{-15}. The blank cathodes showed ratios comparable to the diluted materials and the blank correction would have resulted in negative values (Figure 6.15). Without the blank correction, the achieved precision for the diluted samples was in the range of 7-11 %. Like for the measurement in January the precision of the measured ratios was dominated by the scatter of the sequence run iteration values.

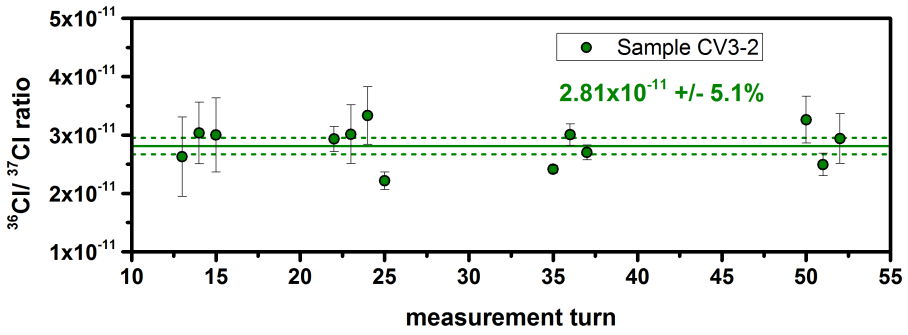

Figure 6.13.: An example of measurement results in August 2018 (beamtime Cl1708). The selected charge state was 2+ and the detection time was about 45 minutes. The solid and dotted lines represent the weighted mean and its uncertainty, respectively. The individual data points values were obtained during the sequence run of the respective measurement turn. Some measurement turns had to be discarded due to system instability reasons.

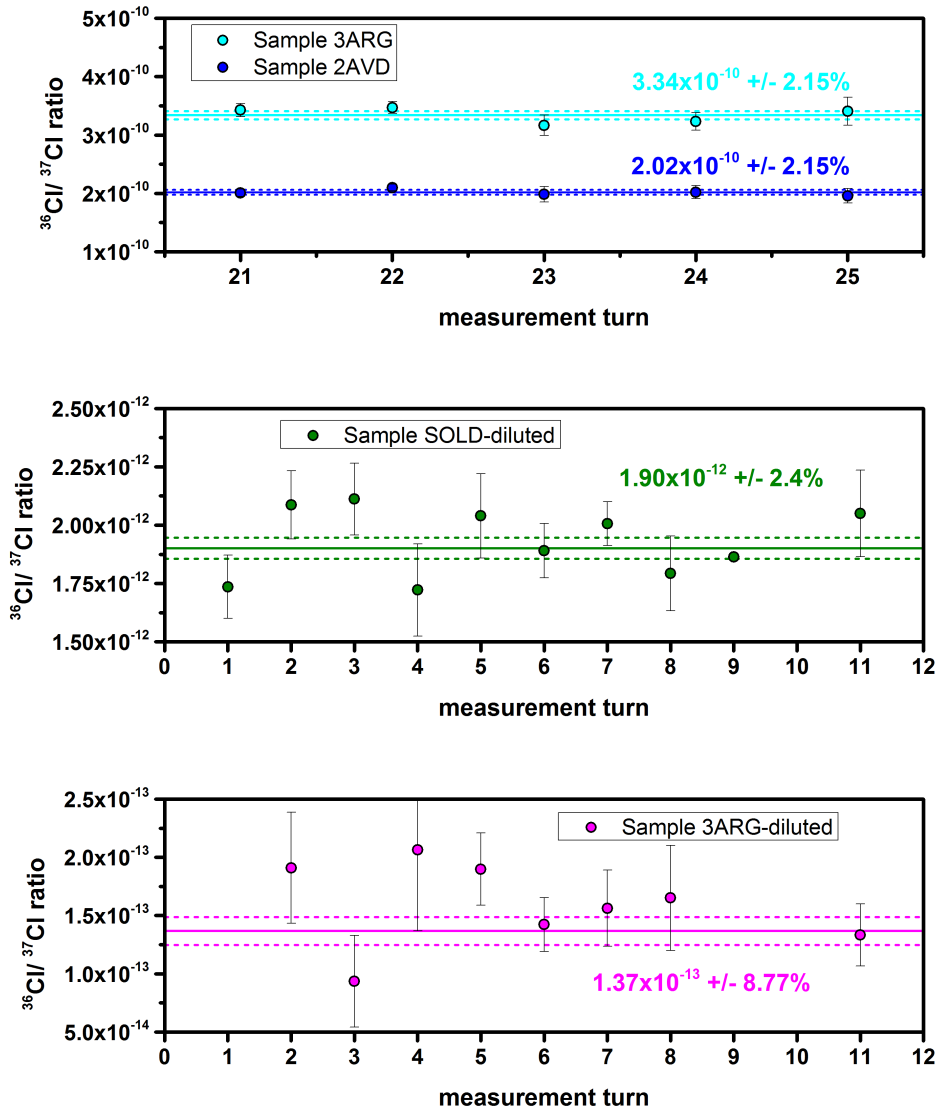

Figure 6.14.: Results of sample measurements in January 2017 (beamtime Cl1701b). Samples in the ratio regions 10^{-10} (top), 10^{-12} (middle) and 10^{-13} (bottom) were determined with a precision better than 10%. The selected charge state was 7+ and the detection time was about one hour. The solid and dotted lines, respectively represent the weighted mean and its uncertainty. The individual data point values were obtained during the sequence run of the respective measurement turn. Some measurement turns had to be discarded due to system instability reasons.

6.5.2. Reproducibility

The reproducibility of a sample ratio was determined for 3 different cases. At first the ratios of two cathodes with identical material was investigated. The same material (CV3-2) was pressed into two ordinary cathodes and placed in the cathode wheel adjacent to each other. The weighted mean ratios were measured as:

$$\text{CV3-2\_a: } {}^{36}\text{Cl/Cl} = (2.16 \pm 0.17) \cdot 10^{-14}$$
$$\text{CV3-2\_b: } {}^{36}\text{Cl/Cl} = (1.90 \pm 0.17) \cdot 10^{-14}$$

The individual turn ratios of both cathodes show high scatter (Figure 6.15), but the weighted mean ratios agree within their 1σ uncertainties.

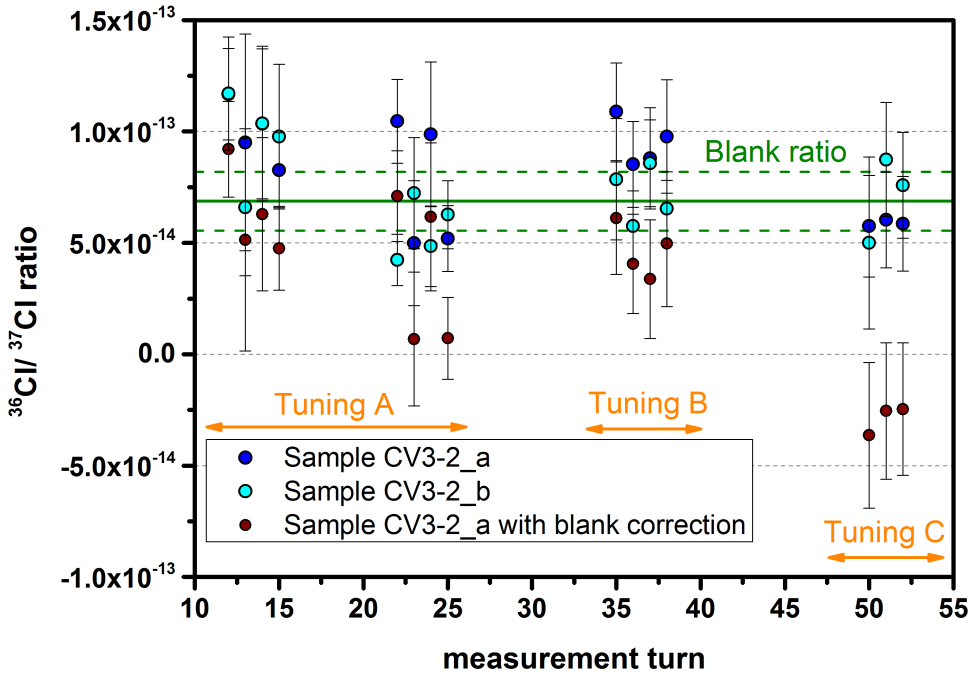

Figure 6.15.: The ratio of two cathodes with identical target material as a function of the measurement turn. In August 2017 (beamtime Cl1708) ratio values without blank correction (cyan and blue) show good agreement in terms of their uncertainties. By applying an overall blank correction negative values were reached (red).

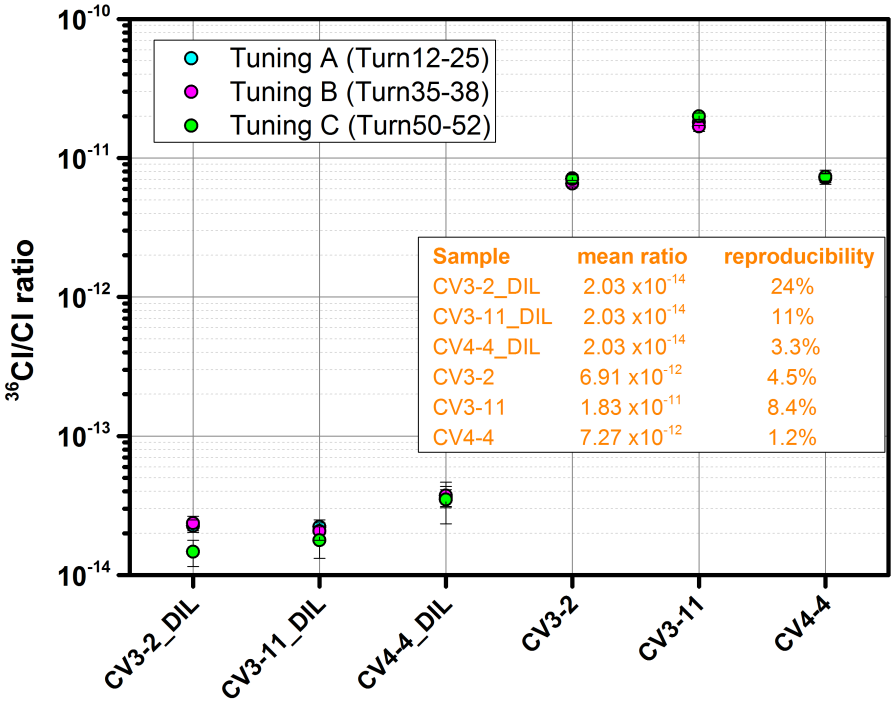

Figure 6.16.: Comparison of sample ratios obtained during the different tunings of the measurement in August 2017 (beamtime Cl1708). Ratios higher than 10^{-13} could be reproduced below a 10 % difference. Lower ratios vary by up to 24%, where especially Tuning C shows bad agreement with the other tunings.

Since different tunings had shown to affect the system stability, the ratios obtained during the individual tunings in August 2017 were investigated (Figure 6.16). While the ratios of the non-diluted samples show a 1σ standard deviation of less then 10 % of the mean value, the diluted ratios show values up to 24 %. The tunings A and B show good agreement, but the values of Tuning C differs at these low ratios. The last investigation on the reproducibility involved the determination of an already measured material. A high ratio material (Z7-1-B-2) was determined in 2015 at VERA using the measurement procedure without photodetachment. During the measurment in January 2017 the ratio of this material was measured again and the obtained value agrees with the previous one within their uncertainty (Figure 6.17).

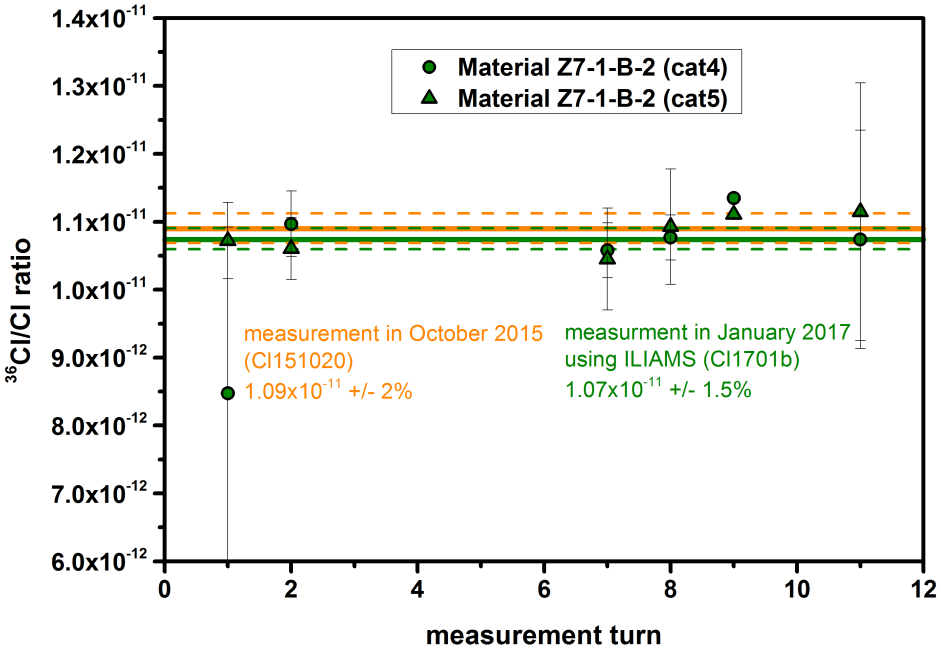

Figure 6.17.: Reproducibility of a previously measured sample material. The ratio determined in 2015 with the old measurement routine (orange line) lies within the uncertainty of a new measurement carried out in January 2017 with the ILIAMS setup.

6.6. Detection limits

During the measurement in August 2017 the blank level had proven to be a crucial point in the system's performance. The used blanks showed ^{36}Cl/Cl ratios in the order of 10^{-15} and could not be used to determine diluted samples with the desired precision. The lowest ratios were found in the sulfur spiked materials of batch #2a and #2b (more information in Section 4.1). In October 2017 another beam time (Cl1710) was scheduled to characterize this material and with it the performance of the new measurement routine for chlorine.

6.6.1. Blank value

The blank value is an important quantity when talking about limits in AMS. It determines the lowest ratio that can be measured at the facility. In order to make quantitative statements about this value the appropriate material has to be chosen. As mentioned before, the in-house produced sulfur spiked materials revealed an lower ^{36}Cl/Cl ratio than the previously used blanks. The high sulfur content of the spike material turned out to be an actual advantage. It can be used to fine-tune the laser setup in order to maximize the laser photodetachment suppression. In addition a potential drift of the laser alignment can be monitored by using its measured spectrum.

At first the measurement in October revealed ^{36}Cl/Cl ratios in the order of 10^{-15} (Figure 6.18). By increasing the ion source output and the ^{37}Cl current accordingly a trend towards lower ^{36}Cl/Cl ratios was found. By looking only at the ratios measured during the increase of the source output, the blank material showed an average ^{36}Cl/Cl ratio of $(6.46\pm1.94)\cdot10^{-16}$. During this investigation the source output was not increased up to the point where a ratio minimum is expected. Therefore, the presented value can be seen as an upper bound of the actual blank value.

6.6.2. Cross contamination

During the blank value investigation a niobium target, which is expected to have a low chlorine content, was included in the measurement. The ^{36}Cl count rate of the niobium material was in the same order as for the spiked targets, which suggests a source of contamination.

A contamination during the target preparation would result in an higher ratio in the sample and could not describe the decreasing ratio at higher source output (cf. Figure 6.18). A contamination by the use of the ion cooler can be ruled out. The typical residence time is in the order of 2 ms during the injection of a 3.2 nA ion beam (cf. Figure 2.10). Therefore, no ^{36}Cl ions inside the ion cooler survive the 6 minute delay between cathode measurements. In addition the prior measure-

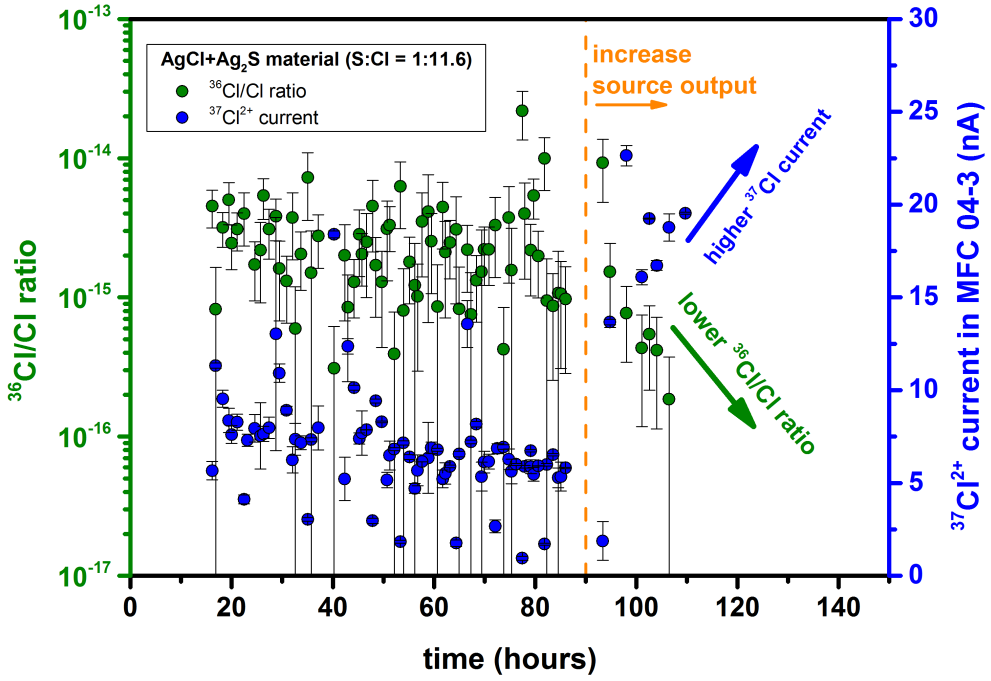

Figure 6.18.: Normalized blank ratio and high energy current as a function of the measurement time. After increasing the source output, the increased ^{37}Cl currents resulted in a trend towards lower ^{36}Cl/Cl ratios. This indicates a contamination inside the ion source. Note that the ratio axis is plotted logarithmic, while the current is presented on a linear scale.

ment of the stable isotope is expected to "wash out" the contained ions due to its higher space charge. Due to these reasons, the contamination is therefore to happen inside the ion source.

To determine whether this is a localized effect, or the whole source is contaminated with ^{36}Cl, two types of standards form the DiluSe series were used. Sequences of standard, blank and niobium materials were evenly distributed around the cathode wheel to achieve maximum distance between them (Figure 6.19). The niobium targets are not expected to contain high amounts of chlorine. As expected, their measurements revealed low stable isotope currents in the noise level of the Faraday

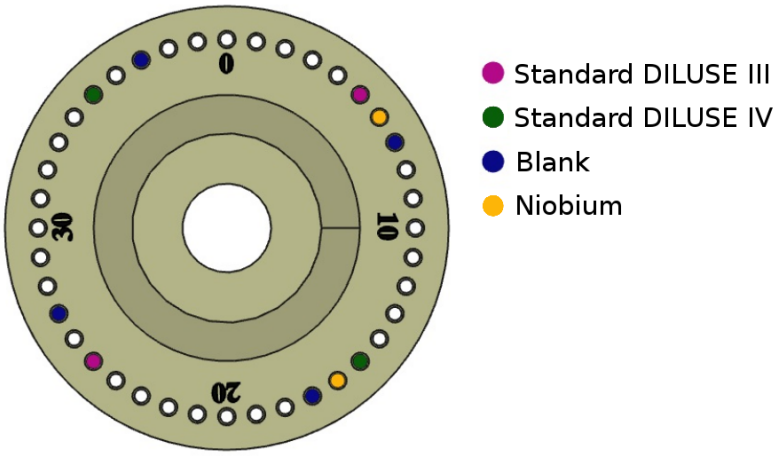

Figure 6.19.: The positions of the individual targets mounted to the cathode wheel.

cup during the automatic measurement. Due to this low ion current, the ^{36}Cl ratio could not be calculated for the niobium targets and only the detector count rate was compared to the other materials (Figure 6.20).

The count rate of the sulfur spiked material is in the same range as that of the niobium targets. The use of the two different Standard materials DiluSe III (^{36}Cl/Cl = (3.627±0.082)· 10^{-13} [Martschini, 2012]) and DiluSe IV (^{36}Cl/Cl = (1.310±0.034)· 10^{-13} [Martschini, 2012]), would allow the detection of localized contamination effects near the standard cathode. Although the standard ratios differ by a factor of 3 no significant effect could be observed at the closest targets. Because of these results, the source contamination is expected to effect every cathode in the wheel, independent of their position.

This memory effect was also observed during the investigations by Martschini [2012] at Source 1 of the VERA facility. Also Argento et al. [2010] reported this effect during the determination of ^{36}Cl in seawater. The presented ^{36}Cl/Cl ratios in their work were measured at the Australian National University (ANU), where the 14 MV terminal voltage resulted in 112 MeV ions in charge state +7. Due to the simultaneous measurement of 10^{-12} ratios, their blank level was reported to be in the order of 10^{-16}. This is also the observed region encountered during the ILIAMS investigation.

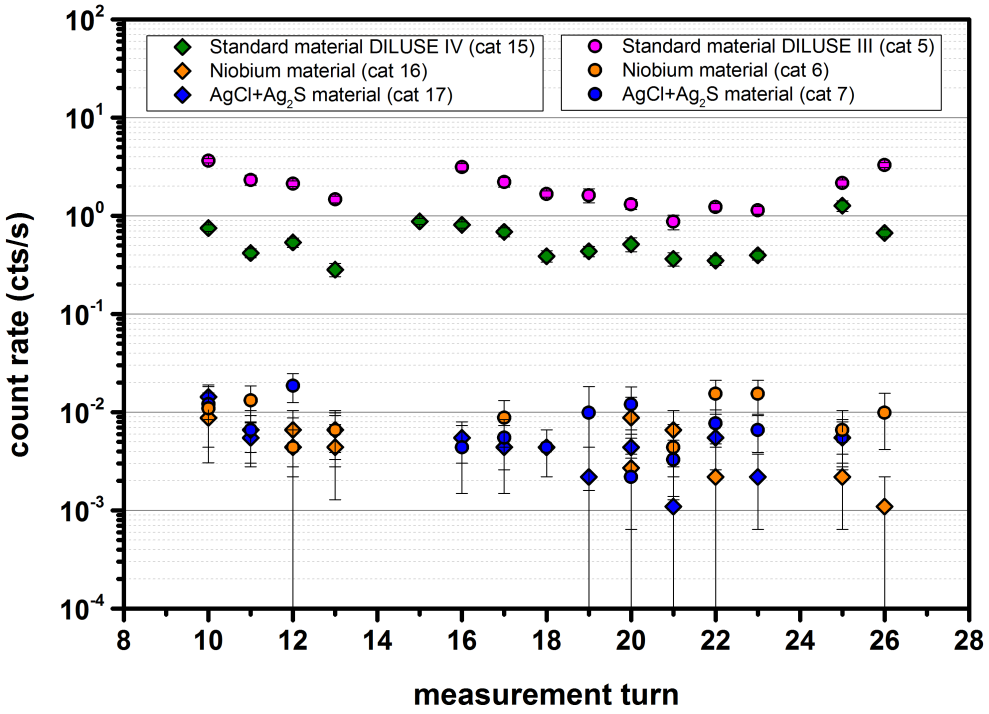

Figure 6.20.: Detector count rates of various cathodes as a function of the measurement turn. The cathodes were sputtered in the order: Standard, Niobium, Blank. Although the isotope ratio of the standard materials differ almost by a factor of three, a clear separation of the other cathodes is not possible when looking at the count rates.

7. Conclusions and Outlook

A new ^{36}Cl measurement routine at VERA, using its new ILIAMS setup, has successfully been developed.

First photodetachment suppression measurements of sulfur isotopes have been done. Although only lower limits could be calculated for ^{36}S events, the more abundant ^{34}S isotope revealed a suppression factor in the order of 10^{10}. This value is sufficient enough to set coarse conditions on the detector data, resulting in a detector efficiency of nearly 100 %.
The investigation of possible molecular interferences revealed that a potential carbon background can already be suppressed by a combination of the photodetachment process of a green laser and the mass filter of the low energy beamline. The fragments of the isobaric molecule FO were the only observed interference at the accelerator exit. The electron affinity value of FO is close to the laser energy and therefore only moderate suppression could be shown.
The ILIAMS chlorine measurement in January 2017 showed stable measurement conditions. This allowed the determination of sample ratios in the order of 10^{-12} with a precision of about 2.4 %. During blank level investigations an already known memory effect of the source could be shown, which limits the determination of low ratio samples (^{36}Cl/Cl$\approx 10^{-15}$). Later measurements revealed a more unstable condition of the system and the source of this additional error turned out to be the RFQ cooler.
Compared to the previous measurement routine the ILIAMS measurements are more efficient. Along with the improvement in detector efficiency by a factor of 2, the selection of the charge state 2+ results in a twice as high stripping yield and a previously required sulfur reduction during cathode preparation is not required anymore.

So far, all discovered and identified interferences contributing to the background have lower electron affinity vales than ^{36}Cl itself. The use of a laser with higher photon energy is expected to suppress the observed FO molecule sufficiently, which would make measurements without the use of a tandem accelerator feasible. In this case the efficiency of the measurement would be further increased, due to the absence of the stripping process.
The successful ILIAMS measurements of ^{36}Cl open up new possibilities in mass spectrometry. In the future laser photodetachment suppression may allow the determination of new isotope concentrations (e.g. ^{135}Cs and ^{182}Hf), which are presently not in reach of usual AMS setups.

A. VERA Scheme

In Figure A.1 a detailed scheme of the VERA system is given. The new ILIAMS system is included and various important ion filter parameters are listed.

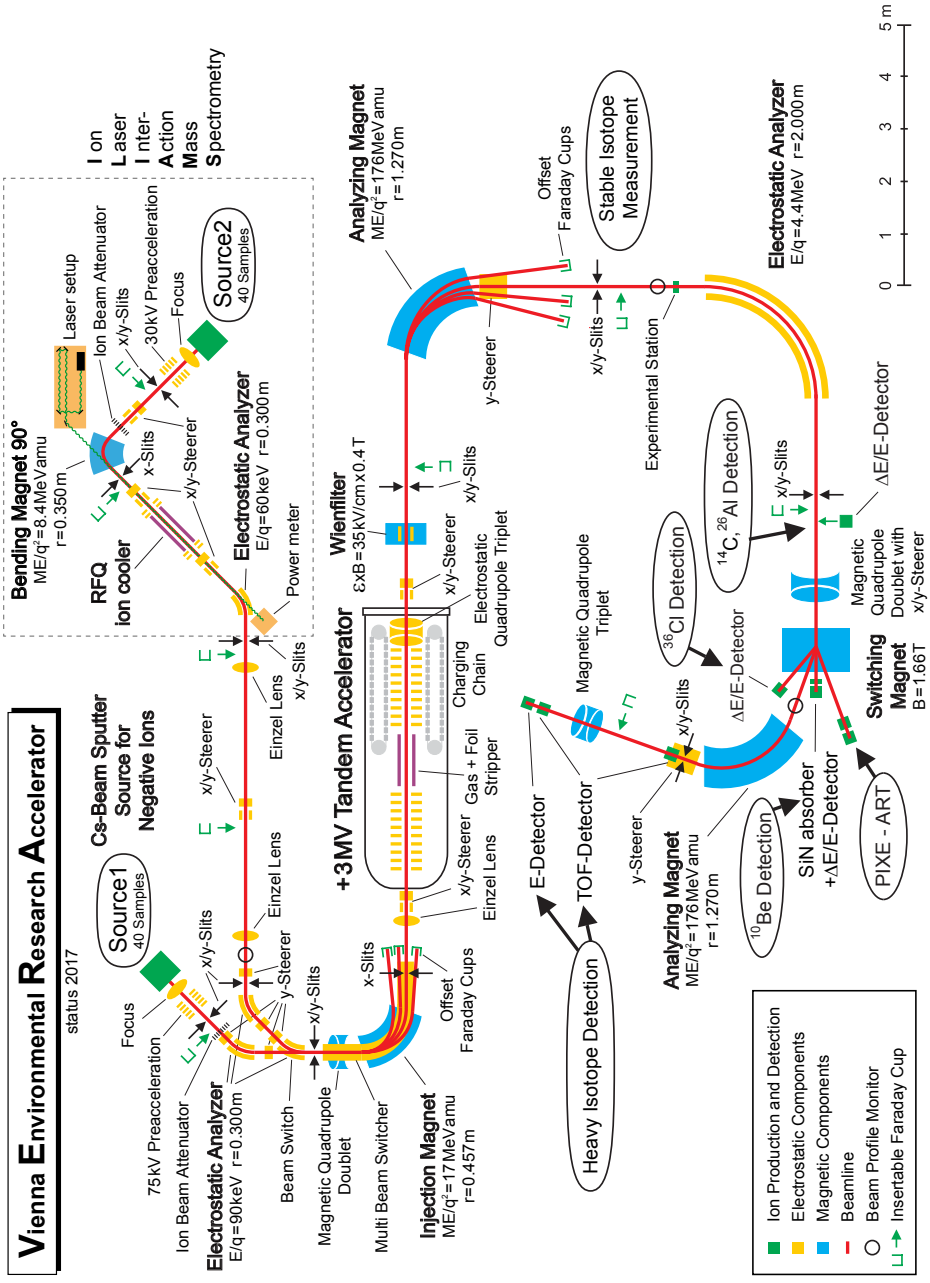

Figure A.1.: A detailed scheme of the VERA setup in late 2017.

B. Steerer phase space y-direction

The Figure B.1 shows the y-phase space for different steerer parameters during SETUP2 measurements. The large impact of the x-steerer component in Figure B.1c does not compare to the other 3 settings and therefore a systematic error during the aquisition is expected.

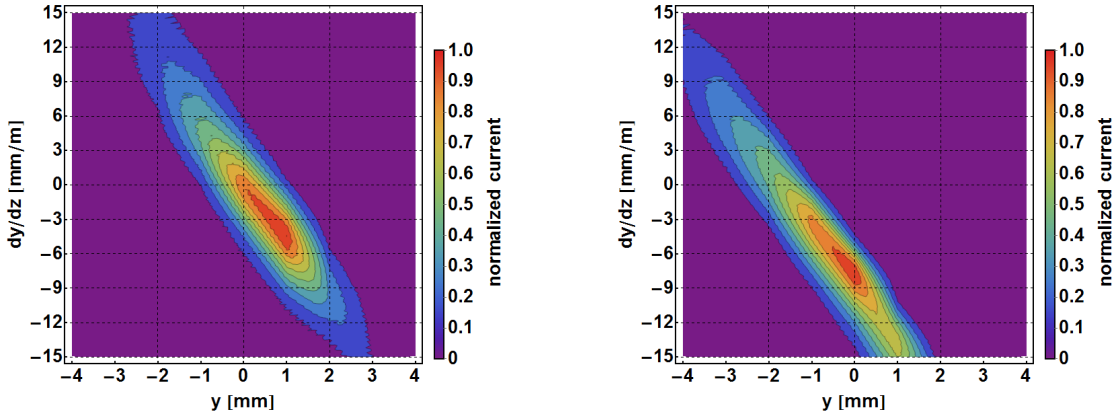

(a) X-Steerer: 0V , Y-Steerer: 0V

(b) X-Steerer: 0V , Y-Steerer: -500V

(c) X-Steerer: -250V , Y-Steerer: 0V

(d) X-Steerer: -250V , Y-Steerer: -500V

Figure B.1.: The y-phase space for different steerer parameters during SETUP2 measurements. Further information on the measurement can be found in Chapter 3. The large impact of the x-steerer component in (c) does not compare to the other 3 settings and therefore a systematic error during the acquisition is expected

C. Laser setup

A drawing of the 150x60 cm^2 breadboard from THORLABS® and the mounted optical elements can be found on the following page. The positions of the mounted elements are also given in units of mm. The drawing was made with [FreeCAD, 2018] and for the identification of the optical elements it is advised to compare the drawing with Figure 3.9.

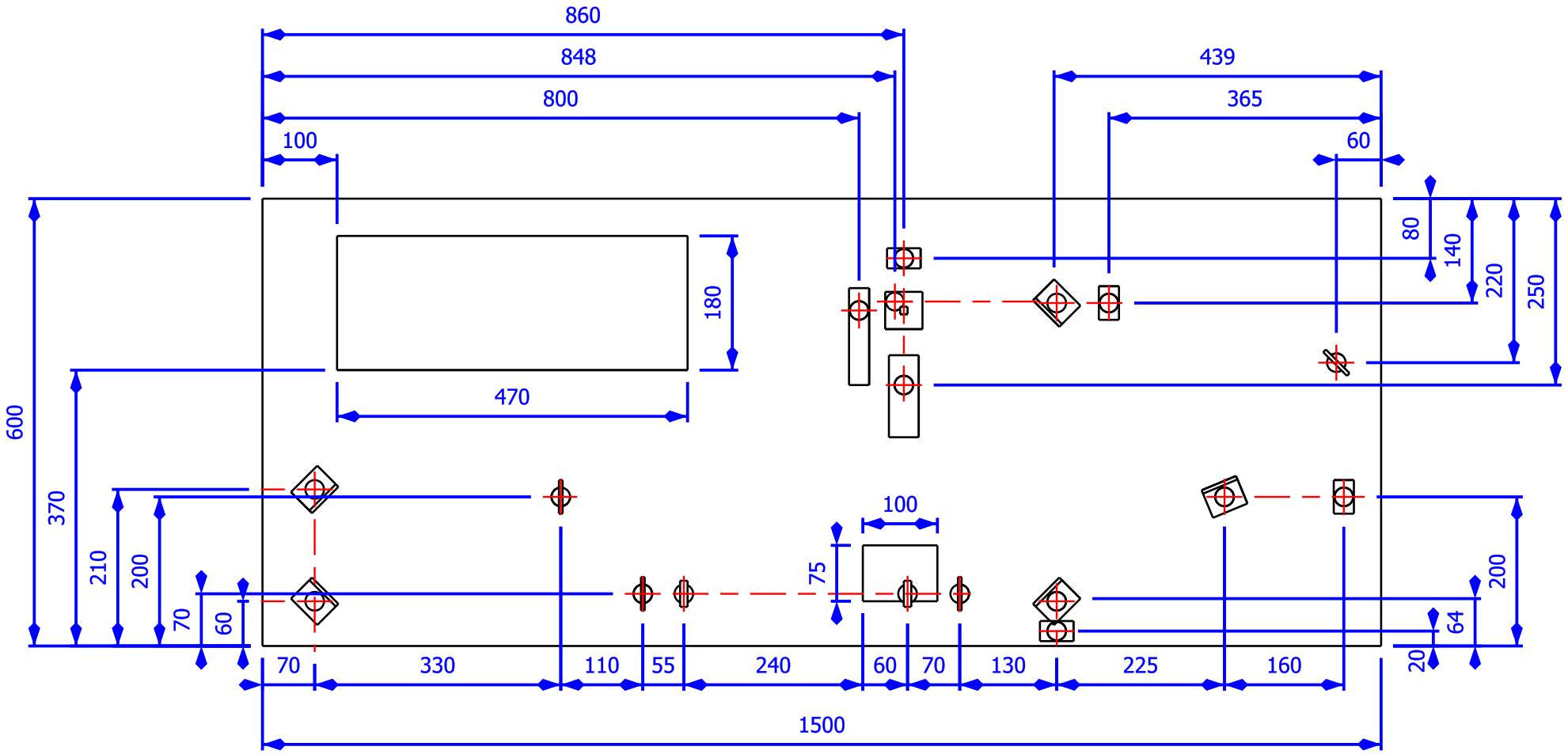

Created by:	Title:	Size:	Sheet:	Scale:
Christoph Marek	Laser Table	A4	X / Y	1:8

Supplementary information:	Part number: /
Position of optical elements	Drawing no.: /
	Date: 26/06/2018 — Revision: REV A

D. Measurement evaluation

This appendix is designed to give an overview of the evaluation used for the presented ^{36}Cl measurement results. The recorded raw data can be accessed via the VERA homepage and is located in the respective beamtime folder. Knowledge about the structure of the measurement routine is beneficial, hence it is highly recommended to read the Section 6.2 first.

The determination of an AMS sample is usually done with the help of a standard material, used for normalization, and a blank material.
If an automatic evaluation is configured, an automatic script determines the ^{36}Cl detector events N_{36Cl}, the measurement time t_{meas}, the reference high energy current I_{37Cl} and the high energy charge state Q. All of these values are stored for each individual iteration of a sequence run and can accessed via the homepage. Further calculations were usually done using a combination of *Microsoft® Excel* and *Python®*.

At first the detector count rate

$$R_{36Cl} = \frac{N_{36Cl}}{t_{meas}} \tag{D.1}$$

was calculated for each sequence run. The count rates of blank targets were afterwards averaged over all measurements and subtracted from sample and standard count rates of each sequence run.

$$R_{36Cl,Sample/Standard,corr} = R_{36Cl,Sample/Standard} - \bar{R}_{36Cl,Blank} \tag{D.2}$$

These corrected values and the high energy current of the reference were used to calculate the measured ^{36}Cl/^{37}Cl ratios

$$(^{36}\mathrm{Cl}/^{37}\mathrm{Cl})_{Sample/Standard} = \frac{R_{36Cl,Sample/Standard,corr} \cdot Q \cdot e}{I_{37Cl}} \tag{D.3}$$

of each sequence run. This way a ratio for each cathode and each turn is gained. The simultaneous measurement of the standard ratio allows the normalization of the sample ratios by applying the normalization factor

$$K = \frac{(^{36}Cl/^{37}Cl)_{Standard,nominal}}{(^{36}Cl/^{37}Cl)_{Standard,measured}} \tag{D.4}$$

In order to correct drifts during the measurement, the normalization factor K of all standard runs was calculated and averaged over each turn i. Afterwards the sample ratios where normalized by applying this factor K_i to the corresponding sample ratio of the turn.

$$(^{36}\mathrm{Cl}/^{37}\mathrm{Cl})_{Sample,norm,i} = (^{36}\mathrm{Cl}/^{37}\mathrm{Cl})_{Sample,i} \cdot K_i \tag{D.5}$$

The final value of the cathode material was determined by taking an weighted mean of the turn ratios.

$$\overline{(^{36}\mathrm{Cl}/^{37}\mathrm{Cl})}_{Sample,final} = \frac{\sum_i (^{36}\mathrm{Cl}/^{37}\mathrm{Cl})_{Sample,norm,i} \cdot w_i}{\sum_i w_i} \tag{D.6}$$

As weights w_i the product of measurement time and high energy current were used. Final ^{36}Cl/Cl ratios were calculated by using the mole fraction abundances of the stable chlorine isotopes.

The uncertainty of the final value is either the Gaussian propagation of the counting statistic or the statistic uncertainty of the mean value, depending on which of them is higher. Unless otherwise specified the 1σ value is given.

E. Machine setup for ^{36}Cl measurements

In Table E.2 typical parameter values of the ILIAMS system are given. The main parameters of the remaining AMS system are given in Table E.1.

		high energy charge state	
description	**parameter**	**7+**	**2+**
Electrostatic spherical analyzer	ESA 01-1|VC	5.0675 kV	
	ESA 01-2|VC	4.9861 kV	
Analyzing magnet	HPB 01-1|MfieldR	3726.5 Gauss	
Terminal voltage	TPS TK-1|GvmVC	3.0576 MV	1.7490 MV
Electrostatic spherical analyzer	ESA 04-1|VC	79.594 kV	60.163 kV
Analyzing magnet	HPB 03-1|MfieldR	4835.8 Gauss	7853.3 Gauss
Switching magnet	HPB 04-1|MfieldR	8922.7 Gauss	14985.3 Gauss

Table E.1.: Typical values of the common AMS system during ^{36}Cl measurements.

category	description	parameter	value
Ion Source Parameter	Cathode voltage	CAT S2-1| VC	-3 kV
	Extraction voltage	EXT S2-1| VC	6.59 to 7.14 kV
	Focal lens	FOC S2-1| VC	0.054 to 0.150 kV
	Ionizer	ION S2-1| CC	25 A
	Cs-oven	OVN S2-1| VC	27.2 to 28.0 V
	Line heater	LNH S2-1| CC	4 to 14 A
	Pre-acceleration	HVS S2-1| VC	-19.7 to 20.4 kV
RFQ cooler	Quadrupole frequency	RFQ I1-1| FreqC	2375 kHz
	Quadrupole amplitude	RFQ I1-1| AmplVC	0.0452 V
	Cooler potential	RFQ I1-1| HVVC	29.935 kV
	Cooler injection	RFQ I1-1| InjHVC	5.80 to 7.22 kV
		RFQ I1-1| InjLVC	0.76 to 0.93 kV
	Guide electrode	RFQ I1-1| GElecVC	20 to 40 V
	Cooler extraction	RFQ I1-1| ExtLVC	1.0 to 1.2 kV
		RFQ I1-1| ExtHVC	2.5 to 2.8 kV
Ion optic elements	2D-steerer (Ion source)	ESX S2-1| XVC	-540 to -980 V
		ESY S2-1| YVC	260 to 730 V
	2D-steerer (Cooler injection)	ESX I1-1| XVC	-570 to -1020 V
		ESY I1-1| YVC	-160 to 3 V
	2D-steerer (Cooler extraction)	ESX I1-2| XVC	-140 to 120 V
		ESY I1-2| YVC	-1225 V
	x&y-steerer	ESX I2-1| XVC	-0.12 to -0.09 kV
		ESY I2-1| YVC	-0.24 to -0.04 kV
	Electrostatic lens	EL I2-1| VC	-9.4 to -7.5 kV
		EL I2-2| VC	-12.7 to -10.6 kV
Ion filters	Bending magnet	BM I1-1| CC	59 A
	Electrostatic spherical analyzer	ESA I2-1| VC	4.997 kV

Table E.2.: Typical ILIAMS parameter during a ^{36}Cl measurement.

Bibliography

Andersson, P. (2009). *Laser photodetachment of negative ions*. PhD thesis, University of Gothenburg.

Andersson, P., Forstner, O., Hanstorp, D., Lindahl, A. O., and Wendt, K. (2009). *Isobar Selective Laser Photodetachment In Trace Element Analysis*. AIP Conference Proceedings, 1104(1):53–60, DOI:https://doi.org/10.1063/1.3115610.

Argento, D. C., Stone, J. O., Fifield, L. K., and Tims, S. G. (2010). *Chlorine-36 in seawater*. Nuclear Instruments and Methods in Physics Research Section B: Beam Interactions with Materials and Atoms, 268(7-8):1226–1228, DOI:https://doi.org/10.1016/j.nimb.2009.10.139.

Arnold, J. R. and Libby, W. F. (1949). *Age determinations by radiocarbon content: checks with samples of known age*. Science, 110(2869):678–680.

Beasley, T., Cecil, L., Sharma, P., Kubik, P., Fehn, U., Mann, L., and Gove, H. (1993). *Chlorine-36 in the Snake River Plain Aquifer at the Idaho National Engineering Laboratory: Origin and Implications*. Groundwater, 31(2):302–310, DOI:https://doi.org/10.1111/j.1745-6584.1993.tb01822.x.

Beasley, T., EImore, D., Kubik, P., and Sharma, P. (1992). *Chlorine-36 Releases from the Savanniah River Site Nuclear Fuel Reprocessing Facilities*. Groundwater, 30(4):539–548, DOI:https://doi.org/10.1111/j.1745-6584.1992.tb01530.x.

Bentley, H. W., Phillips, F. M., Davis, S. N., Habermehl, M. A., Airey, P. L., Claf, G. E., Elmore, D., Grove, H. E., and Torgersen, T. (1986). *Chlorine 36 dating of very old groundwater 1. The Great Artesian Basin, Australia*. Water Resources Research, 22(13):2991–2001.

Berkovits, D., Boaretto, E., Hollos, G., Kutschera, W., Naaman, R., Paul, M., and Vager, Z. (1989). *Selective suppression of negative ions by lasers*. Nuclear Instruments and Methods in Physics Research Section A: Accelerators, Spectrometers, Detectors and Associated Equipment, 281(3):663–666.

Buchriegler, J. (2013). *Construction of a Multi-Anode Ionization Chamber for AMS at VERA*. Master's thesis, University of Vienna.

Charalambus, S. (1971). *Nuclear transmutation by negative stopped muons and the activity induced by the cosmic-ray muons*. Nuclear Physics A, 166(2):145–161, DOI:https://doi.org/10.1016/0375-9474(71)90419-2.

Christophorou, L., Compton, R., and Dickson, H. (1968). *Dissociative electron attachment to hydrogen halides and their deuterated analogs*. The Journal of Chemical Physics, 48(5):1949–1955, DOI:https://doi.org/10.1063/1.1668996.

CVI™ (2018a). *PBSO:High Energy Laser Line Polarizing Cube Polarizers*. CVI Laser, LLC., Retrieved from: https://www.cvilaseroptics.com/pbso-high-energy-laser-line-polarizing-cube-polarizers/product/pbso_high_engergy_laser_line_polarizing_cube_polarizers in 2018.

CVI™ (2018b). *QWPM: Multiple Order Waveplates*. CVI Laser, LLC., Retrieved from: https://www.cvilaseroptics.com/qwpm-multiple-order-waveplates/product/qwpm_multiple_order_waveplates in 2018.

Davis, R. and Schaeffer, O. A. (1955). *Chlorine-36 in nature*. Annals of the New York Academy of Sciences, 62(1):107–121, DOI:https://doi.org/10.1111/j.1749-6632.1955.tb35368.x.

Davis, S. N., Cecil, D., Zreda, M., and Sharma, P. (1998). *Chlorine-36 and the initial value problem*. Hydrogeology Journal, 6(1):104–114, DOI:https://doi.org/10.1007/s100400050137.

De Laeter, J. R., Böhlke, J. K., De Bièvre, P., Hidaka, H., Peiser, H., Rosman, K., and Taylor, P. (2003). *Atomic weights of the elements. Review 2000 (IUPAC Technical Report)*. Pure and applied chemistry, 75(6):683–800, DOI:https://doi.org/10.1351/pac200375060683.

Drake, G. W., editor (2006). *Springer handbook of atomic, molecular, and optical physics*. Springer-Verlag New York.

Eliades, J., Zhao, X.-L., Litherland, A., and Kieser, W. (2015). *Negative ion–gas reaction studies using ion guides and accelerator mass spectrometry II: S-, SO- and Cl- with NO2 and N2O*. Nuclear Instruments and Methods in Physics Research Section B: Beam Interactions with Materials and Atoms, 361:300–306, DOI:https://doi.org/10.1016/j.nimb.2015.07.002.

EuroChlor (2009). *Chlorine Industry Review 2008–2009. Tackling issues in a transparent manner*. Retrieved from: http://www.eurochlor.org/media/10674/chlorine_industry_review_2008-2009.pdf.

Fabryka-Martin, J. T. (1988). *Production of radionuclides in the earth and their hydrogeologic significance, with emphasis on chlorine-36 and iodine-129*. PhD thesis, The University of Arizona.

Farley, J. W. (1989). *Photodetachment cross sections of negative ions: The range of validity of the Wigner threshold law*. Physical Review A, 40(11):6286, DOI:https://doi.org/10.1103/PhysRevA.40.6286.

Fifield, L., Ophel, T., Bird, J., Calf, G., Allison, G., and Chivas, A. (1987). *The chlorine-36 measurement program at the Australian National University*. Nuclear Instruments and Methods in Physics Research B, 29:114–119, DOI:https://doi.org/10.1016/0168-583X(87)90217-5.

Forstner, O., Andersson, P., Hanstorp, D., Lahner, J., Martschini, M., Pitters, J., Priller, A., Steier, P., and Golser, R. (2015). *The ILIAS project for selective isobar suppression by laser photodetachment*. Nuclear Instruments and Methods in Physics Research Section B: Beam Interactions with Materials and Atoms, 361:217–221, DOI:https://doi.org/10.1016/j.nimb.2015.04.021.

Forstner, O., Michlmayr, L., Auer, M., Golser, R., Kutschera, W., Priller, A., Steier, P., and Wallner, A. (2008). *Applications of a compact ionization chamber in AMS at energies below 1 MeV/amu.* Nuclear Instruments and Methods in Physics Research Section B: Beam Interactions with Materials and Atoms, 266(10):2213–2216, DOI:https://doi.org/10.1016/j.nimb.2008.02.060.

FreeCAD (2018). *FreeCAD: An open-source parametric 3D CAD modeler.* https://www.freecadweb.org/.

Génévriez, M. and Urbain, X. (2015). *Animated-beam measurement of the photodetachment cross section of H-.* Physical Review A, 91(3):033403, DOI:https://doi.org/10.1103/PhysRevA.91.033403.

Gosse, J. C. and Phillips, F. M. (2001). *Terrestrial in situ cosmogenic nuclides: theory and application.* Quaternary Science Reviews, 20(14):1475–1560, DOI:https://doi.org/10.1016/S0277-3791(00)00171-2.

Graedel, T. E. and Keene, W. (1996). *The budget and cycle of Earth's natural chlorine.* Pure and applied chemistry, 68(9):1689–1697, DOI:https://doi.org/10.1351/pac199668091689.

Hammer, S., Friedrich, R., Kromer, B., Cherkinsky, A., Lehman, S. J., Meijer, H. A., Nakamura, T., Palonen, V., Reimer, R. W., Smith, A. M., et al. (2017). *Compatibility of Atmospheric 14 CO 2 Measurements: Comparing the Heidelberg Low-Level Counting Facility to International Accelerator Mass Spectrometry (AMS) Laboratories.* Radiocarbon, 59(3):875–883, DOI:https://doi.org/10.1017/RDC.2016.62.

Hellborg, R. and Skog, G. (2008). *Accelerator mass spectrometry.* Mass spectrometry reviews, 27(5):398–427, DOI:https://doi.org/10.1002/mas.20172.

Hotop, H. and Lineberger, W. C. (1975). *Binding energies in atomic negative ions.* Journal of Physical and Chemical Reference Data, 4(3):539–576, DOI:https://doi.org/10.1063/1.555524.

Huggle, D., Blinov, A., Stan-Sion, C., Korschinek, G., Scheffel, C., Massonet, S., Zerle, L., Beer, J., Parrat, Y., Gaeggeler, H., et al. (1996). *Production of cosmogenic 36Cl on atmospheric argon*. Planetary and space science, 44(2):147–151, DOI:https://doi.org/10.1016/0032-0633(95)00085-2.

Kalb, A. (2017). *First Photodetachment Measurements of Slow Negative Molecules for AMS*. Master's thesis, University of Vienna.

Kieser, W., Zhao, X.-L., Clark, I., Cornett, R., Litherland, A., Klein, M., Mous, D., and Alary, J.-F. (2015). *The André E. Lalonde AMS Laboratory–the new accelerator mass spectrometry facility at the University of Ottawa*. Nuclear Instruments and Methods in Physics Research Section B: Beam Interactions with Materials and Atoms, 361:110–114, DOI:https://doi.org/10.1016/j.nimb.2015.03.014.

Kleijn, R. and Van der Voet, E. (1998). *Chlorine in Western Europe, a MacTempo case study*. CML, Leiden, The Netherlands.

Kutschera, W., Collon, P., Friedmann, H., Golser, R., Hille, P., Priller, A., Rom, W., Steier, P., Tagesen, S., Wallner, A., et al. (1997). *VERA: A new AMS facility in Vienna*. Nuclear Instruments and Methods in Physics Research Section B: Beam Interactions with Materials and Atoms, 123(1-4):47–50, DOI:https://doi.org/10.1016/S0168-583X(96)00782-3.

Lal, D. and Peters, B. (1967). *Cosmic ray produced radioactivity on the Earth*. In Sitte, K., editor, *Kosmische Strahlung II/Cosmic Rays II*, volume 9/46/2, pages 551–612. Springer, Berlin, Heidelberg. DOI:https://doi.org/10.1007/978-3-642-46079-1_7.

Laseroptik (2018). *VIS 380-779 nm, Coating HR 532nm/45°*. Laseroptik GmbH., Retrieved from: https://www.laseroptik.de/en/coatings/ranges/vis-380-779-nm in 2018.

Litherland, A. E., Tomski, I., Zhao, X.-L., Cousins, L. M., Doupé, J., Javahery, G., and Kieser, W. (2007). *Isobar separation at very low energy for AMS*. Nuclear Instruments and Methods in Physics Research Section B: Beam Interactions with Materials and Atoms, 259(1):230–235, DOI:https://doi.org/10.1016/j.nimb.2007.01.254.

Liu, Y. and Ning, C. (2015). *Calculation of photodetachment cross sections and photoelectron angular distributions of negative ions using density functional theory*. The Journal of chemical physics, 143(14):144310, DOI:https://doi.org/10.1063/1.4932978.

Marrero, S. M., Phillips, F. M., Caffee, M. W., and Gosse, J. C. (2016). *CRONUS-Earth cosmogenic 36 Cl calibration*. Quaternary Geochronology, 31:199–219, DOI:https://doi.org/10.1016/j.quageo.2015.10.002.

Martschini, M. (2012). *Development of methods for isobar suppression in AMS and measurements of 36Cl with the VERA 3-MV-tandem accelerator*. PhD thesis, University of Vienna.

Martschini, M., Andersson, P., Forstner, O., Golser, R., Hanstorp, D., Lindahl, A. O., Kutschera, W., Pavetich, S., Priller, A., Rohlén, J., et al. (2013). *AMS of 36 Cl with the VERA 3MV tandem accelerator*. Nuclear Instruments and Methods in Physics Research Section B: Beam Interactions with Materials and Atoms, 294:115–120, DOI:https://doi.org/10.1016/j.nimb.2012.01.055.

Martschini, M., Pitters, J., Moreau, T., Andersson, P., Forstner, O., Hanstorp, D., Lachner, J., Liu, Y., Priller, A., Steier, P., et al. (2017). *Selective laser photodetachment of intense atomic and molecular negative ion beams with the ILIAS RFQ ion beam cooler*. International Journal of Mass Spectrometry, 415:9–17, DOI:https://doi.org/10.1016/j.ijms.2016.12.015.

Moreau, T. (2016). *Development and characterization of the Ion Laser InterAction Setup (ILIAS)*. Master's thesis, University of Vienna.

Müller, A. M., Christl, M., Lachner, J., Suter, M., and Synal, H.-A. (2010). *Competitive 10Be measurements below 1 MeV with the upgraded ETH–TANDY AMS facility.* Nuclear Instruments and Methods in Physics Research Section B: Beam Interactions with Materials and Atoms, 268(17-18):2801–2807, DOI:https://doi.org/10.1016/j.nimb.2010.05.104.

NNDC (2018). *National Nuclear Data Center, Nuclear structure and decay data on-line library, Nudat 2.7.* http://www.nndc.bnl.gov/nudat2/, acessed in 2018.

Nottoli, E., Arnold, M., Aumaître, G., Bourlès, D. L., Keddadouche, K., and Suter, M. (2013). *The physics behind the isobar separation of 36 Cl and 10 Be at the French AMS national facility ASTER.* Nuclear Instruments and Methods in Physics Research Section B: Beam Interactions with Materials and Atoms, 294:397–402, DOI:https://doi.org/10.1016/j.nimb.2012.01.052.

O'Malley, T. F. (1965). *Effect of long-range final-state forces on the negative-ion photodetachment cross section near threshold.* Physical Review, 137(6A):A1668, DOI:https://doi.org/10.1103/PhysRev.137.A1668.

Palumbo, L., Benedetti, L., Bourles, D., Cinque, A., and Finkel, R. (2004). *Slip history of the Magnola fault (Apennines, Central Italy) from 36Cl surface exposure dating: evidence for strong earthquakes over the Holocene.* Earth and Planetary Science Letters, 225(1-2):163–176, DOI:https://doi.org/10.1016/j.epsl.2004.06.012.

Phillips, F. M. (2000). *Chlorine-36.* In Cook, P. G. and Herczeg, A. L., editors, *Environmental Tracers in Subsurface Hydrology*, pages 299–348. Springer US, Boston, MA. DOI:https://doi.org/10.1007/978-1-4615-4557-6_10.

Phillips, F. M., Argento, D. C., Balco, G., Caffee, M. W., Clem, J., Dunai, T. J., Finkel, R., Goehring, B., Gosse, J. C., Hudson, A. M., et al. (2016). *The CRONUS-Earth project: a synthesis.* Quaternary Geochronology, 31:119–154, DOI:https://doi.org/10.1016/j.quageo.2015.09.006.

Pitters, J. (2015). *Laser Photodetachment in a Gas-Filled RF-Quadrupole.* Master's thesis, University of Vienna.

Priller, A., Golser, R., Hille, P., Kutschera, W., Rom, W., Steier, P., Wallner, A., and Wild, E. (1997). *First performance tests of VERA*. Nuclear Instruments and Methods in Physics Research Section B: Beam Interactions with Materials and Atoms, 123(1-4):193–198, DOI:https://doi.org/10.1016/S0168-583X(96)00780-X.

Priller, A., Melber, K., Forstner, O., Golser, R., Kutschera, W., Steier, P., and Wallner, A. (2010). *The new injection beamline at VERA*. Nuclear Instruments and Methods in Physics Research Section B: Beam Interactions with Materials and Atoms, 268(7):824 – 826, DOI:https://doi.org/10.1016/j.nimb.2009.10.040.

Purser, K. H. (1977). *Ultra-sensitive spectrometer for making mass and elemental analyses*. US Patent 4,037,100.

Raisbeck, G., Yiou, F., Bourles, D., Lestringuez, J., and Deboffle, D. (1984). *Measurement of 10Be with a Tandetron accelerator operating at 2 MV*. Nuclear Instruments and Methods in Physics Research Section B: Beam Interactions with Materials and Atoms, 5(2):175–178, DOI:https://doi.org/10.1016/0168-583X(84)90505-6.

Rienstra-Kiracofe, J. C., Tschumper, G. S., Schaefer, H. F., Nandi, S., and Ellison, G. B. (2002). *Atomic and molecular electron affinities: photoelectron experiments and theoretical computations*. Chemical reviews, 102(1):231–282, DOI:https://doi.org/10.1021/cr990044u.

Rumble, J. R., editor (2018). *CRC Handbook of Chemistry and Physics, 99th Edition (Internet Version 2018)*. CRC Press/Taylor & Francis, Boca Raton, FL, http://hbcponline.com/.

Schlagenhauf, A., Gaudemer, Y., Benedetti, L., Manighetti, I., Palumbo, L., Schimmelpfennig, I., Finkel, R., and Pou, K. (2010). *Using in situ Chlorine-36 cosmonuclide to recover past earthquake histories on limestone normal fault scarps: a reappraisal of methodology and interpretations*. Geophysical Journal International, 182(1):36–72, DOI:https://doi.org/10.1111/j.1365-246X.2010.04622.x.

Stan-Sion, C., Huggle, D., Nolte, E., Blinov, A., and Dumitru, M. (1996). *AMS measurements of the production cross sections of 36Cl with protons up to 1 GeV*. Nuclear Instruments and Methods in Physics Research Section B: Beam Interactions with Materials and Atoms, 117(1-2):26–30, DOI:https://doi.org/10.1016/0168-583X(96)00240-6.

Steier, P. (2000). *Exploring the limits of VERA*. PhD thesis, University of Vienna.

Steier, P., Golser, R., Kutschera, W., Priller, A., Vockenhuber, C., and Winkler, S. (2004). *VERA, an AMS facility for "all" isotopes*. Nuclear Instruments and Methods in Physics Research Section B: Beam Interactions with Materials and Atoms, 223:67–71, DOI:https://doi.org/10.1016/j.nimb.2004.04.017.

Suter, M., Döbeli, M., Grajcar, M., Müller, A., Stocker, M., Sun, G., Synal, H.-A., and Wacker, L. (2007). *Advances in particle identification in AMS at low energies*. Nuclear Instruments and Methods in Physics Research Section B: Beam Interactions with Materials and Atoms, 259(1):165–172, DOI:https://doi.org/10.1016/j.nimb.2007.01.244.

Synal, H.-A. (2013). *Developments in accelerator mass spectrometry*. International Journal of Mass Spectrometry, 349:192–202, DOI:https://doi.org/10.1016/j.ijms.2013.05.008.

Synal, H.-A., Beer, J., Bonani, G., Suter, M., and Wölfli, W. (1990). *Atmospheric transport of bomb-produced 36Cl*. Nuclear Instruments and Methods in Physics Research Section B: Beam Interactions with Materials and Atoms, 52(3-4):483–488, DOI:https://doi.org/10.1016/0168-583X(90)90462-4.

Thorlabs® (2018a). *Protected Silver Mirrors*. Thorlabs®, Inc., Retrieved from: https://www.thorlabs.com/newgrouppage9.cfm?objectgroup_id=903 in 2018.

Thorlabs® (2018b). *UV Fused Silica Plano-Convex Lenses, AR Coated: 350-700nm*. Thorlabs®, Inc., Retrieved from: https://www.thorlabs.com/newgrouppage9.cfm?objectgroup_id=6508 in 2018.

VACOM® (2018). *VACOM® Produktkatalog*. VACOM Vakuum Komponenten & Messtechnik GmbH, Retrived from: https://www.vacom.de/downloads/vacom-produktkatalog?download=3241:vacom-produktkatalog-komplett in 2018.

Venuti, M. and Decleva, P. (1997). *Convergent multichannel continuum states by a general configuration interaction expansion in a B-spline basis: application to photodetachment*. Journal of Physics B: Atomic, Molecular and Optical Physics, 30(21):4839, DOI:https://doi.org/10.1088/0953-4075/30/21/020.

Wasserburger, P. (2018). *Simulation und Optimierung des Laser-Ionen-Aufbaus an VERA*. Master's thesis, University of Vienna.

Wigner, E. P. (1948). *On the behavior of cross sections near thresholds*. Physical Review, 73(9):1002, DOI:https://doi.org/10.1103/PhysRev.73.1002.

Wittkower, A. and Ryding, G. (1971). *Equilibrium charge-state distributions of heavy ions (1-14 MeV)*. Physical Review A, 4(1):226, DOI:https://doi.org/10.1103/PhysRevA.4.226.

Wiza, J. L. et al. (1979). *Microchannel plate detectors*. Nucl. Instrum. Methods, 162(1-3):587–601, DOI:https://doi.org/10.1016/0029-554X(79)90734-1.

Zerle, L., Faestermann, T., Knie, K., Korschinek, G., Nolte, E., Beer, J., and Schotterer, U. (1997). *The 41Ca bomb pulse and atmospheric transport of radionuclides*. Journal of Geophysical Research: Atmospheres, 102(D16):19517–19527, DOI:https://doi.org/10.1029/97JD00701.

Ziegler, J. and Biersack, J. (2008). *SRIM-2008: The stopping power and Range of Ions in Matter program package*. http://www.srim.org/.

Zoppi, U., Kubik, P., Suter, M., Synal, H.-A., Von Gunten, H., and Zimmermann, D. (1994). *High Intensity isobar separation at the Zürich AMS facility*. Nuclear Instruments and Methods in Physics Research Section B: Beam Interactions with Materials and Atoms, 92(1-4):142–145, DOI:https://doi.org/10.1016/0168-583X(94)95994-3.